Continuum mechanics of developing epithelia: Shaping a fly wing

DISSERTATION

zur Erlangung des akademischen Grades

Doctor rerum naturalium
(Dr. rer. nat.)

vorgelegt

der Fakultät Mathematik und Naturwissenschaften
der Technischen Universität Dresden

von

Marko Popović

geboren am 19. September 1987 in Zagreb

TECHNISCHE UNIVERSITÄT DRESDEN
MAX-PLANCK-INSTITUT FÜR PHYSIK KOMPLEXER SYSTEME

Dresden, 2017

Acknowledgments

Abstract

Developing tissues are out-of-equilibrium systems that grow and reshape to form organs in adult animals. They are typically composed of a large number of cells. The constitutive cells of a tissue perform different roles in tissue development and contribute to the overall tissue shape changes.

In this thesis, we construct a hydrodynamic theory of developing epithelial tissues. We use it to investigate the developing wing of the fruit fly *Drosophila melanogaster*. This theory relates the coarse-grained cell scale properties to the large-scale tissue flows. We explicitly account for the active cellular processes in the tissue that drive tissue flows. In our description of the tissue, we also include the memory effects that are necessary to account for the experimental observations. These memory effects have a significant influence on the tissue rheology.

Using this hydrodynamic theory we analyze shear flow in a developing fruit fly wing tissue. We find that the active cellular processes contribute to overall tissue flows and that memory effects are present in the wing tissue. We investigate consequences of these findings on the rheology of tissue shear flow. We find that the memory effects give rise to an inertial response that leads to oscillations in the tissue but it does not stem from the wing mass. Finally, we describe how the tissue rheology is affected by different boundary conditions.

We then investigate the area changes during the pupal wing development and we construct a mechanosensitive model for the cell extrusion rate in the pupal wing. Analysis of cell extrusions in the context of this model also allows us to extract information about the cell division properties.

Boundary connections between the wing tissue and surrounding cuticle are crucial for the proper development of the pupal wing. A *dumpy* mutant wing is strongly misshaped during the pupal wing morphogenesis. We use a simple model for the wing

to show that the *dumpy* mutant wing can be described as a wild type wing with compromised boundary conditions.

Finally, we analyze cell properties and tissue flows in a developing wing disc epithelium. Motivated by the observation of radially oriented active T1 transitions in the wing disc epithelium, we use the hydrodynamic theory to investigate the influence of such T1 transitions on stresses in the tissue. We show that sufficiently strong radially oriented active T1 transitions can contribute to the control of the tissue size.

Results obtained in this thesis extend our understanding of the fly wing tissue rheology and the role of internal and external forces in the proper shaping of the wing epithelium. The hydrodynamic theory we use to describe the fly wing development provides a set of phenomenological parameters that characterize the tissue mechanics and can be experimentally measured. Therefore, we expect that future research will include and extend the hydrodynamic theory presented in this thesis.

Contents

Chapter 1

Introduction

Multicellular living beings are organized in functional subunits called organs. Organs are typically made of a large number of cells. A collection of similar cells in an organ forms a tissue.

In order to study physical principles that govern mechanics of developing tissues, we need to keep in mind two important properties. First, the relevant processes that take place in a developing tissue span a wide range of temporal and spatial scales: from the characteristic length scales of $\sim 1\mu m$ and time scales of seconds at the level of cells, to the length scales of $\sim 1mm$ or more and time scales of hours or days at the level of the whole tissue. Second, living tissues constantly transduce energy. Therefore, they are not equilibrium systems and often not even close to a thermodynamic equilibrium. These two properties make understanding of the living tissues an exciting and complex challenge.

1.1 Physical models of developing epithelial tissues

In this section, we first introduce epithelial tissues and their mechanical properties. We describe the sources of stresses generated in the epithelial tissues that are required for their movement, maintenance and reshaping. We then present the two main classes of models currently used to describe the mechanics of the developing epithelial tissues. The first class contains cellular models that describe mechanical properties of each constituent cell. The overall tissue behavior is determined by solving the mechanical model of all cells in the epithelium. Models in the second class are continuum models that do not explicitly describe mechanics of each individual cell in the epithelial tissue.

Instead, they describe tissues as a coarse-grained cellular material, capturing their behavior at long spatial and temporal scales. They can still account for the cellular properties by introducing hydrodynamic fields that represent cell properties. Finally, we introduce the decomposition of large scale deformation into contributions stemming from different cellular processes. We present three recently developed realizations of such decomposition.

1.1.1 Introduction to epithelial tissues

Epithelia are two-dimensional sheets of cells. In an adult animal, their role is to cover body surfaces and outline body cavities and organs [1]. Figure 1.1 shows different types of epithelial tissues. Simple epithelia (left column in Fig. 1.1) contain only a single cell layer while stratified epithelia (middle column in Fig. 1.1) consist of several layers. Epithelia are classified by the shape of the constituent cells. Squamous epithelia (top row in Fig. 1.1) contain short and wide cells, cuboidal epithelia (middle row in Fig. 1.1) contain cells with comparable height and width and columnar epithelia (bottom row in Fig. 1.1) contain long and narrow cells. Pseudostratified epithelia (bottom right in Fig. 1.1) are a particular type of columnar epithelia that contain a single layer of cells but due to irregular organization of cell nuclei, they look like stratified epithelia.

Epithelia are polarized and distinguish an apical and a basal side. Their integrity is maintained by adherens junctions that link cell membranes and cytoskeleton between neighboring cells. An important component of adherens junctions is the cadherin family of proteins. In a cell, they provide connections between cytoskeleton and cadherin proteins of neighboring cells [2]. Mutations in cadherin genes produce defects in developing epithelial tissues and such tissues fail to develop properly [3, 4]. In order to reorganize the cellular network in an epithelium, adherens junction complexes have to be deconstructed on the disappearing cell-cell interfaces and constructed again on the appearing ones.

1.1.2 Active force generation in epithelial tissues

In addition to adhesion forces from adherens junctions that are necessary to ensure tissue integrity, forces are actively generated by a cytoskeleton in each cell. The
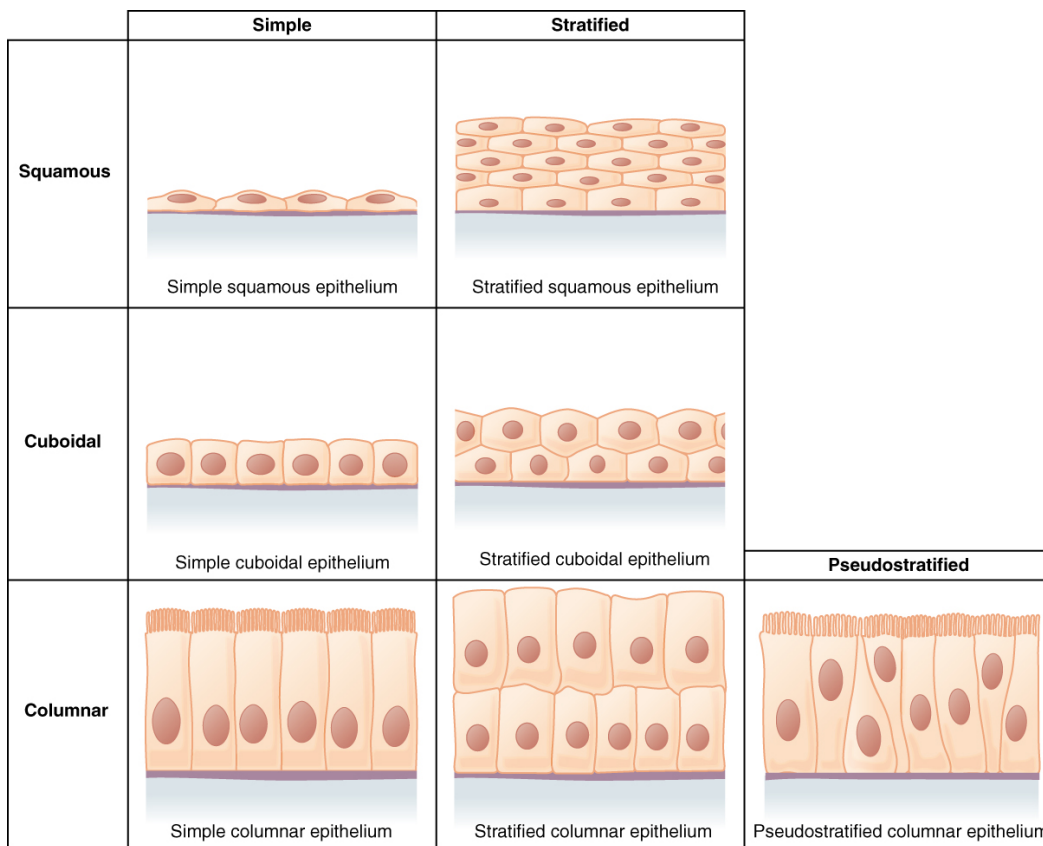
Figure 1.1: Types of epithelial tissues. Epithelial tissue can be divided by cell shape: squamous epithelia contain flat and thin cells, cuboidal epithelia contain cells that have similar height and width and columnar epithelia contain tall and narrow cells. Epithelia that are formed by a single cell layer are called simple and those formed by multiple cell layers are called stratified. Pseudostratified epithelia are formed by a single cell layer but appear as stratified due to the irregular distribution of cell nuclei. Source: OpenStax, Anatomy & Physiology. OpenStax CNX. Feb 26, 2016 http://cnx.org/contents/14fb4ad7-39a1-4eee-ab6e-3ef2482e3e22@8.24.

cytoskeleton is a network made of actin protein filaments interconnected by dynamic crosslinkers and myosin molecular motors that walk on the actin filaments. Myosin motors constantly consume energy in form of adenosine triphosphate (ATP) molecules and actively generate the tension in the cytoskeleton. Turnover of actin filaments and dynamics of crosslinkers allows relaxation of stress in the cytoskeleton. Therefore, on time scales longer than the actin turnover time the cytoskeleton behaves as a viscous fluid. On short times, the cytoskeletal network responds elastically to perturbations

and thus the cytoskeleton can be described as a Maxwell viscoelastic material. For a review see ref. [5].

Although cytoskeletal mechanics is well understood [6–9] the details of intracellular mechanics are not relevant for the physical description of the whole tissue. Instead, in models of tissue mechanics, the active forces generated inside cells are taken into account in a coarse-grained fashion. We now describe the two classes of models for epithelial tissues.

1.1.3 Cellular models of tissue mechanics

Figure 1.2: A) Vertex models describe mechanics of epithelial cells by coarse graining detailed mechanical cell properties. B) Realization of a 2D vertex model simulation, cells are colored according to their neighbor number. Source: adapted from ref. [10]
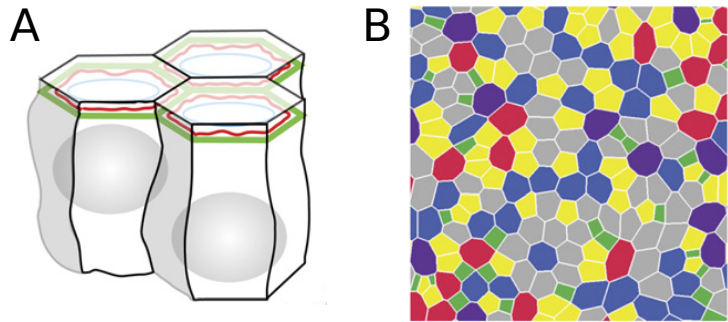
Cellular models of epithelia typically specify a model for the mechanics of individual cells and a set of rules that control interactions between the neighboring cells. Cellular models are used to describe both two-dimensions systems [10–24] and systems in which the curvature of epithelium requires either a three-dimensional description [25–28] or an effective three-dimensional description that assumes a particular symmetry in the tissue [29–32]. Detailed overviews of cellular models have been recently provided [33–35]. Two-dimensional cellular models have been used to investigate various biological processes such as cell shape and packing distributions [10, 14], cell sorting [12, 20, 36], patterning [23, 37] and tissue size control [22, 38]. Three-dimensional cellular models have been used to investigate appendage formation [25], gastrulation [29–31] and tissue folding and buckling [26–28, 32].

Cellular models provide a powerful tool to describe the mechanical properties of epithelial tissues. In most cases, cellular models have to be solved numerically, although sometimes analytical results can be found [39]. As these models keep track of each cell,

application of cellular models can be limited in tissues that contain a large number of cells. Moreover, one has to take care when constructing models of cell mechanics and cell interaction rules that conservation laws and symmetries are fulfilled, when necessary.

1.1.4 Continuum models of tissue mechanics

Developing epithelial tissues usually contain a large number of cells. For example, wing imaginal disc from which the fruit fly wing develops contains up to about 40000 cells [40]. When the cell number in a system is large and cell properties vary on scales larger than that of a single cell, behavior of individual cells becomes less important for understanding the physics of the whole tissue. Therefore, to develop a physical description of such epithelial tissues it is reasonable to use continuum models in which cell number density and other relevant cell properties are represented by hydrodynamic fields [17, 41–50] (see Fig. 1.3).

A cell number density n is a coarse-grained representation of a local cell number per unit area. The cell number density can change locally by cell divisions and cell extrusions, which are sources and sinks of cells, respectively. Otherwise, in absence of divisions and extrusions, the cell number density can only change by convection. Therefore, cell number balance equation (for example see [17]) can be written as

$$\partial_t n + \partial_k \left(n v_k \right) = n \left(k_d - k_e \right) \quad . \tag{1.1}$$

Here, k_d and k_e are cell division and extrusion rates defined as a number of divisions or extrusions per cell per unit time and v_i is the cell velocity field.

Forces in epithelial tissue are described by a two-dimensional stress tensor σ_{ij} that can be decomposed into an isotropic part equal to the negative two-dimensional pressure $P = -\sigma_{kk}/2$ and a traceless symmetric part called shear stress $\tilde{\sigma}_{ij} = \sigma_{ij} + P\delta_{ij}$. In principle, the stress tensor in tissues could also contain a finite antisymmetric stress component, but in this work we do not consider that possibility. In this thesis, we use Einstein summation convention over repeated indices unless explicitly stated otherwise.

A continuum theory is completed by providing appropriate constitutive equations.

In physical systems, in which a detailed microscopic model is available, constitutive equations can be derived by coarse-graining the microscopic model. However, our understanding of physical laws governing cellular and subcellular scales is currently limited. Therefore, we construct constitutive equations by including all terms allowed by symmetry to the lowest relevant order. If a system is close to equilibrium, one can use Onsager symmetry relations between coefficients in constitutive relations [51].
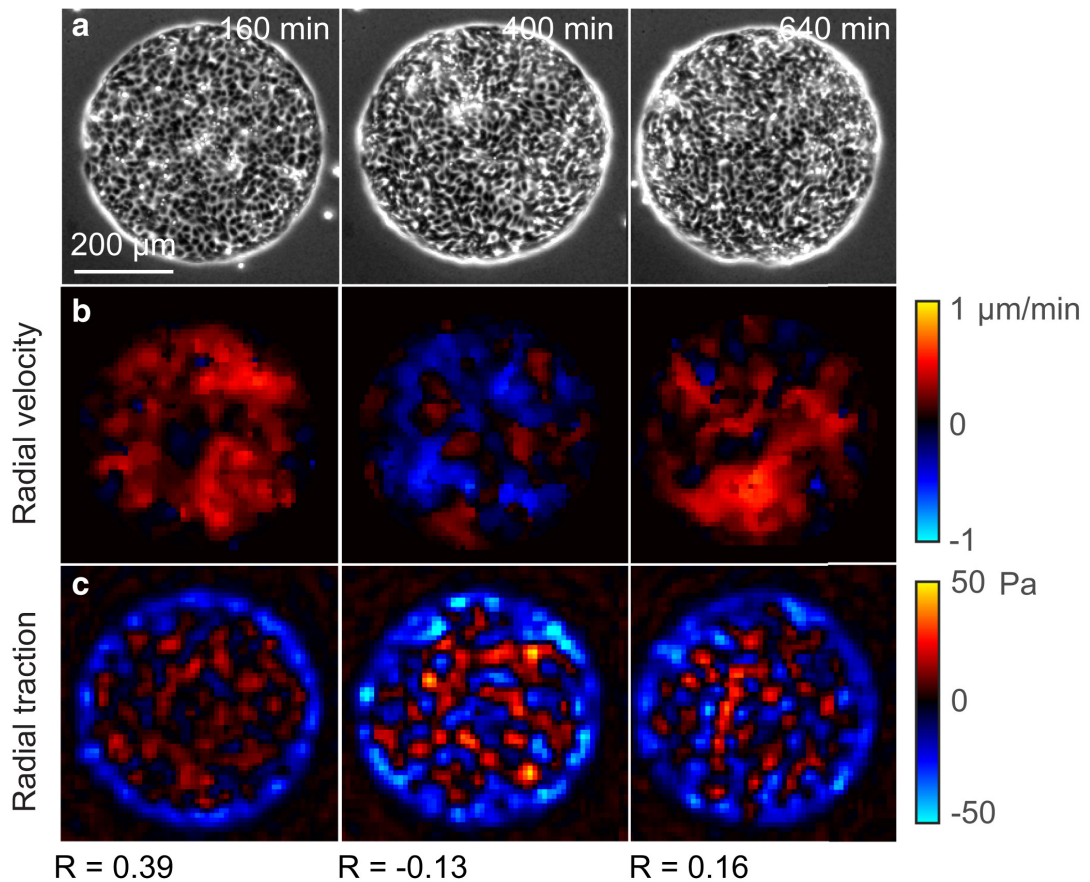
Figure 1.3: Top row: Cell monolayer confined to a circular domain. Middle row: Radial component of cell velocity. Bottom row: Radial component of force between cell layer and substrate determined by traction force microscopy. Source: ref. [50]

A number of constitutive equations for the stress in a tissue are used by the continuum tissue models. Although they can differ in a particular choice of the source

of stress, they obey symmetries of the problem. Here, we present an example of the constitutive equation for tissue stress used in a model that describes anisotropic tissue growth by cell divisions [17]. The authors propose the following constitutive equation for the tissue stress tensor

$$\sigma_{ij} = \eta \left(\partial_i v_j + \partial_j v_i - \frac{2}{d}\delta_{ij}\partial_k v_k \right) + \zeta \delta_{ij}\partial_l v_l - \mu k_d \left(p_i p_j - \frac{1}{d}\delta_{ij} \right) \quad . \tag{1.2}$$

Here, d is the dimension of space and η and ζ are shear and bulk viscosities, respectively. Vector p_i is a unit vector describing the preferred axis of cell divisions. This constitutive equation is relevant on long spatial and temporal scales where the lowest order gradient terms of the velocity field dominate. First and second terms on the right-hand side describe shear and bulk viscosity in the tissue, respectively. The last term accounts for the active stress generated by anisotropic cell divisions. The nematic symmetry of cell division is obeyed by the last term on the right hand side which is constructed as a traceless symmetric tensor, invariant to transformation $p_i \to -p_i$.

In addition to cell number density n and cell velocity v_i continuum models of tissues also include a coarse-grained description of various cell state properties such as concentrations of chemicals [44, 46, 47, 50], cell polarity [44, 46, 47, 50, 52] and nematic cell polarity [37, 52].

A parallel can be made between continuum theories of tissue and hydrodynamic theories of active polar gels [6, 53]. They involve a similar set of variables and the constitutive equations for such active gels derived using Onsager expansion around equilibrium are similar to the set of equations used for modeling tissues. In Chapter 3 we compare the constitutive equations governing shear flow in the fruit fly wing and Onsager theory of active viscoelastic nematic gel.

1.1.5 Cellular contributions to tissue deformation

Tissues are cellular materials and the overall tissue deformation stems from the deformation of cells and from the reorganization of the cellular network trough cell divisions, cell extrusions and cell neighbor exchanges. Several methods have been developed to quantify different cellular contributions to the overall tissue deformation.

In the tissue tectonics method [57], cell shape is defined by the best-fit ellipse and
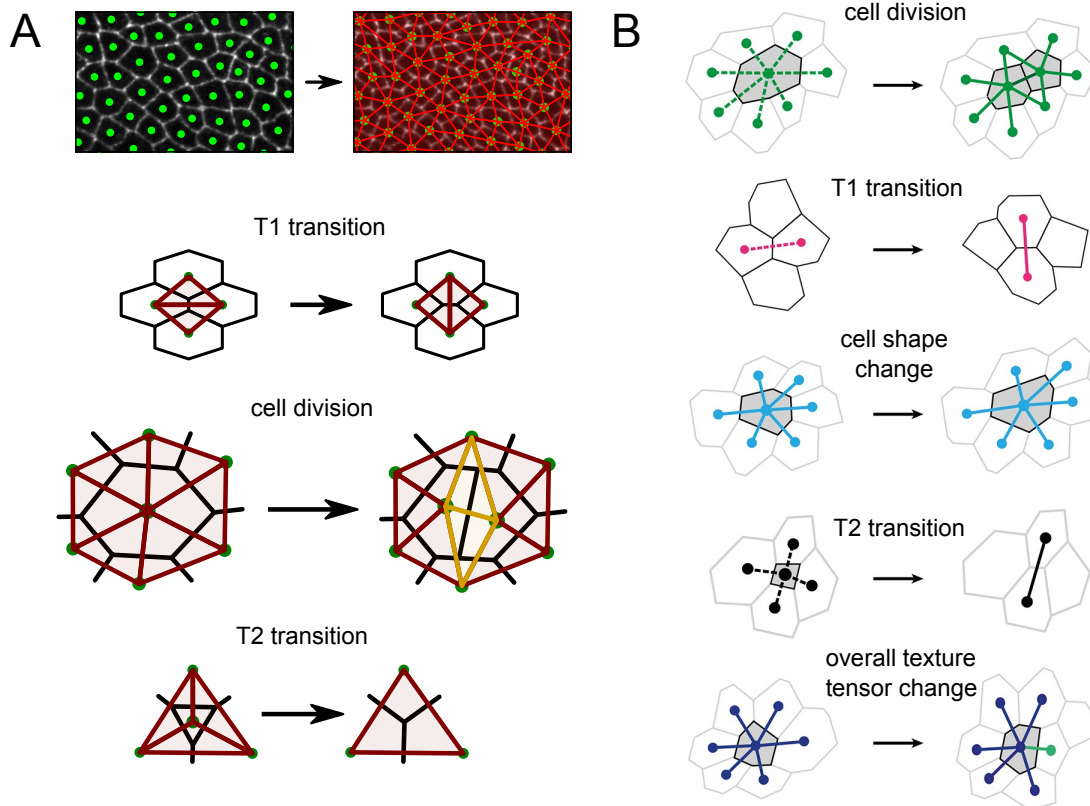
Figure 1.4: A) Top: triangulation of tissue used in triangle method [54, 55] to decompose overall tissue deformation into cellular contributions. Middle and bottom: Changes of topology in the cellular network due to different cellular processes create and destory triangles. Differences in shapes of created and destroyed triangles are used to quantify tissue deformation due to individual topological changes. B) Change of tissue texture tensor by different cellular processes. From top to bottom: division, T1 transition, shape change, T2 transition (extrusion) [56]. The bottom schematic shows the overall change in the texture tensor. These changes can be used to define cellular contribution to the tissue strain. Sources: A) adapted from ref. [54] B) adapted from ref. [56]

the deformation due to topological changes in defined as a different between the tissue velocity gradient and cell shape change rate. Currently, this method does not account for the tissue deformation due to cell divisions and extrusions.

The triangle method [54, 55] is based on triangulation of the tissue by connecting centers of neighboring cells. The average cell shape in a given tissue region is defined

through the shape of the corresponding triangles. Tissue deformation due to individual topological changes in the cellular network is then quantified by considering changes of geometry and topology of the triangulation (see Fig. 1.4 A). In this work we use the triangle method to quantify tissue deformation and its cellular contributions from the experimental data.

Another recently developed method [56] defines contributions of different cellular properties to the overall tissue deformation by considering the changes of so-called tissue texture tensor (see Fig. 1.4 B). Tissue texture tensor in a given tissue region is defined as

$$\mathbf{M} = \langle \boldsymbol{l} \otimes \boldsymbol{l} \rangle \quad , \tag{1.3}$$

where $\boldsymbol{l}$ is a vector connecting centers of neighboring cells and $\otimes$ is a dyadic product [58].

1.2 Fruit fly wing development

Here, we introduce the fruit fly *Drosophila melanogaster* as a model organism and we describe the development of the fruit fly wing. Of particular interest in this work are the larval and pupal stages of the fruit fly development. During the larval stages the wing grows and prepares the further development in pupal stages. During the pupal morphogenesis wing tissue reshapes through large scale tissue flows and obtains a form resembling the adult wing shape.

The fruit fly *Drosophila* has been used a model organism for more than a century. It has played a role in important discoveries in biology, for example, almost a century ago T. H. Morgan proved that genes are carried by chromosomes, by discovering a strong correlation between fly sex and inheritance of eye color [59]. The whole genome of *Drosophila* was sequenced and contains around 13600 genes [40, 60]. Investigations of *Drosophila* are not only limited to understanding invertebrate development. For example, a number of disease genes in humans have a fly gene counterpart [61].

The life cycle of the fruit fly consists of four main stages: embryonic stage, larval stage, pupal stage and the adult Fig. 1.5. At room temperature it takes about 10 days

| egg/embryo | larva | pupa | adult |

1 day   6 days   9 days
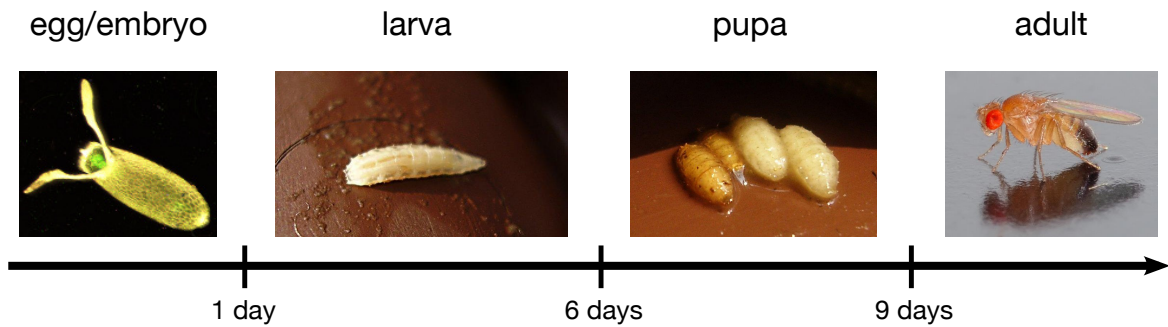
Figure 1.5: Developmental stages of the fruit fry *Drosophila melanogaster*. Embryonic stage lasts about 1 day. It is followed by the larval stage during which the animal grows during about 5 days and prepares for the pupal stage of development. In the pupal stage the imaginal tissues reorganize and form parts of the adult animal which emerges after about 3 days. Source: (left) JWSchmidt, commons.wikimedia.org (middle left and middle right) RickP, commons.wikimedia.org (right) André Karwath, commons.wikimedia.org

for a fertilized egg to develop into an adult fly [40]. Embryonic development lasts about 1 day. During the next 5 days of larval development the animal grows and accumulates resources required to undergo metamorphosis during the pupal development that takes additional 3 days.

After fertilization of the *Drosophila* egg the nucleus undergoes 13 rounds of divisions. The egg does not divide at that time and all the nuclei share common cytoplasm forming a syncytium. After the 9th round of divisions nuclei migrate to periphery and after the 13th round of divisions the syncytium cellularizes to form the blastoderm. Blastoderm cells are ancestors of all future tissues in the animal, including the wings [40].

1.2.1 Larval development

Most of the larval organs do not survive the pupal development stage but are used by the animal to grow and organize tissues called *imaginal discs*. The imaginal discs are small sheets of epithelia from which the adult structures of the animal will form [40] (see Fig. 1.6 A). The name 'imaginal disc' comes from the name of the adult structures known as 'imago' [62].

Fruit fly wings develop from the wing imaginal discs that at the beginning of larval
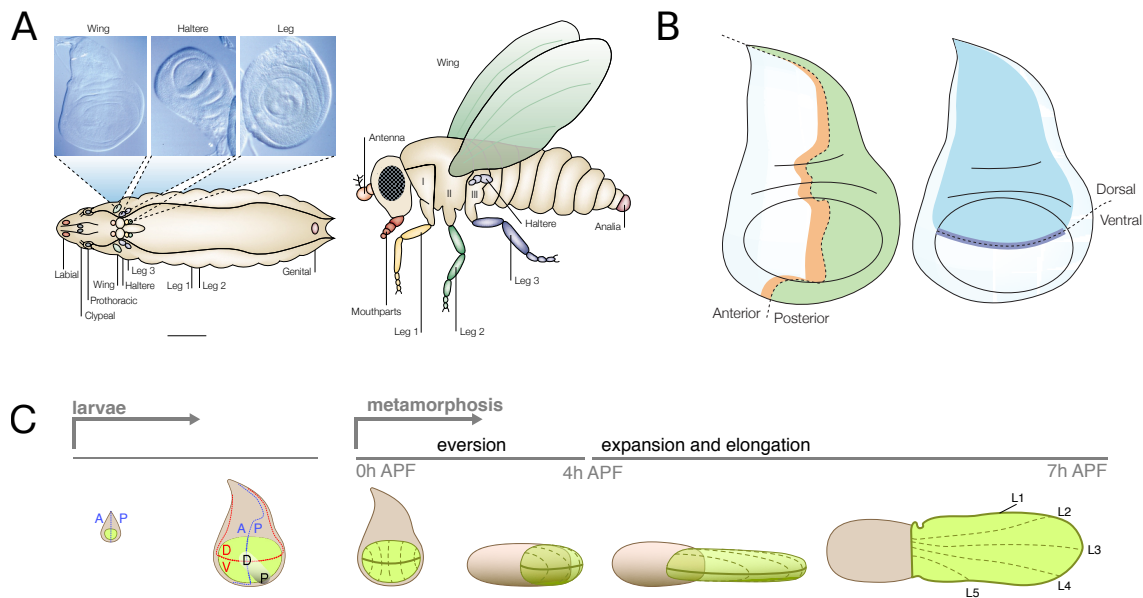
Figure 1.6: A) Organs of the adult animal form from epithelial tissue called imaginal discs. B) Wing imaginal disc in a late stage of larval development. Left: anterior (white) and posterior (green) wing disc compartments are separated by the anterio-posterior (AP) compartment boundary (orange). Right: dorsal (blue) and ventral (white) wing disc compartments are separated by the dorso-ventral (DV) compartment boundary (dark blue). C) During larval development wing imaginal disc increases its size and wing disc compartments are formed. At the end of larval development the wing disc everts and the wing disc pouch (green) reorganizes into a double layer that will form the wing blade in the adult animal. Source: A) adapted from ref. [63] B) adapted from ref. [64] C) adapted from ref. [65]

stage contain about 40 cells and throughout the larval stage the number of cells increases by a factor of 1000 [40]. At the same time, the main tissue axes of the wing are specified and compartment boundaries are formed that separate anterior, posterior, dorsal and ventral wing compartments (see Fig. 1.6 B). At the transition to the pupal stage of development the wing disc epithelium everts and the pouch region of the wing disc forms a double layered epithelium (see Fig. 1.6 C).

1.2.2 Pupal development

The double layered wing epithelium formed during eversion process reshapes during the pupal morphogenesis. This process takes place between around 15 and 36 hours

after pupa formation (hAPF) (see Fig. 1.7 A).

At around 30 hAPF the main features of the wing are clearly visible (see Fig. 1.7 B). Two main regions of the wing are the *blade* region (green) forming the most of the wing area and the *hinge* region (brown) that connects the wing to the body of the animal. Four longitudinal veins and two crossveins are visible in the wing blade (see Fig. 1.7 B).

After 40 hAPF the pupal wing flattens, expands and begins to fold as it does not fit into the space it is confined to. It remains folded until the animal hatches. Once the fly hatches the veins are filled with fluid that spreads the wing (see Fig. 1.7 A). During 2 hours after the hatching most of the living cells in the wing are removed and the adult wing is formed mostly by the cuticular material [65].
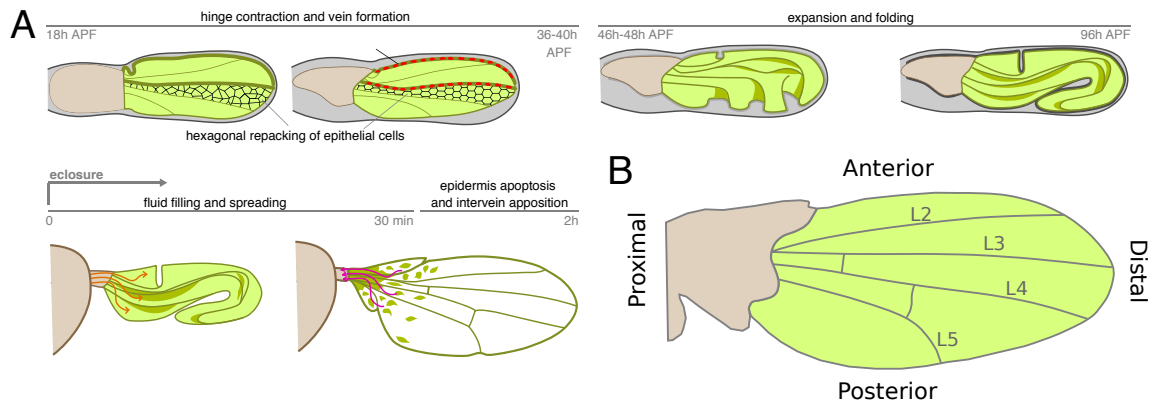
Figure 1.7: A) During pupal morphogenesis wing blade reshapes, veins are formed and hexagonal packing of cells emerges. Wing then expands, folds and remains folded until hatching. Soon after the adult animal emerges from the pupal case fluid fills veins and spreads the wing. B) Shape of the adult and late pupal wing. Two main regions of the wing are hinge (brown) and blade (green). Four longitudinal veins are indicated by their names. Source: A) adapted from ref. [65] B) adapted from ref. [54]

Chapter 2

Hydrodynamic theory of epithelial tissue flow

In this chapter, we present a generic hydrodynamic theory of large-scale tissue flows. We introduce a coarse-grained description of cell scale quantities as hydrodynamic fields. We decompose the overall tissue flow into contributions arising from different cellular processes. A concrete realization of these hydrodynamic fields and flow decomposition is given by the triangle method [55]. We then propose constitutive relations relating mechanical stresses to the tissue state properties as well as a constitutive equation for the tissue shear flow due to topological rearrangements. In these constitutive relations, we explicitly include memory effects to account for the complex mechanisms that govern mechanics of cells in a living tissue.

Hydrodynamic theory presented here has been published in ref. [66].

2.1 Continuum description of tissue flow

In a continuum description of tissue flow, we are not concerned with the movement of the individual cells. Therefore, we need to define the tissue velocity field based on the coarse-grained movement of the constituent cells. The cell number flux density J_i can be measured as the number of cells passing trough a unit line segment per unit time. Similarly, the local cell number density n is the number of cells per unit area in a given region of the tissue. We define tissue velocity as

$$v_i = \frac{J_i}{n} \quad .$$

(2.1)

A homogeneous tissue velocity field only translates the tissue but does not change the tissue shape. To describe the changes in the overall tissue shape we need to investigate spatial variations of the tissue velocity field v_i described by the tissue velocity gradient tensor $\partial_i v_j$. The velocity gradient tensor is represented by a matrix that can be uniquely decomposed into a trace, traceless symmetric and antisymmetric parts

$$\partial_i v_j = \frac{1}{2} v_{kk} \delta_{ij} + \tilde{v}_{ij} + \omega_{ij} \quad . \tag{2.2}$$

The trace of the velocity gradient tensor v_{kk} describes tissue area changes, the traceless symmetric part

$$\tilde{v}_{ij} = \frac{1}{2} \left(\partial_i v_j + \partial_j v_i - v_{kk} \delta_{ij} \right) \tag{2.3}$$

corresponds to the pure shear flow and the antisymmetric part

$$\omega_{ij} = \frac{1}{2} \left(\partial_i v_j - \partial_j v_i \right) \tag{2.4}$$

describes tissue rotation.

2.2 Cell state properties as hydrodynamic fields

We now extend the coarse-grained description of the tissue by defining the hydrodynamic fields corresponding to cellular state properties: cell size, cell shape and internal anisotropy of cell structure (Fig. 2.1 C).

Cell area

We define the average cell area in a given region of the tissue as

$$a = \frac{1}{n} \quad . \tag{2.5}$$
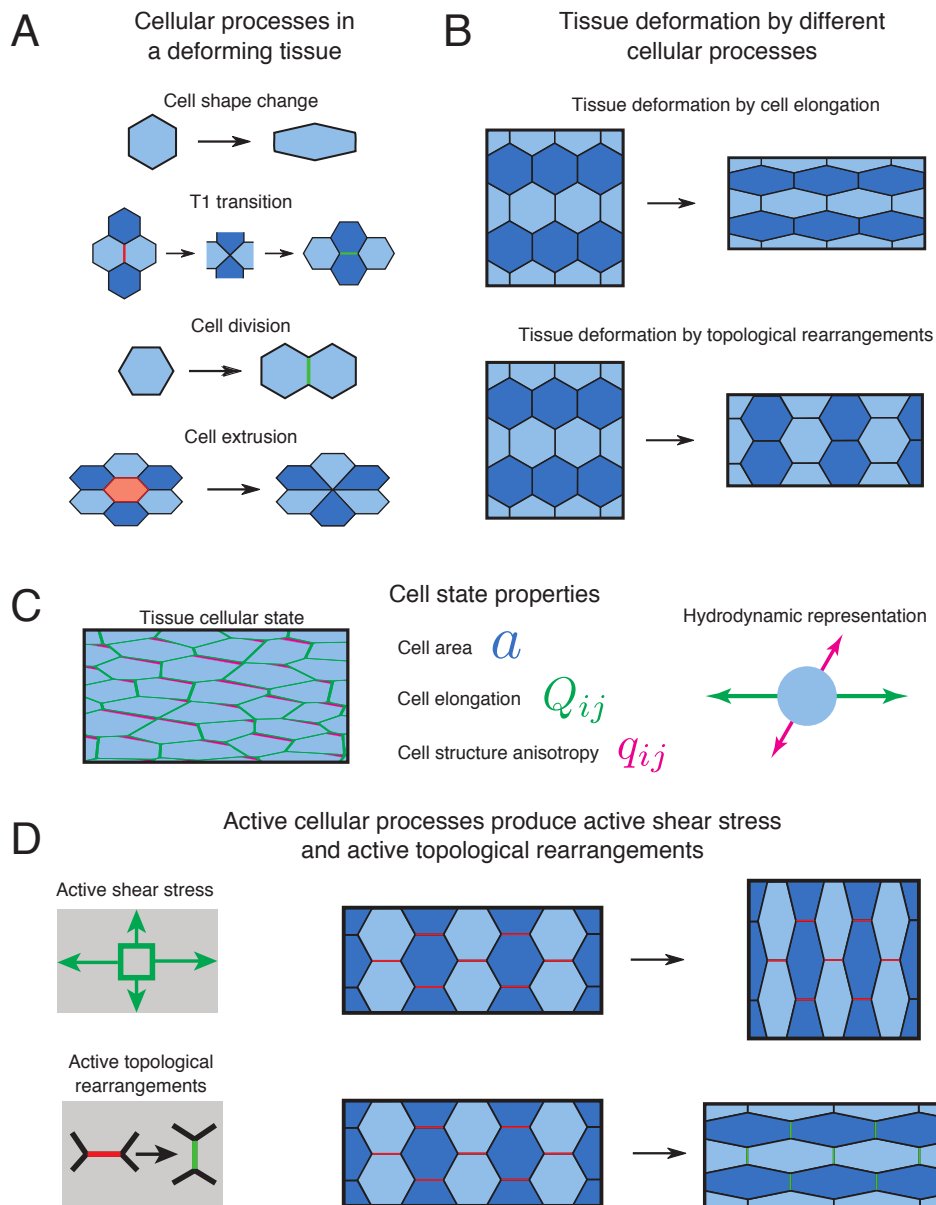
Figure 2.1: A) Cellular processes that contribute to the tissue deformation. B) The same overall tissue deformation can be obtained by different cellular processes. Schematics show how the same tissue deformation can be realized by either deforming cells (top) or by rearranging cells without deforming them (bottom). C) In a continuum theory, cell state properties are coarse grained and represented by hydrodynamic fields. D) Active cellular processes can produce active shear stress (top) and active topological rearrangements (bottom). These active processes produce different cell and tissue behavior. Source: adapted from ref. [66]

Cell elongation

The anisotropy of cell shape can be described to the lowest order by the cell elongation nematic tensor Q_{ij}. Two-dimensional nematic tensor is described by a magnitude Q and an orientation angle φ

$$Q_{ij} = Q \begin{pmatrix} \cos 2\varphi & \sin 2\varphi \\ \sin 2\varphi & -\cos 2\varphi \end{pmatrix} \tag{2.6}$$

The magnitude Q of the cell elongation tensor represents the amount of cell shape anisotropy and the nematic angle φ specifies the cell shape orientation.

Theory presented in this thesis does not depened on a precise definition of the cell elongation tensor as long as it satisfies the following condition. In a homogeneously deforming tissue, and in absence of any changes of the cellular network topology, the change of average cell elongation should be equal to the average tissue shear flow

$$\frac{\mathrm{D}Q_{ij}}{\mathrm{D}t} = \tilde{v}_{ij} \quad . \tag{2.7}$$

Here, $\mathrm{D}/\mathrm{D}t$ is a corotational convected derivative as defined in Appendix A.1.

To to analyse experimental data in this thesis we use the definition of cell elongation based on the triangulation of the cellular network as defined in [55].

Cell polarity

The internal anisotropic distribution of various proteins in a cell can be ordered on tissue scales. For example, during growth of the *Drosophila* wing epithelium, planar cell polarity systems are established. Complexes of proteins are distributed anisotropically in each cell and this anisotropy is ordered on scales that are large compared to a single cell [67]. Therefore, in our hydrodynamic description of the tissue we introduce a nematic tensor q_{ij} to represent the information contained in the anisotropic distributions of proteins or other objects inside the cell. For practical purposes, we use only one such nematic polarity tensor field. It is straightforward to introduce additional cell polarity nematics or vectors if needed for a particular application.

Planar cell polarity has been experimentally measured from the distribution of different polarity proteins on cell bonds [37, 67].

2.3 Cellular contributions to tissue flow

In this section, we decompose tissue flows into contributions arising from different cellular processes. This allows us to distinguish situations in which the overall tissue flow is the same but the behavior of cells is very different. The cellular processes we consider are cell shape and size changes, cell neighbor exchanges called T1 transitions, cell divisions and cell extrusions or T2 transitions (see Fig. 2.1 A). We now consider cellular contributions to the isotropic and shear parts of the tissue flow.

2.3.1 Isotropic flow decomposition

In a fixed region, the cell number can change either due to cells flowing in or out of the region or by cells inside the region dividing or extruding. Therefore, the cell number density balance equation contains divisions as a source and extrusions as a sink

$$\partial_t n + \partial_k \left(v_k n \right) = n \left(k_d - k_e \right) \quad .\tag{2.8}$$

Here, k_d and k_e are cell division and extrusion rates defined in a given time interval Δt as

$$k_d = \lim_{\Delta t \to 0} \frac{1}{N} \frac{\Delta N_{\text{division}}}{\Delta t} \tag{2.9}$$

$$k_e = \lim_{\Delta t \to 0} \frac{1}{N} \frac{\Delta N_{\text{extrusion}}}{\Delta t} \quad ,\tag{2.10}$$

where $\Delta N_{\text{division}}$ and $\Delta N_{\text{extrusion}}$ are the changes of cell number due to division and extrusion, during the interval Δt in the considered region, respectively. The number of cells in the region is denoted by N. We can now express the trace of the velocity gradient tensor, corresponding to the local tissue area change, as

$$v_{kk} = -\frac{1}{n} \frac{\mathrm{d}n}{\mathrm{d}t} + k_d - k_e \quad ,\tag{2.11}$$

where $\mathrm{d}/\mathrm{d}t$ is the convected derivative as defined in Appendix A.1. Using the definition of average cell area $a = 1/n$ we can rewrite this as

$$v_{kk} = \frac{1}{a}\frac{\mathrm{d}a}{\mathrm{d}t} + k_d - k_e \quad . \tag{2.12}$$

This is the decomposition of isotropic tissue flow into cellular contributions. If we consider a region co-moving with the tissue, the trace of the velocity gradient tensor corresponds to the relative tissue area change rate and we can write

$$\frac{1}{A}\frac{\partial A}{\partial t} = \frac{1}{a}\frac{\partial a}{\partial t} + k_d - k_e \quad , \tag{2.13}$$

where A is the area of the co-moving tissue region and a is the average cell area in the region.

2.3.2 Shear flow decomposition

The pure shear component of the tissue flow describes the anisotropic tissue shape change that preserves the tissue area. The pure shear can be produced by anisotropic cell shape changes, corresponding to the changes in the cell elongation, oriented cell division and extrusions and T1 transitions. For example, the same amount of tissue shear produced by the cell elongation change and by T1 transitions is shown in Fig. 2.1 B.

When analyzing experimental data, we use the triangle method [55] to decompose the tissue shear rate into its cellular contributions. In the triangle method, an additional term D_{ij} arises in the shear decomposition equation stemming from the collective correlated movements of elongated cells. The tissue shear flow decomposition can therefore be written as

$$\tilde{v}_{ij} = \frac{\mathrm{D}Q_{ij}}{\mathrm{D}t} + T_{ij} + C_{ij} + E_{ij} + D_{ij} \quad . \tag{2.14}$$

Here, T_{ij} is the tissue shear rate due to T1 transitions, C_{ij} is the shear rate due to cell divisions, E_{ij} is the shear rate due to cell extrusions. The shear rate due to the correlation effects is denoted by D_{ij}. A detailed discussion of these correlation effects

is out of the scope of this thesis.

It is useful to define a quantity which accounts for the sum of all tissue shear rate contributions not arising from cell shape changes

$$R_{ij} = T_{ij} + C_{ij} + E_{ij} + D_{ij} \quad . \tag{2.15}$$

We will call this tensor *shear rate due to topological rearrangements*. In terms of this tensor the tissue shear rate can be written as

$$\tilde{v}_{ij} = \frac{\mathrm{D}Q_{ij}}{\mathrm{D}t} + R_{ij} \quad . \tag{2.16}$$

Theoretical models developed in this thesis will use the shear rate due to topological rearrangements.

2.4 Forces in epithelia and force balance

Tissue growth and shape changes, as well as size and shape of constituent cells, are driven by external forces and by mechanical stresses generated inside the cells. External forces consist of body forces which act throughout the whole tissue and forces imposed by the physical constraints to the tissue shape that act at the tissue boundaries. Examples of body forces are gravitation and friction with a substrate. The former usually has a negligible effect on the tissue mechanics while the latter can be important. Forces imposed by the physical constraints are taken into account through boundary conditions.

Epithelia are effectively two-dimensional. To describe forces acting in them we will use the two-dimensional stress tensor σ_{ij} which can be obtained by integrating the usual three-dimensional stress along axis normal to the epithelium. We will refer to the two-dimensional stress simply as *stress*. Tissue stress can be decomposed into isotropic part $-P\delta_{ij}$ corresponding to the negative pressure and traceless symmetric part $\tilde{\sigma}_{ij}$ called shear stress

$$\sigma_{ij} = -P\delta_{ij} + \tilde{\sigma}_{ij} \quad . \tag{2.17}$$

In developing tissues, inertial forces are negligible. To quantitatively support this approximation, we now make a rough estimate of inertial forces in a developing fly wing tissue [54]. Reasonable estimates of the wing dimensions are: length $L \sim 800\mu m$, height $h \sim 200\mu m$, thickness $w \sim 100\mu m$. We assume that the density of the wing tissue is close to the density of water $\rho \sim 10^3 kg/m^3$ so that the mass of the wing is on the order of $m_{\mathrm{wing}} \sim 1.6 \cdot 10^{-8} kg$. Cells in the wing travel up to about $\Delta x \sim 200\mu m$ over about $\Delta t \sim 10h$ from which we can estimate an acceleration in the wing to be up to $a \sim 1.5 \cdot 10^{-11} ms^{-2}$. Therefore, we can estimate an upper limit on inertial forces in the developing pupal wing tissue to be on the order of $F_{\mathrm{inertial}} \sim 2.5 \cdot 10^{-21} N$. For comparison, we now estimate elastic forces in the tissue. Typical elastic constant of a cell is or the order of $K \sim 10 Pa$ and a typical cell size is $l = 10\mu m$. If we also assume that a typical cell strain is $\epsilon = 0.05$, we can estimate that the elastic forces in the tissue are on the order of $F_{\mathrm{elastic}} \sim 5 \cdot 10^{-11} N$. Therefore, the inertial forces are more than 9 orders of magnitude weaker than other relevant forces in the tissue

$$\frac{F_{\mathrm{inertial}}}{F_{\mathrm{elastic}}} \sim 5 \cdot 10^{-9} \quad , \tag{2.18}$$

and we can neglect them in the force balance equation

$$\partial_i \sigma_{ij} + f_j^{\mathrm{ext}} = 0 \quad . \tag{2.19}$$

Here, f_i^{ext} is force density of the external body forces.

2.5 Linear constitutive relations

We now complete the hydrodynamic description of the tissue mechanics and propose generic linear constitutive relations for tissue pressure, shear stress, and shear due to topological rearrangements. To capture possible memory effects in the tissue we include memory kernels in the constitutive equations.

2.5.1 Mechanical stress

Shear stress

The mechanical shear stress is a symmetric traceless tensor and to the linear order it depends only on other tensors with the same symmetry. Therefore, we propose a constitutive equation for shear stress that contains a linear elastic term proportional to the cell elongation Q_{ij} and a term arising from cell polarity q_{ij}

$$\tilde{\sigma}_{ij}(t) = 2K \int_{-\infty}^{t} \phi_K\left(t-t'\right) Q_{ij}(t')dt' + \zeta \int_{-\infty}^{t} \phi_\zeta\left(t-t'\right) q_{ij}(t')dt' \quad . \tag{2.20}$$

Here, parameters K and ζ have units of stress. Memory kernels ϕ_K and ϕ_ζ have units of rate. In general, they might not be isotropic in which case they would be represented by fourth order tensors. Here, we assume that all anisotropies are accounted for by cell elongation Q_{ij} and nematic cell polarity q_{ij} and thus we use scalar memory kernels. Both memory kernels are normalized so that $\int_0^\infty \phi_{K,\zeta}(t)dt = 1$.

Tissues actively transduce energy to maintain their structure and thus both of the terms on the right-hand side of Eq. (2.20) contain contributions stemming from the transduction of energy in the cell. The first term describes the elastic response to the change of cell shape. The second term depends on cell polarity and is reminiscent of active stress in active fluids [6]. We will refer to it as *active shear stress*. Fig. 2.1 D illustrates how active shear stress can affect cell and tissue shape. A more detailed discussion of the active shear stress is presented in Section 3.5.

Pressure

As in the case of the shear stress, we write the pressure in the tissue as a function of the other scalar quantities in the system. In particular, the elastic response to the cell area can be described by the following constitutive equation

$$P = -\overline{K} \int_{-\infty}^{t} \phi_{\overline{K}}\left(t-t'\right) u(t')dt' \quad , \tag{2.21}$$

where $\overline{K}$ is the isotropic elastic constant and $\phi_{\overline{K}}$ is the corresponding memory kernel. It is normalized so that $\int_0^\infty \phi_{\overline{K}}(t)dt = 1$. The natural cell strain u is defined as

$$u = \ln \frac{a}{a_0} \quad . \tag{2.22}$$

Here, we have introduced the *preferred cell area* a_0 which corresponds to the average cell area in a pressure free tissue. Unlike the quantities introduced in Section 2.2 we do not consider the preferred cell area to be an observable quantity since at present we are not able to measure it directly.

Dynamics of the preferred cell area

We now construct a model for the dynamics of the preferred cell area. A tissue under constant pressure can change its size by changing the cell size. This is achieved by adjusting the preferred cell area. Alternatively, in a tissue that grows in time by increasing the number of cells at the expense of a reservoir of cellular material, the preferred cell area does not change in time. Finally, in a tissue that produces new cells but does not have a source of the cellular material, the daughter cells will be smaller than their mother cell and their preferred cell area will be reduced. To capture these properties of the preferred cell area we propose the following dynamical equation

$$\frac{1}{a_0} \frac{da_0}{dt} = \beta(a_0) - (1 - \epsilon) k_d \quad . \tag{2.23}$$

The function $\beta(a_0)$ has units of rate and describes growth of the preferred cell area in time, independent of cell divisions. The second term is proportional to the cell division rate. The dimensionless parameter ϵ controls the influence of cell divisions on the preferred cell area. For $\epsilon = 1$ divisions do not affect the preferred cell area and the tissue can grow by increasing the cell number. This would correspond to the case when there is a reservoir of cellular material present, for the daughter cells to use and grow. In the case $\epsilon = 0$ the daughter cells have exactly one half of their mother's preferred cell area and thus, under the same pressure, we expect the tissue to maintain its size although the number of cells grows in time. This process cannot reduce the cell area below a certain physical limit a_{limit} and thus the product $(1 - \epsilon) k_d$ has to vanish as

cell area approaches this limit. If we assume that value ϵ is mostly controlled by the cellular material reservoir, the cell division rate has to obey $k_d \left(a \to a_{\text{limit}} \right) \to 0$.

2.5.2 Shear rate due to topological rearrangements

Finally, we propose a constitutive equation for shear rate due to topological rearrangements R_{ij} defined by Eq. (2.15). It is a traceless symmetric tensor and thus, as in the case of shear stress, the corresponding constitutive equation contains a term proportional to the cell elongation Q_{ij} and a term proportional to the cell polarity q_{ij}

$$
R_{ij} = \frac{1}{\tau} \int_{-\infty}^{t} \phi_\tau \left(t - t' \right) Q_{ij} \left(t' \right) dt' + \lambda \int_{-\infty}^{t} \phi_\lambda \left(t - t' \right) q_{ij}(t') dt' \quad , \tag{2.24}
$$

where τ and λ have units of time and rate, respectively. Memory kernels ϕ_τ and ϕ_λ have units of rate and are normalized so that $\int_0^\infty \phi_{\tau,\lambda}(t) dt = 1$. The first term in Eq. (2.24) describes the response of topological rearrangements to the cell shape anisotropy. The second term accounts for the shear rate due to topological rearrangements driven by cell polarity. We will refer to the second term as *active shear flow due to topological rearrangements* or simply *active shear flow*. Figure 2.1 D illustrates how the active topological rearrangements can affect cell and tissue shape. A more detailed discussion of the active shear flow is presented in Section 3.5.

For simplicity, we have employed the same nematic polarity field q_{ij} as in the equation for the shear stress Eq. (2.20). If several different polarities are present, the two active terms could couple differently to different polarities.

This constitutive equation implicitly contains the contributions of asymmetric cell divisions and extrusions. In a system where divisions and extrusions contribute significantly to the shear flows and their rates vary strongly in time, additional terms should be included containing cell division and cell extrusion rates coupled to cell elongation Q_{ij} and cell polarity q_{ij} nematic tensors.

2.6 Summary

In this chapter we presented the hydrodynamic theory we will use in this thesis to describe the flow of epithelial tissues. We first defined the cell number density n and the cell velocity v_i. Cell velocity is sufficient to describe overall tissue deformation. However, additional important information about the tissue is contained in properties of the cells that form the tissue. To relate the information contained at the cellular and subcellular scale to the coarse-grained tissue properties, we defined average cell area a, cell elongation Q_{ij} and cell polarity q_{ij}. The overall change in tissue shape and size can be decomposed into contributions from the change of cell state properties and from changes in the network topology.

Forces in the tissue are described by a two-dimensional stress. We found that in developing tissues, which are the subject of this thesis, the characteristic inertial forces are negligible as compared to the characteristic elastic forces. Therefore, we neglected inertial terms in the force balance equation.

Finally, to complete the hydrodynamic theory we introduced linear constitutive relations for shear stress $\tilde{\sigma}_{ij}$, pressure P, and shear flow due to topological rearrangements R_{ij}. These constitutive relations include memory effects as well as active terms that can intrinsically drive tissue flows.

Chapter 3

Rheology of tissue shear flow in the developing fly wing

In this chapter, we use the hydrodynamic theory developed in Chapter 2 to investigate rheology of epithelia shear flow. We study shear flow in the fruit fly wing during pupal morphogenesis. The pupal wing morphogenesis starts at around 15 hours after pupa formation (hAPF) when the hinge region of the wing starts contracting. This contraction shapes the wing blade and after another 18 hours, the wing shape resembles the shape of the adult wing [54].

We analyze the shear flow of the wing blade tissue and its cellular contributions [54, 55]. The shear rate decomposition reveals a dynamic interplay of cell elongation changes and shear due to T1 transitions while the overall tissue shear rate decays monotonically. We find that we can describe the observed relationship between the tissue shear flow and the cell shape with active T1 transitions and memory effects in the wing tissue.

Based on the experimental measurements we propose a simple constitutive relation for the tissue shear stress leading to a novel rheological equation that is capable of producing transient oscillations in the tissue shear stress. We investigate theoretically this rheological equation and find that the observed memory effects give rise to the effective inertia in the tissue rheology.

Finally, we study the active flows of the tissue, produced by the active T1 transitions and an active shear stress, under different boundary conditions. Results of this chapter have been published in refs. [54, 66].
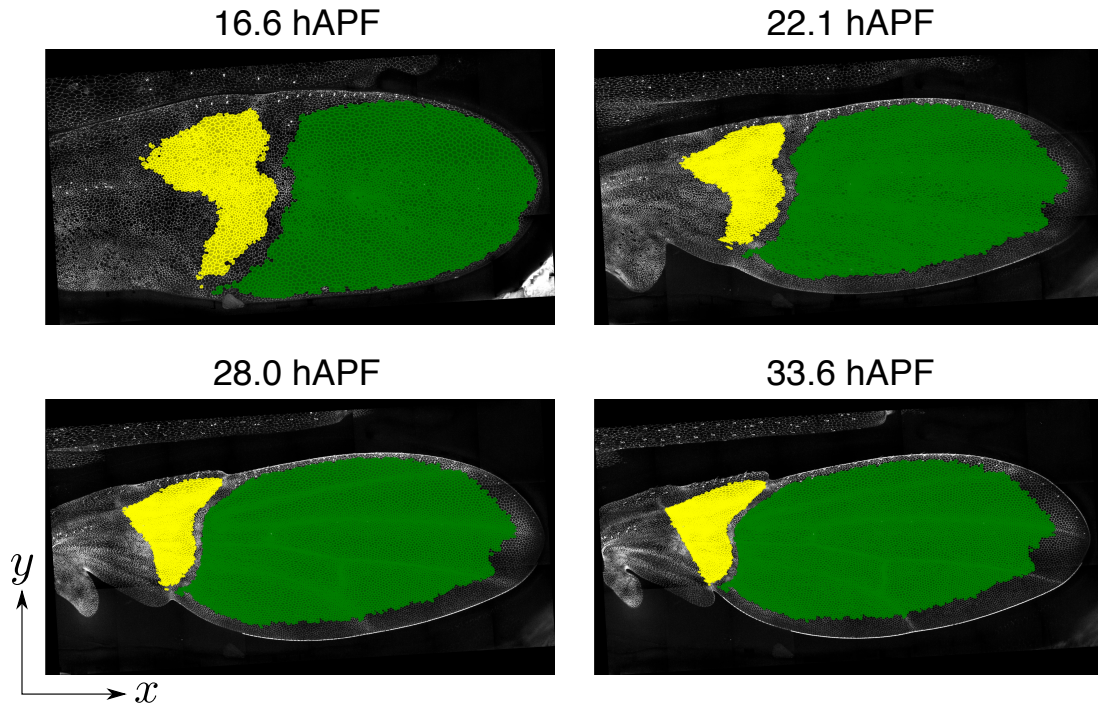
Figure 3.1: Time evolution of hinge and blade tracked regions shown at four different timepoints during pupal morphogenesis. The blade tracked region (green) is composed of cells visible throughout the observed pupal morphogenesis. The hinge tracked region (yellow) is composed of a distal collection of hinge cells.

3.1 Active interplay of cell elongation and T1 transitions during wing morphogenesis

3.1.1 Shear flow in the developing pupal wings and its cellular contributions

We measure the tissue shear rate and its cellular contributions in the *blade tracked region*. This region consists of the largest collection of blade cells that can be tracked from the beginning of the experiment (green region in Fig. 3.1). Using a tracked region allows us to measure the tissue shear rate without convective contributions. The *hinge tracked region* is shown in yellow in Fig. 3.1. It is located in the distal part of the wing hinge. Other parts of the hinge are not included because the segmentation of

cells there is prone to errors. In this chapter, we study the tissue flow in the blade tracked region.

We use the method based on the triangulation of the tissue [55] to quantify cellular contributions to the average shear rate in the blade tracked region, as described in Section 2.3.2.

We study 3 wild type wings, distally and anteriorly ablated wings, as well as the *dumpy* mutant wing. These three perturbed wings have compromised lateral connections to the surroundings. Therefore, mechanical stresses in these wings are different from the wild type ones. For more information about the experimental data see Appendix B.

We analyze the xx component of the tissue shear rate $\tilde{v}_{xx}$ and the cell elongation Q_{xx} (see Fig. 3.2). The x axis is oriented along the proximo-distal (PD) axis of the wing (see Fig. 3.1). The direction of the tissue shear flow is aligned with the long axis of the wing and the xy component of the shear flow and cell elongation are small. We do not consider them in this thesis.

We find that the blade of the wild type wings shears monotonically along the long axis of the wing (blue line in Fig. 3.2 A). At the same time, the cell elongation change DQ_{xx}/Dt (green line in Fig. 3.2 A) and the shear rate due to T1 transitions T_{xx} (red line in Fig. 3.2 A) exhibit oscillations around the overall shear rate. Interestingly, in the early part of pupal morphogenesis which lasts about 6 hours the blade cells elongate more than the overall tissue. This is balanced by the negative shear rate due to T1 transitions. Negative shear corresponds to the shear along the short wing axis, perpendicular to the direction of the positive shear. As we can see in Fig. 3.3, cell elongation component along the long wing axis Q_{xx} in wild type wings (green lines) is positive and increases in time. Therefore, the early T1 transitions actively increase the cell elongation instead of relaxing it as would be expected in a passive system.

In the later part of pupal wing morphogenesis, the cell elongation change rate and the shear due to T1 transitions reverse their directions and the cell elongation accumulated during the early pupal morphogenesis is relaxed by the T1 transitions (Fig. 3.3 green lines). However, the cell elongation does not relax completely and is maintained at a finite value.

In a *dumpy* mutant wing the cell elongation change and the shear due to T1 transi-
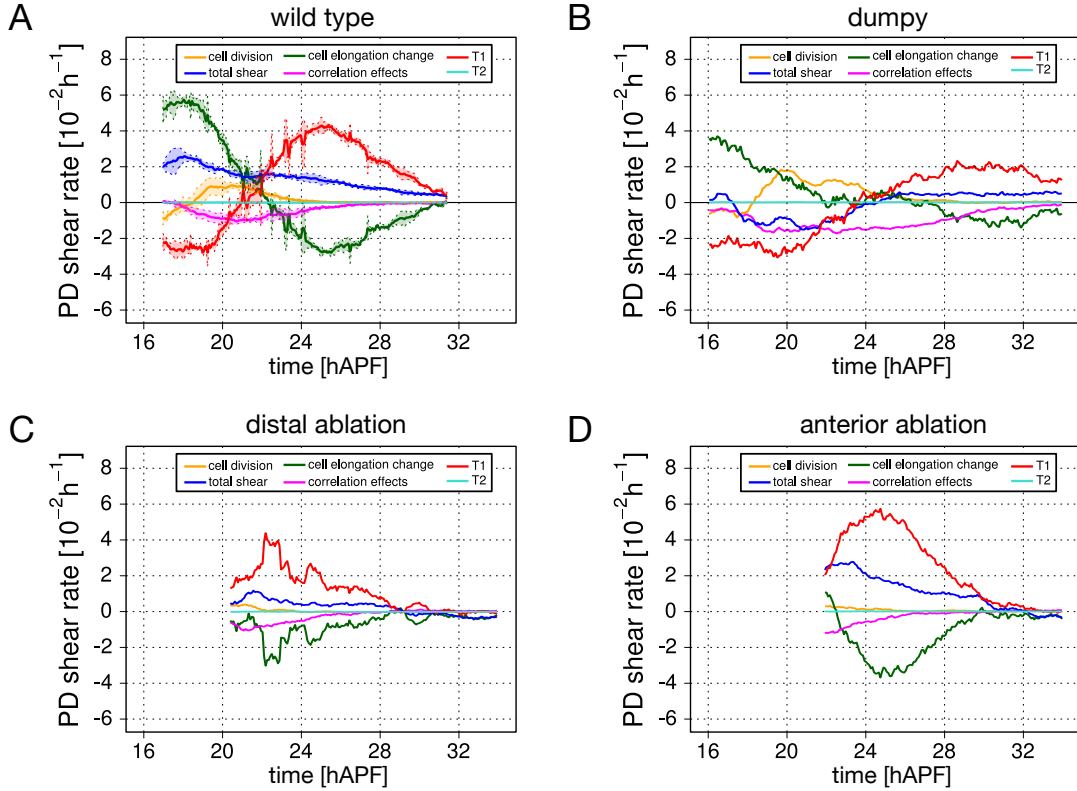
Figure 3.2: Decomposition of average tissue shear flow along the proximal-distal (PD) wing axis $\tilde{v}_{xx}$ (blue) into cellular contributions: cell elongation change (green), T1 transitions (red), cell divisions (orange), cell extrusions or T2 transitions (cyan) and correlation effects (magenta). A) lines show the average and error bars show standard deviation for 3 wild type wings. Both the overall shear rate and individual cellular contributions are reproducible among wild type wings. B) *dumpy* mutant wing. C) Distally ablated wing. D) Anteriorly ablated wing. For plotting, the data is smoothed by a moving time interval of about 50 minutes. Source: partially adapted from refs. [54] and [68]

tions show a qualitatively similar behavior as the wild type wing. However, the overall shear rate in the *dumpy* wing is negative. The experiments with mechanically perturbed wing start at a later time than the experiments with the wild type and dumpy wings. They also show a qualitatively similar behavior as the wild type wing.

Contribution to the tissue shear rate from cell divisions C_{xx}, cell extrusions E_{xx} and correlations effects D_{xx} are small and the shear rate due to topological rearrangements R_{xx} as defined in Eq. (2.15) mainly consists of the T1 transition contribution T_{xx}. To
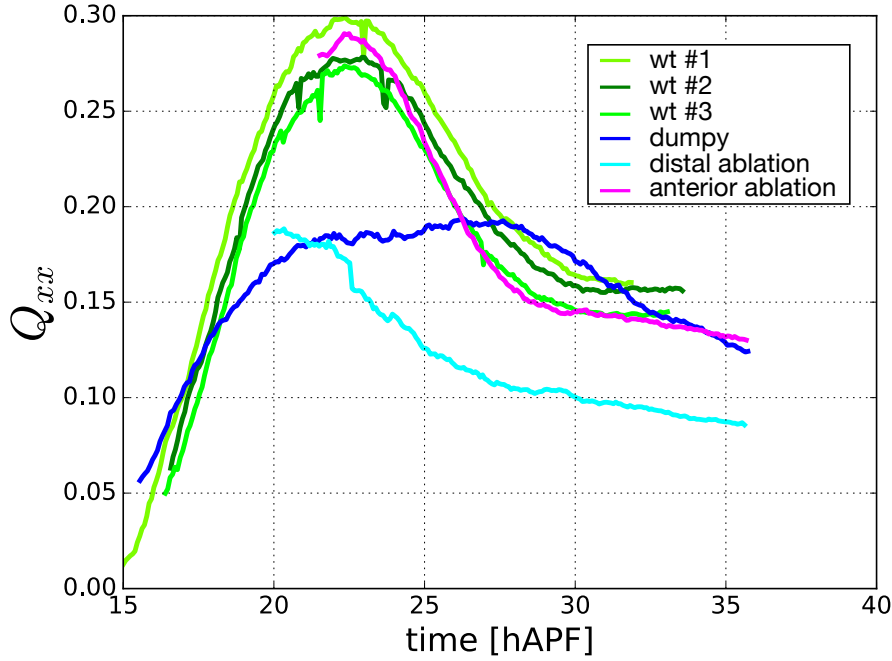
Figure 3.3: Cell elongation component Q_{xx} along the long axis of the wing. Green lines: three wild type wings. Blue line: dumpy mutant wing. Cyan line: distally ablated wing. Magenta line: anteriorly ablated wing.

simplify the analysis, in the following we study the shear rate due to topological rearrangements $R_{xx} = T_{xx} + C_{xx} + E_{xx} + D_{xx}$.

3.1.2 Constitutive equation for the shear rate due to topological rearrangements in the developing pupal wings

In Section 2.5.2 we introduced a general constitutive equation Eq. (2.24) for shear due to topological rearrangements R_{ij}. Here, we use the measurements obtained in the previous subsection to determine the particular form of constitutive equation for R_{xx} that describes fly wing shear flow.

Figure 3.4 shows shear rate due to topological rearrangements R_{xx} plotted as a function of cell elongation Q_{xx} in the blade tracked region. The time is used as a parameter and is indicated by color. This spiraling curve indicates that the memory

effects are present in the system. We will use an exponential memory kernel

$$\phi_\tau(t) = \frac{1}{\tau_d} e^{-\frac{t}{\tau_d}} \quad . \tag{3.1}$$

in the constitutive equation Eq. (2.24). Here, τ_d is a time-scale over which the memory about the cell elongation vanishes in the tissue. Also, we will use a constant active shear flow term λq_{xx} in the Eq. (2.24) so that the constitutive equation for shear rate due to topological rearrangements in the wing blade is

$$R_{xx}(t) = \frac{1}{\tau} \int_{-\infty}^{t} \frac{1}{\tau_d} e^{-\frac{t-t'}{\tau_d}} Q_{xx}(t')dt' + \lambda q_{xx} \quad . \tag{3.2}$$

It is convenient to write this equation as a differential equation

$$(1 + \tau_d \partial_t) R_{xx} = \frac{1}{\tau} Q_{xx} + \lambda q_{xx} \quad . \tag{3.3}$$
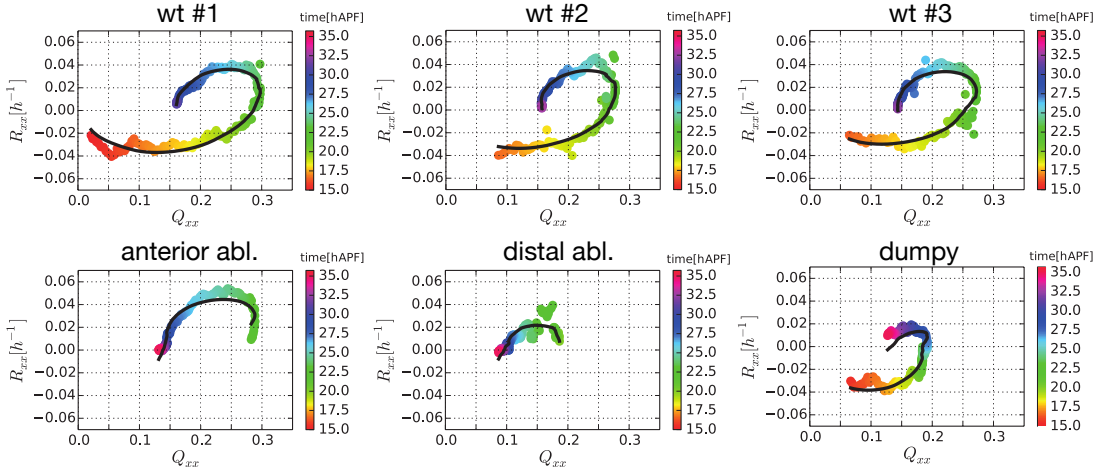
Figure 3.4: Shear rate due to topological rearrangements along the proximal-distal (PD) wing axis R_{xx} as a function of PD component of cell elongation Q_{xx} for three wild type wings, distally and anteriorly ablated wings and the dumpy mutant wing. Time of experimental data points is denoted by color. The fit of the model to the data is plotted as a black line. For plotting, the data is smoothed by a moving time interval of about 50 minutes. Source: adapted from ref. [54].

The time-scale τ was introduced in Chapter 2 as the inverse amplitude of shear due to topological rearrangements response to the cell elongation (see Eq. (2.24)). We do not have experimental information about the nematic cell polarity q_{ij}, but if we assume it does not change in time, we can set it to $q_{xx} = 1, q_{xy} = 0$. We determine values of parameters τ, τ_d and λ by jointly fitting the Eq. (3.3) to the experimental data for the three wild type wings, *dumpy* mutant wing, and anteriorly and distally ablated wings. We find that a single set of time-scales τ and τ_d describes all 6 experiments (black lines in Fig. 3.4). The active shear flow parameter λ was allowed to vary between the movies. Obtained values of parameters are reported in Table 3.1.2. Initial values of R_{xx} were treated as fit parameters.

	wt 1	wt 2	wt 3	ant. abl.	dist. abl.	dumpy
$\tau[h]$	1.6 ± 0.1					
$\tau_d[h]$	4.4 ± 0.4					
$\lambda[h^{-1}]$	-0.12 ± 0.01	-0.11 ± 0.01	-0.10 ± 0.01	-0.10 ± 0.01	-0.070 ± 0.007	-0.098 ± 0.009

Table 3.1: Parameter values obtained by fitting Eq. (3.3) to the experimental data in the tracked blade region of the wing. Uncertainties reported here are standard deviations of parameters from 1000 dataset realizations obtained by bootstraping the original datasets.

Active shear flow λ describes the active T1 transitions that drive the negative shear rate due to T1 transitions in the early pupal wing morphogenesis when the cell elongation Q_{xx} is small. Interestingly, the same active T1 transitions account for the finite value of cell elongation Q_{xx} at late times of pupal morphogenesis. To show this we consider the constitutive equation Eq. (3.3) in a steady state, when flows vanish and state variables do not change. Then, the cell elongation is determined by λ

$$Q_{xx} = -\tau\lambda \quad . \tag{3.4}$$

Therefore, the active T1 transitions maintain the finite value of the cell elongation Q_{xx} in the late pupal wing morphogenesis.

3.2 Active shear stress in the wing epithelium

Stress in overdamped systems like cytoskeleton or developing epithelial tissue can be studied by ablating the tissue with a laser and measuring the response [54, 69]. The method is based on the fact that when the dissipative forces dominate in the system, the initial deformation rate after the ablation is proportional to the stress present before the laser ablation.

Our experimental collaborators performed circular laser ablation at different places in the wing tissue at about 22.5 hAPF (see Fig. 3.5). The ablated circular regions quickly deform into ellipsoidal shapes and our collaborators measured the retraction rates $V_\parallel$ and $V_\perp$, along the long and short axes of the ellipsoidal shape of the ablated region, respectively. From these retraction rates, we construct the retraction velocity gradient tensor as follows

$$v_{ij}^{\mathrm{cut}} = \begin{pmatrix} \cos\theta & -\sin\theta \\ \sin\theta & \cos\theta \end{pmatrix} \begin{pmatrix} V_\parallel/r_\parallel & 0 \\ 0 & V_\perp/r_\perp \end{pmatrix} \begin{pmatrix} \cos\theta & \sin\theta \\ -\sin\theta & \cos\theta \end{pmatrix} \quad . \tag{3.5}$$

Here, angle θ describes the orientation of the long axis of the ablated region. The ellipsoidal shape of the ablated region at the time when the retraction velocities were determined has half-lengths of the major and minor axes $r_\parallel$ and $r_\perp$, respectively.

We plot the component of traceless symmetric part of the retraction velocity gradient along the long wing axis $\tilde{v}_{xx}^{\mathrm{cut}}$ versus the corresponding component of the cell elongation tensor Q_{xx} measured in an unperturbed wing at the location of the ablation, as shown in Fig. 3.5. We find that measurements in both wild type and *dumpy* mutant show a clear correlation between Q_{xx} and $\tilde{v}_{xx}^{\mathrm{cut}}$. Therefore, we describe the shear stress in the wing tissue with a Hookean constitutive equation

$$\tilde{\sigma}_{ij} = 2KQ_{ij} + \zeta q_{ij} \quad . \tag{3.6}$$

Parameters K and ζ have been introduced in Eq. (2.20). A linear fit to data allows us to determine $\zeta/K = 0.3 \pm 0.2$ in the wild type wing and $\zeta/K = 0.3 \pm 0.2$ in the dumpy mutant.

A similar analysis of the isotropic part of the retraction velocity gradient tensor v_{kk}^{cut}
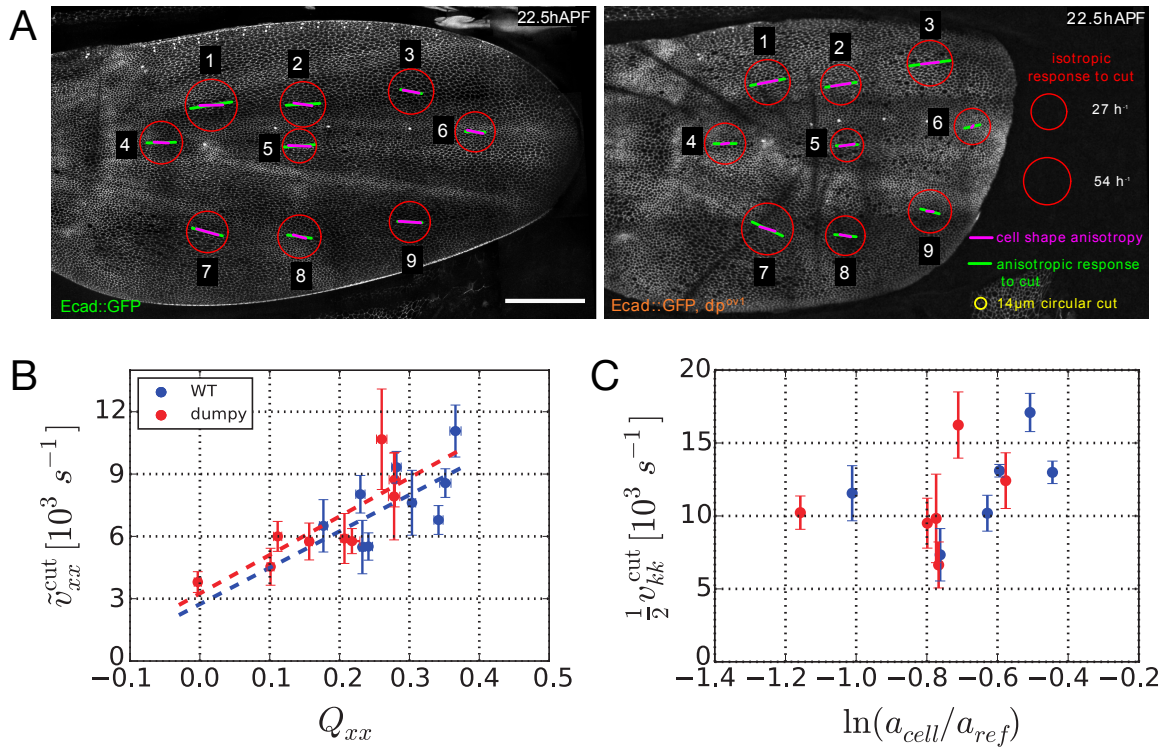
Figure 3.5: A) Circular laser ablation experiments were performed in the wild type and dumpy mutant wing. Figure shows locations at which the ablations were performed, overlayed on an image of an unperturbed wing. B) Wing tissue retraction shear component is correlated with local cell elongation. C) There is no clear correlation between the isotropic component of tissue retraction and local cell area a_{cell}. Parameter a_{ref} is introduced to make a_{cell} dimensionless and has the same value for all data points. Source: adapted from ref. [54]

does not show a clear relationship with the cell area (see Fig. 3.5 B). This could be due to the fact that the cell area strain depends on both cell area a and a preferred cell area a_0, defined in Section 2.5.1. The preferred cell area could be very dynamic and dependent on the cell division rate, but it cannot be directly measured. Circular ablation experiments measure local tissue stresses and spatial fluctuations of a_0 could indeed prevent us from extracting useful information from the isotropic part of the retraction velocity gradient tensor v_{kk}^{cut}. Properties of the preferred cell area are discussed in more detail in Chapter 5.

3.3 Transient oscillations and effective inertia due to memory effects

Dynamics of shear flow decomposition Eq. (2.16) and constitutive relations for shear due to topological rearrangements Eq. (3.2) can be schematically represented by Fig. 3.6 A. These two equations, together with the shear stress constitutive equation Eq. (3.6) allow us to relate the shear stress to the velocity gradient. In frequency domain we find

$$\tilde{\sigma}_{ij}(\omega) = 2\eta \frac{1 + i\tau_d\omega}{1 + i\omega\tau\left(1 + i\tau_d\omega\right)} \tilde{v}_{ij}(\omega) \quad , \tag{3.7}$$

where we have introduced the effective shear viscosity $\eta = K\tau$. We have omitted active terms and we discuss the properties of the response function

$$\chi(\omega) = 2\eta \frac{1 + i\tau_d\omega}{1 + i\omega\tau\left(1 + i\tau_d\omega\right)} \quad . \tag{3.8}$$

Fig. 3.6 D shows real and imaginary parts of $\chi(\omega)$ for three values of τ_d/τ.

When there is no memory in the system $\tau_d = 0$ the response function becomes

$$\lim_{\tau_d \to 0} \chi(\omega) = 2\eta \frac{1}{1 + i\omega\tau} \quad . \tag{3.9}$$

This is the Maxwell viscoelastic response to the shear deformation (red line in Fig. 3.6 D). In this limit, the time-scale τ corresponds to the Maxwell viscoelastic time-scale below which the system response is mostly elastic and beyond which the system flows as a viscous fluid. The short term elastic behavior comes from the initial elastic response of cells. It takes time τ for cells to rearrange and relax the elongation imposed by the tissue strain. Thus, the topological rearrangements fluidize the tissue on the time-scales larger than τ, and the tissue behaves as a viscous fluid with viscosity $\eta = K\tau$.

Memory time-scale can be interpreted as the time it takes for the tissue to realize that cells have changed their shape and start performing the T1 transitions. Schematic in Fig. 3.6 B illustrates the interpretation of the two time-scales.
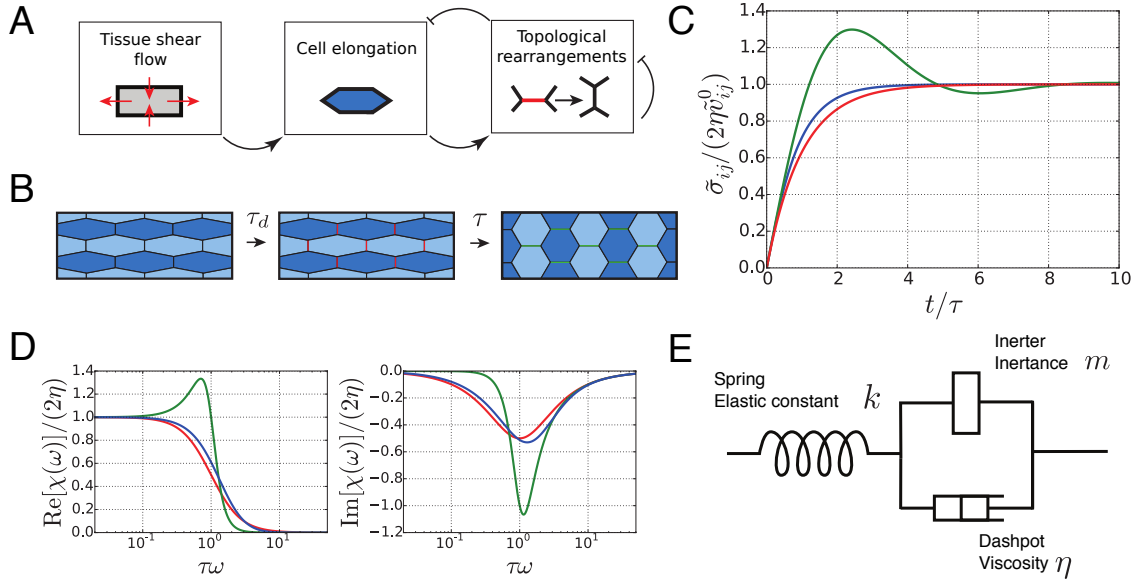
Figure 3.6: A) Schematic of the dynamical system governing the tissue shear flow. B) Interpretation of the two time-scales relevant for the dynamics of topological rearrangements. Tissue requires time τ_d to induce topological rearrangements in response to a change of cell elongation. Once topological rearrangements are induced it takes them time τ to relax the cell elongation. C) Shear stress in a tissue in response to an imposed constant shear rate at $t = 0$. When memory time-scale vanishes $\tau_d = 0$ tissue responds as a Maxwell viscoelastic material (red line). For $\tau_d/\tau = 0.2 < 1/4$ (blue line) shear stress is exponentially relaxed and for $\tau_d/\tau = 0.5 > 1/4$ (green line) shear stress exhibits damped oscillations. D) Real and imaginary components of the response function $\chi(\omega)$. Line colors correspond to the same values of τ_d/τ as in C. E) Mechanical network that reproduces the rheological response function $\chi(\omega)$. Source: ref. [66]

The response function $\chi(\omega)$ has two simple poles

$$\omega_{1,2} = \frac{i}{2\tau_d}\left[1 \pm \sqrt{1 - \frac{4\tau_d}{\tau}}\right] \quad . \tag{3.10}$$

For $\tau_d < \tau/4$ both poles lie on the positive imaginary axis. In this case, the system exhibits exponential relaxation as in the Maxwell material. However, when $\tau_d > \tau/4$ both poles become complex and the tissue exhibits damped oscillatory response. We demonstrate this in an example where at $t = 0$ a constant tissue shear rate $\tilde{v}_{ij}^0$ is

imposed on the tissue. The tissue stress is then given by

$$\tilde{\sigma}_{ij}(t) = 2\eta\tilde{v}_{ij}^0 \left[1 - e^{t/(2\tau_d)} \left(\frac{1-\beta^2}{2\beta} \sin\left(\beta\frac{t}{2\tau_d}\right) + \cos\left(\beta\frac{t}{2\tau_d}\right) \right) \right] \quad , \qquad (3.11)$$

where

$$\beta = \sqrt{\frac{4\tau_d}{\tau} - 1} \quad . \qquad (3.12)$$

For a real β the shear stress exhibits damped oscillations. For an imaginary β the shear stress relaxes exponentially to the equilibrium value (Fig. 3.6 C). Values of parameters we found in Section 3.1.2 correspond to $\tau_d/\tau \sim 2.5$. Therefore, during pupal morphogenesis, the wing blade tissue exhibits damped oscillatory response to an imposed shear rate.

Rheological response functions are usually represented by mechanical networks of springs and dashpots. However, the response function Eq. (3.8) cannot be reproduced by a mechanical network composed of springs and dashpots. We prove this by analyzing the real and imaginary parts of the response function

$$\mathrm{Re}\left[\chi(\omega)\right] = 2\eta \frac{1}{(\tau\omega)^2 + (1 - \tau\tau_d\omega^2)^2} \qquad (3.13)$$

$$\mathrm{Im}\left[\chi(\omega)\right] = -2\eta\omega \frac{\tau - \tau_d + \tau\tau_d^2\omega^2}{(\tau\omega)^2 + (1 - \tau\tau_d\omega^2)^2} \quad . \qquad (3.14)$$

We note that the imaginary part of the response function $\chi(\omega)$ can become positive for $\tau_d > \tau$. However, a network composed of only springs and dashpots cannot produce a response function with a positive imaginary part.

This can be proved as follows. Let two rheological elements with response functions $\chi_1(\omega)$ and $\chi_2(\omega)$ both have equal signs of the real part of their response functions and equal signs of the imaginary parts. Then, both serial and parallel connections of these two elements will have the same signs of real and imaginary parts as the two rheological elements they were constructed from, see Appendix C.1 for proof. Since the response function of spring with elastic constant k and dashpot with viscosity $\bar{\eta}$

are

$$\chi_{\text{spring}}(\omega) = -i\frac{k}{\omega} \tag{3.15}$$

$$\chi_{\text{dashpot}}(\omega) = \overline{\eta} \tag{3.16}$$

we can conclude that the response function of any mechanical network made of springs and dashpots has a non-positive imaginary part. Since the Eq. (3.14) can become positive we conclude that the response function $\chi(\omega)$ cannot be reproduced by springs and dashpots.

The Bott Duffin synthesis theorem for electrical circuits states that the response function whose Laplace transform is a positive real function can be reproduced by a network of resistors, capacitors and inductors. A positive real function is a rational complex function of complex variable z that has real values for $\text{Im}(z) = 0$ and has a positive real part for $\text{Re}(z) > 0$. The Laplace transform of the response function $\chi(\omega)$ is

$$\tilde{\chi}(s) = 2\eta\frac{1 + \tau_d s}{1 + \tau s \left(1 + \tau_d s\right)} \tag{3.17}$$

and it is easy to see that it is indeed a positive real function. Therefore, the response function χ can be reproduced by an electrical network consisting of resistors, capacitors and inductors.

Analogy between mechanical networks and electrical circuits can be made by identifying the electrical current with the shear stress and electrical potential with the shear rate. In this analogy resistor and inductor in electrical circuits correspond to dashpot and spring in the mechanical networks. The mechanical element corresponding to a capacitor has an inertial response to the deformation rate and it is called *inerter* [70]. Note that an inerter is not a simple mass element as it has to respond inertially to the relative movement of its two endpoints in a mechanical network. A simple mass responds inertially to the movement of its center of mass relative to an inertial frame of reference and thus it corresponds to a grounded capacitor in electrical circuits.

The mechanical response function of an inerter is $\chi_{\text{inerter}} = i\omega m$ where m is called *inertance* [70]. Now, it is straightforward to find the mechanical network equivalent

to the response function $\chi(\omega)$. It is composed of a parallel connection of an inerter of inertance $m = 2K\tau\tau_d$ in parallel with a dashpot with viscosity $\overline{\eta} = 2K\tau$ and this parallel connection is connected in series with a spring with elastic constant $k = 2K$ (see Appendix C.2 and Fig. 3.6 E). The inertance of the wing tissue can be estimated from the measured values of time-scales τ and τ_d, assuming a typical three-dimensional elastic modulus of cells $K_{3D} = 10Pa$ and a characteristic cell size to be $l = 10\mu m$. We find $m = 2K_{3D}l\tau\tau_d \sim 2 \cdot 10^4 kg$. This value is 12 orders of magnitude larger than the estimate for wing mass $m_{\mathrm{wing}} \sim 1.6 \cdot 10^{-8} kg$ we made in Section 2.4. Therefore, the inertial response is not related to the inertia of the wing and arises from the memory effects in the system.

3.4 Shear flow of a viscoelastic nematic gel close to equilibrium

It is interesting to compare tissue shear flow and the shear flow of viscoelastic nematic gel close to equilibrium. In Appendix D we derive constitutive equations that govern such viscoelastic nematic gel using Onsager theory. A very similar derivation is presented in ref. [53] and we have adapted it for a nematic gel.

Cell elongation in a tissue corresponds to the local elastic shear strain in a gel. Interestingly, an equation that is equivalent of the shear decomposition Eq. (2.16) holds in gels [53] (see Appendix D). This allows us to define the tensor R_{ij} in gels and to derive the dynamical equation

$$\left(1 + \tau_d\frac{D}{Dt}\right) R_{ij} = \frac{1}{\tau}Q_{ij} + \alpha\frac{DQ_{ij}}{Dt} \quad . \tag{3.18}$$

In this chapter, we have used $\alpha = 0$ to describe tissue shear flow. In Appendix D.1.1 we show that if $\alpha = 0$ in a passive gel, the inequality $\tau \geq 4\tau_d$ holds. Therefore, a passive gel with $\alpha = 0$ cannot exhibit the damped oscillations we found in the pupal wing. However, we show in Appendix D.1.2 that in an active gel this constraint does not apply and constitutive equation Eq. (3.3) for tissue shear flow can also describe shear flows in an active viscoelastic nematic gel.

These results show that the mechanics of tissue shear flow is closely related to the

shear flow of a viscoelastic nematic gel. In particular, equations governing the shear flow of an active gel can be mapped to the equations that govern tissue shear flow.

3.5 The role of boundary conditions in active tissue shear flow

Earlier in this chapter, we have found that two distinct active cellular processes are present during the pupal wing morphogenesis. In this section, we study tissue shear flow driven by the active shear stress ζ and active shear flow λ under different boundary conditions. Active shear flow λ describes the flow produced by active topological rearrangements of cells.

We consider a homogeneous rectangle tissue (Fig. 3.7 A) with a uniform polarity field q_{ij} oriented along the x axis. Tissue dynamics is governed by constitutive equations Eq. (3.3) and Eq. (3.6), and it is constrained by elastic springs. The elastic springs set the boundary conditions for the stress in the tissue. Since we consider a homogeneous rectangle tissue, values of the stress components are constant in space and correspond to their boundary values

$$\sigma_{xx} = -kL \tag{3.19}$$

$$\sigma_{yy} = -kH \quad . \tag{3.20}$$

Here, k is the elastic constant of the springs and L and H are natural strains

$$L = \ln \frac{l}{l_0} \tag{3.21}$$

$$H = \ln \frac{h}{h_0} \quad , \tag{3.22}$$

where l and h are length and width of the tissue. l_0 and h_0 are the corresponding resting length and width. Using the elastic boundary conditions allows us to investigate the whole spectrum between free ($k = 0$) and rigid ($k \to \infty$) boundary conditions.

We consider the following situation. For $t < 0$, the tissue is at rest and $L, H, \zeta, \lambda = 0$. At the moment $t = 0$ values of ζ and λ are set to a finite constant value. We determine

the dynamics of the tissue flow, tissue shape and cell elongation component Q_{xx} for $t > 0$

$$v_{xx}(t) = 4\frac{\gamma}{s\mu}\left(1 + \frac{\zeta}{2K\tau\gamma}\frac{\nu}{\mu}\right)e^{-t/(2\tau_d)}\sin\frac{s}{2\tau_d}t - \frac{\zeta}{\mu K}\delta(t) \tag{3.23}$$

$$L(t) = \gamma\frac{2\tau}{\nu}\left[1 - \left(1 + \frac{\zeta}{2\tau K\gamma}\frac{\nu}{\mu}\right)e^{-t/(2\tau_d)}\left(\frac{1}{s}\sin\frac{s}{2\tau_d}t + \cos\frac{s}{2\tau_d}t\right)\right] \tag{3.24}$$

$$H(t) = -L(t), \tag{3.25}$$

$$Q_{xx}(t) = \frac{1}{2K}\left(-kL(t) - \zeta\right) \quad . \tag{3.26}$$

For derivation see Appendix E. We have introduced parameter

$$\gamma = \lambda - \frac{\zeta}{2K\tau} \quad , \tag{3.27}$$

which determines the deformation accumulated after a long time. Parameter

$$s = \sqrt{4\frac{\tau_d}{\tau}\frac{\nu}{\mu} - 1} \tag{3.28}$$

determines whether the system exhibits transient oscillations for a real s, or a simple exponential relaxation for an imaginary s. Finally, values of parameters

$$\mu = 2\left(1 + \frac{k}{2K}\right) \tag{3.29}$$

$$\nu = \frac{k}{K} \tag{3.30}$$

depend on the elasticity of the springs.

Now, we discuss the behavior of this system in three cases: free boundary conditions for $k/K = 0$, rigid boundary conditions for $k/K \to \infty$ and elastic boundary conditions for a finite k/K.

When the boundary conditions are free $\nu = 0$ and $\mu = 2$. Therefore, $s = i$ is always imaginary and the tissue shape always relaxes exponentially to the steady state. Both ζ and λ contribute to the steady state tissue flow through parameter γ. However, cell elongation reaches a steady state value $Q_{xx} = -\zeta/(2K)$, independent of λ. Tissue shear rate and cell elongation dynamics are shown in Fig. 3.7 left.
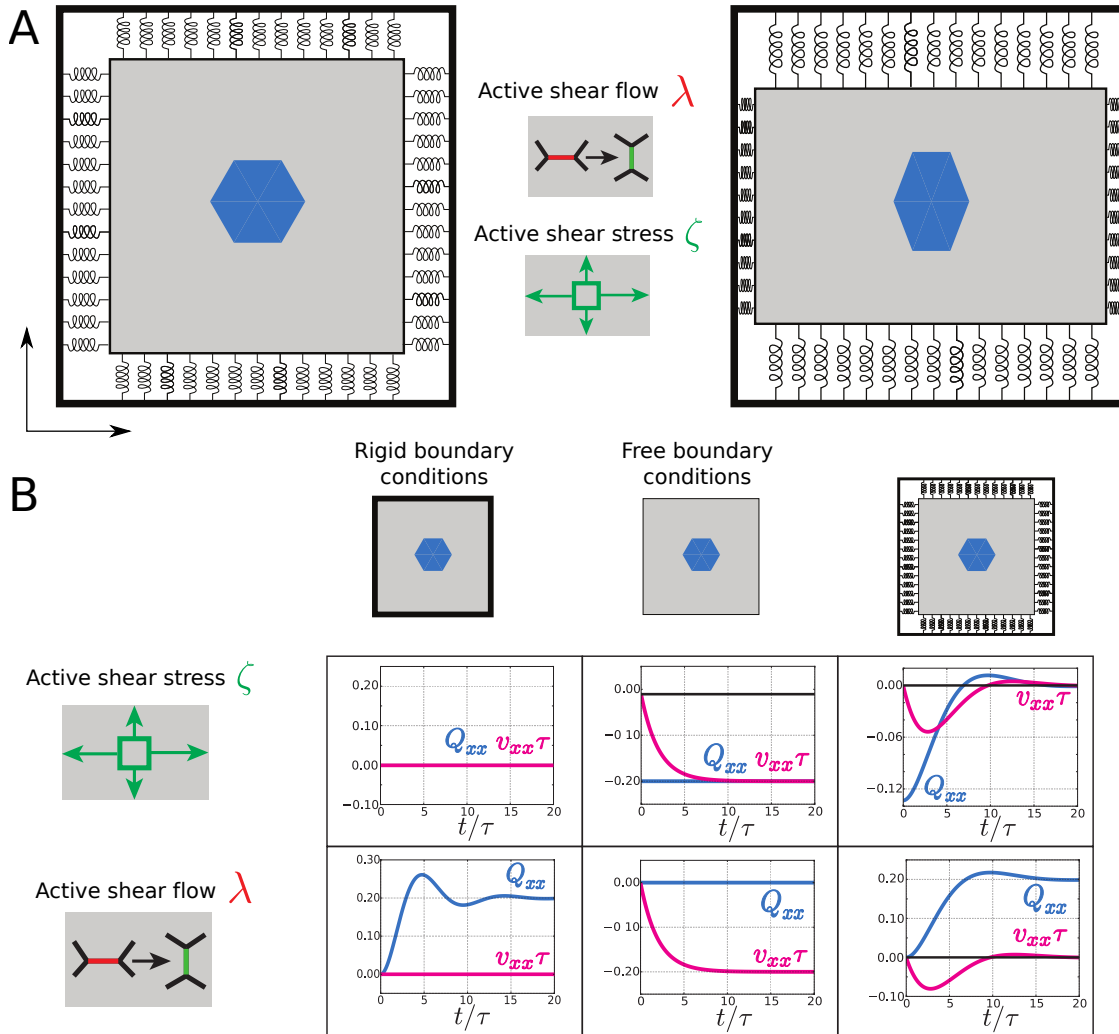
Figure 3.7: A) A homogeneous rectangle tissue flow is driven by the active cellular processes: active shear stress ζ and active shear flow λ. B) Dynamics of the tissue shear rate and cell elongation in a rectangular tissue, subjected either to active stress ($\zeta = 0$ and $\lambda \neq 0$, top row) or to active shear flow ($\zeta \neq 0$, $\lambda = 0$, bottom row), under different boundary conditions. The active shear stress and active shear flow give rise to different dynamics of cell elongation and tissue flow. The parameter γ that controls the shear rate magnitude is set to be the same in all cases: $\gamma\tau = \lambda\tau - \zeta/(2K) = -0.2$. Other parameters used are $\tau_d/\tau = 2$ and in the third column, the spring constant is $k/K = 1$. Note that a Dirac delta peak at $t = 0$ in $v_{xx}(t)$ is not shown in the plots. Source: adapted from ref. [66]

When the boundary conditions are rigid tissue cannot deform. Both ν and μ diverge but their ratio is $\nu/\mu = 1$. This is also the maximal value ν/μ can obtain. Although tissue does not flow, active shear flow λ drives the cell elongation until the value $Q_{xx} = -\lambda\tau$ is reached. Tissue shear rate v_{xx} and cell elongation Q_{xx} are shown in Fig. 3.7 middle.

For the elastic boundary conditions parameter s can always be made purely imaginary and oscillations can be removed by sufficiently reducing the elasticity of the springs. However, since $\nu/\mu < 1$, it is not always possible to induce oscillations by making the springs stiffer. The cell elongation reaches the same final values as in the case of the rigid boundary conditions $Q_{xx} = -\lambda\tau$. Tissue shear rate and cell elongation dynamics are shown in Fig. 3.7 right.

Both active processes can induce tissue shear flows when the boundary conditions allow it. To distinguish the two active processes in an experiment, it is not sufficient to measure the shear rate $\tilde{v}_{xx}$ but it is necessary to also measure the cell elongation Q_{xx}.

Finally, it is interesting to compare parameter s with the parameter β defined in Eq. (3.12). They both control oscillations in the tissue but they are not the same

$$s^2 = \frac{\nu}{\mu}\left(\beta^2 + 1\right) - 1 \quad . \tag{3.31}$$

The reason for this is that β is relevant in a system in which tissue shear rate is imposed. Thus, β and s are identical when the springs are infinitely stiff and the tissue shear is imposed to be 0. On the other hand, a situation in which the springs are removed and $\nu/\mu = 0$ corresponds to an imposed shear stress. The response of tissue shear rate to an imposed stress is described by a response function $\chi_\sigma(\omega) = 1/\chi(\omega)$. This response function has a single imaginary pole and thus, as we have already found, no oscillations are present in the tissue. Therefore, parameter s provides a more general criterion for the presence of oscillations in the tissue than β. It includes not only systems in which the shear rate or the shear stress are imposed, but also the whole spectrum of systems with elastic boundary conditions.

3.6 Summary

In this chapter, we studied rheology of shear flow in epithelial tissues. We quantified cellular contributions to the shear flow in the wild type fruit fly wing as well as in the wings that were either mechanically or genetically perturbed. We found that the relationship between tissue shear flow due to topological rearrangements and cell elongation exhibits an interesting interplay arises from the active T1 transitions and an exponentially decaying memory in the tissue.

We analyzed circular laser ablation experiments to determine the relationship between tissue shear stress and cell elongation. Interestingly, we found that the relationship is very similar in the wild type and the dumpy mutant wing and we found a finite value of active shear stress ζ.

We then studied the response function of shear stress to the shear flow rate of the tissue. We found that when the memory time-scale in the tissue is sufficiently large, the memory effects give rise to damped oscillations of the shear stress. This memory gives rise to the inertial part of the rheological response which can be reproduced by a simple mechanical network that includes an inerter element. We also briefly discussed similarities between tissue shear flow and the shear flow of an active viscoelastic nematic gel close to equilibrium.

Finally, we demonstrated how the two different active processes present in the pupal wing influence tissue flow and cell shape. We discussed active tissue flow in the presence of different boundary conditions and determined how different boundary conditions affect the tissue rheology and the dynamics of cell shape.

Chapter 4

Spontaneous rotations of actively coupled nematics

Biological cells are seldom isotropic. Their shape, membrane properties and internal structure typically show both vectorial and nematic anisotropy. In Chapter 2 we introduced two such order parameters relevant on the tissue scale: cell elongation tensor Q_{ij} and internal cell polarity q_{ij}. In this chapter, we investigate general properties of a system of two active coupled nematic objects. They can represent individual cells or homogeneous fields. We present the results obtained for nematic objects (nematics) but the same results hold for vectors, up to a numerical prefactor.

In a passive system, interactions between two nematics would either align or oppose them. However, biological systems are out of equilibrium and the coupling parameters between two nematics in biological tissue can explore a bigger parameter space. We find that in the region of parameters not accessible to a passive system both aligned and opposed configurations of the two nematics can become unstable and the system spontaneously rotates. A similar transition to a spontaneously oscillating state was found in an active nematic fluid where the nematic order parameter is coupled to the strain rate tensor [71].

4.1 Soft and hard nematics

We distinguish two types of nematics based on their response to an external field. The first type we call a *soft nematic* and denote it by Q_{ij}. It obeys the following

dynamical equation

$$\partial_t Q_{ij} = -\frac{1}{\tau} Q_{ij} + \nu \lambda_{ij} \quad , \tag{4.1}$$

where τ is the relaxation time-scale, λ_{ij} is an external nematic field and ν is a coupling constant between the nematic and the external field. The magnitude of a soft nematic relaxes to 0 in the absence of an external field. In the presence of an external field λ_{ij}, a soft nematic is proportional to the external field $Q_{ij} = \tau \nu \lambda_{ij}$.

The second type of nematics we consider we call *hard nematics*. Their magnitude q is constant and they respond to an external field by changing their orientation angle

$$\partial_t \varphi = -\frac{\mu \lambda}{2q} \sin\left(2\varphi - 2\theta_\lambda\right) \quad . \tag{4.2}$$

Here, φ is the nematic orientation angle, θ_λ is the orientation angle of the external field λ_{ij}, λ is the external field strength and μ is a coupling parameter.

In a biological tissue, an example of a soft nematic is cell elongation that relaxes to its equilibrium value in absence of an imposed stress. An example of a hard nematic could be a spontaneously generated anisotropy of proteins in a cell that can reorient but does not change in magnitude.

4.2 Dynamics of coupled soft and hard nematic

In this chapter, we discuss dynamics of a system composed of one soft nematic Q_{ij} interacting with one hard nematic q_{ij}. They interact with each other in the same way they would with an imposed external field. In polar components the dynamics of the coupled system is

$$\partial_t Q = -\frac{1}{\tau} Q + \nu q \cos\left(2\psi - 2\varphi\right) \tag{4.3}$$

$$\partial_t \psi = -\frac{\nu}{2} \frac{q}{Q} \sin\left(2\psi - 2\varphi\right) \tag{4.4}$$

$$\partial_t \varphi = -\frac{\mu}{2} \frac{Q}{q} \sin\left(2\varphi - 2\psi\right) \quad , \tag{4.5}$$

where Q and ψ are the magnitude and the orientation angle of the soft nematic, respectively, φ is the angle of the hard nematic and ν and μ are the coupling constants as introduced in the previous section.

4.2.1 Passive coupling

Now we show that the dynamical Eqs. (4.3)-(4.5) describe relaxation of a passive system to an equilibrium state if a particular constraint on coefficients μ and ν is imposed.

Consider a passive system with a free energy

$$F(Q_{ij}, q_{ij}, B) = \frac{1}{2}CQ_{ij}Q_{ij} + DQ_{ij}q_{ij} + B\left(q_{ij}q_{ij} - 1\right) \quad , \tag{4.6}$$

where C is a positive constant, D is interaction parameter and B is a Lagrange multiplier used to impose the constraint $|q_{ij}| = 1$. Relaxation to equilibrium state is described by

$$\gamma_Q \partial_t Q_{ij} = -\frac{\delta F}{\delta Q_{ij}} = -CQ_{ij} - Dq_{ij} \tag{4.7}$$

$$\gamma_q \partial_t q_{ij} = -\frac{\delta F}{\delta q_{ij}} = -2Bq_{ij} - DQ_{ij} \tag{4.8}$$

$$|q_{ij}| = 1 \quad , \tag{4.9}$$

where γ_Q and γ_q are positive constants. Mapping $C/\gamma_Q \to 1/\tau$, $-D/\gamma_Q \to \nu$ and $-D/\gamma_q \to \mu$ relates this passive system with the dynamical system Eqs. (4.3)-(4.5). However, since $\gamma_Q, \gamma_q > 0$ the following constraint

$$\mu\nu = D^2 \gamma_Q \gamma_q > 0 \tag{4.10}$$

holds in a passive system.

4.2.2 Arbitrary coupling

We now proceed to investigate the behavior of a coupled soft and hard nematic with arbitrary coupling constants. We use Eq. (4.10) to distinguish parameter regimes that

are accessible to a passive system from those that a passive system cannot reach.

The system described by Eqs. (4.3)-(4.5) is rotationally invariant and only the angle difference is relevant for the dynamics. Therefore, we can reduce the number of relevant dimensions by introducing variables

$$\xi = \psi - \varphi \tag{4.11}$$

$$\zeta = \psi + \varphi \quad . \tag{4.12}$$

Now we write the system of Eqs. (4.3)-(4.5) in a dimensionless form

$$\partial_t Q = -Q + \tilde{\nu} \cos 2\xi \tag{4.13}$$

$$\partial_t \xi = -\frac{1}{2} \left(\tilde{\nu} \frac{1}{Q} + \tilde{\mu} Q \right) \sin 2\xi \tag{4.14}$$

$$\partial_t \zeta = -\frac{1}{2} \left(\tilde{\nu} \frac{1}{Q} - \tilde{\mu} Q \right) \sin 2\xi \quad . \tag{4.15}$$

Here we have expressed time in units of τ and defined dimensionless parameters $\tilde{\nu} = \nu\tau$ and $\tilde{\mu} = \mu\tau$. We have also set $q = 1$. Dynamics of this system is completely described by Eqs. (4.13) and (4.14). The Eq. (4.15) only determines the behavior of the sum of the angles.

It is worth noting that a dynamical system described by Eqs. (4.13) and (4.14) is similar to the dynamical system of nematic order parameter and shear strain rate tensor found in an active nematic fluid [71] and to a FitzHugh model [72]. FitzHugh model is a special case of Hodgkin-Huxley model for the propagation of action potential in neurons [73]. Differences between these models and our system come from the fact that Eqs. (4.13) and (4.14) describe nematics in two dimensions and that the magnitude of hard nematic q_{ij} is constant.

We look for the steady state solutions Q_S and ξ_S of Eqs. (4.13) and (4.14)

$$Q_S - \tilde{\nu} \cos 2\xi_S = 0 \tag{4.16}$$

$$\left(\tilde{\nu} \frac{1}{Q_S} + \tilde{\mu} Q_S \right) \sin 2\xi_S = 0 \quad . \tag{4.17}$$

This system has four solutions. The first two solutions satisfy $\sin \xi_{S1,2} = 0$. They

correspond to the states in which the two nematics are oriented either in the same direction

$$\xi_{S1} = 0 \tag{4.18}$$

$$Q_{S1} = \tilde{\nu} \quad , \tag{4.19}$$

or in perpendicular directions

$$\xi_{S2} = \frac{\pi}{2} \tag{4.20}$$

$$Q_{S2} = -\tilde{\nu} \quad , \tag{4.21}$$

as shown in Fig. 4.1. Note that since $Q > 0$ only one of these two solutions is available for a particular choice of a coupling constant $\tilde{\nu}$. In these two steady states $\sin 2\xi_S = 0$ and the sum of the vector angles does not change in time.

The second two solutions are

$$\cos 2\xi_{S3,4} = \frac{1}{\tilde{\nu}}\sqrt{-\frac{\tilde{\nu}}{\tilde{\mu}}} \tag{4.22}$$

$$Q_{S3,4} = \sqrt{-\frac{\tilde{\nu}}{\tilde{\mu}}} \quad . \tag{4.23}$$

Both are represented by the right schematic in Fig. 4.1. These solutions appear simultaneously and are available when $\tilde{\nu}\tilde{\mu} < -1$. Therefore, they are unavailable in a passive system. Unlike in the first two solutions, $\sin 2\xi_S$ does not vanish and the sum of the two nematic angles ζ will grow indefinitely as described by the Eq. 4.15.

4.2.3 Stability of steady states

We now discuss properties of the four steady states in different regions of parameter space. In the region of parameters where $\tilde{\nu}\tilde{\mu} > -1$ only one steady state solution exists and it is one of the first two solutions. When $\tilde{\nu} > 0$ the nematics are aligned and when $\tilde{\nu} < 0$ they are opposed (red and green Fig. 4.2 A). However, inside the region of parameters defined by $\tilde{\nu}\tilde{\mu} < -1$ one of the first two solutions is still available

$\tilde{\mu}\tilde{\nu} > -1$		$\tilde{\mu}\tilde{\nu} < -1$
$\tilde{\nu} > 0$	$\tilde{\nu} < 0$	
$\xi_S = 0$	$\xi_S = \frac{\pi}{2}$	$\cos 2\xi_S = \frac{1}{\tilde{\nu}}\sqrt{-\frac{\tilde{\nu}}{\tilde{\mu}}}$
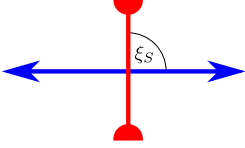
Figure 4.1: Steady state solutions of interacting soft (blue) and hard (red) nematics. For $\tilde{\mu}\tilde{\nu} > -1$ the only solutions are nematics that are not moving and are either aligned $\xi_S = 0$ or perpendicular $\xi_S = \pi/2$. For $\tilde{\mu}\tilde{\nu} < -1$ the two stable steady state solutions correspond to uniformly rotating nematics with a constant angle between them that satisfies $\cos 2\xi_S = \sqrt{-(\tilde{\nu}/\tilde{\mu})}/\tilde{\nu}$.

and the two new solutions appear (blue in Fig. 4.2 A).

We perform the linear stability analysis to determine the stability of each steady state solution. Dynamics of a perturbation from a steady state solution $\delta Q = Q - Q_S$, $\delta\xi = \xi - \xi_S$ close to the steady state is given by

$$\partial_t \begin{pmatrix} \delta Q \\ \delta\xi \end{pmatrix} = \begin{pmatrix} -1 & -\tilde{\nu}\sin 2\xi_S \\ \left(\tilde{\nu}\frac{1}{Q_S} - \tilde{\mu}Q_S\right)\frac{\sin 2\xi_S}{Q_S} & -\left(\tilde{\nu}\frac{1}{Q_S} + \tilde{\mu}Q_S\right)\cos 2\xi_S \end{pmatrix} \begin{pmatrix} \delta Q \\ \delta\xi \end{pmatrix} \qquad (4.24)$$

For the first two steady states, the eigenvalues of the stability matrix are $\gamma_1 = -1$ and $\gamma_2 = -1 - \tilde{\mu}\tilde{\nu}$. Therefore, they are stable only in the region of parameters where they are the only solutions $\tilde{\mu}\tilde{\nu} > -1$. For the other two steady states, the eigenvalues are

$$\gamma_{1,2} = -\frac{1}{2}\left(1 \pm \sqrt{9 + 8\tilde{\mu}\tilde{\nu}}\right) \quad, \qquad (4.25)$$

so that these solutions are stable whenever they exist. Interestingly, at parameters value $\tilde{\mu}\tilde{\nu} = -9/8$ (orange line in Figure 4.2 A) the eigenvalues become complex and the real part remains negative. Therefore, the stability of steady states does not change

at that point but above this value $-9/8 < \tilde{\mu}\tilde{\nu} < -1$ the steady state is a stable node and for $\tilde{\mu}\tilde{\nu} < -9/8$ it becomes a stable spiral.
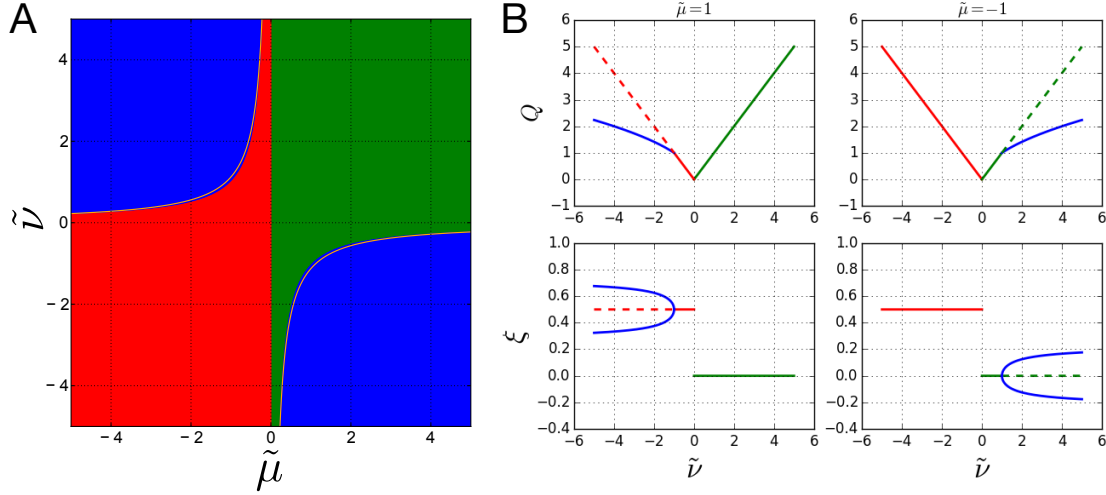
Figure 4.2: A) Parameter space regions corresponding to different stable steady state solutions. Green: nematics are oriented in the same direction and do not rotate. Red: nematics are oriented in perpendicular directions and do not rotate. Blue: nematics are under an angle ξ that satisfies $\cos 2\xi = \sqrt{(-\tilde{\nu}/\tilde{\mu})}/\tilde{\nu}$ and rotate together. Orange line denotes the transition between the parameter region where the stable steady state solution is a stable node and the parameter region where it is a stable spiral. B) Bifurcation diagram of transitions between rotating (blue) and non-rotating solutions (red and green) reveals a supercritical pitchfork bifurcation at the critical value of parameter $\tilde{\nu}_c = 1/\tilde{\mu}$ for a given value of parameter $\tilde{\mu}$.

In the second two steady states $\sin 2\xi_0$ is not zero

$$|\sin 2\xi_0| = \sqrt{1 + \frac{1}{\tilde{\nu}\tilde{\mu}}} \tag{4.26}$$

and the sum of the nematic angles grows is time according to

$$\zeta = \zeta_0 \pm \sqrt{-1 - \tilde{\nu}\tilde{\mu}}t \quad . \tag{4.27}$$

This corresponds to a uniform rotation of nematics with angular frequency $\omega = \frac{\sqrt{-1-\tilde{\nu}\tilde{\mu}}}{\tau}$. Sign of $\zeta - \zeta_0$, corresponding to the direction of rotation, is not determined by the dynamics of the system but rather by the initial conditions.

Figure 4.2 A shows a phase diagram of stable steady states in the parameters space.

In green and red regions the first two steady state solutions where the nematics are aligned/perpendicular are stable. The steady states in which two nematics rotate together exist and are stable only in blue regions. The first two steady states exist in the blue regions but are not stable. At the boundary of blue regions in Fig. 4.2 A system exhibits a supercritical pitchfork bifurcation in which one of the first two steady states loses stability and two new stable steady states appear as shown in Fig. 4.2 B.

4.3 Summary

In this chapter, we studied a system of two interacting nematic objects. In particular, we were interested in a system of one soft and one hard nematic. If such system is active it can enter a regime in which the two nematics rotate uniformly. We determined parameter regions in which such solutions are available and we discussed the stability of different steady state solutions. We found that for any choice of parameters a steady state solution is present in which nematics are either aligned or perpendicular. However, in the region of parameters where the rotating solutions are available the aligned and perpendicular solutions become unstable.

Chapter 5

Mechanics of cell divisions and cell extrusions in the pupal wing

During fruit fly pupal morphogenesis, the shape of the wing blade region changes significantly. However, at the same time, the area of the wing blade is almost unchanged although cells in the wing blade undergo 1 to 2 rounds of cell divisions [54]. In this chapter, we quantify the area growth of the developing wing epithelium during pupal morphogenesis to investigate mechanical properties of cells that undergo cell division and cell extrusion.

Several models that describe how tissues can respond to mechanical forces by regulating cell proliferation and maintaining homeostasis have been proposed [16, 42, 74–76]. Here, we propose a mechanosensitive model for the cell extrusion rate in the developing pupal fly wing. We find that a single set of parameters provides a reasonable description for wild type wings and a range of genetic, temperature and mechanical perturbations. This suggests that mechanical signaling can have a strong influence on the cell extrusion process. In a *dumpy* mutant wing, the cell extrusion rate exhibits a significantly different behavior than the extrusion rate in other experiments and cannot be accounted for by our mechanosensitive model. This implies that other extrusion mechanisms are present in the *dumpy* mutant wing.

Part of the data presented here has been published in ref. [54].

5.1 How can cells divide without increasing the tissue size?

During pupal morphogenesis, cells in the wing blade undergo 1 to 2 rounds of cell divisions with an average life cycle of about 5.8 hours. The number of cells in the blade of the wild type wing increases from around 4500 to almost 10000 [54]. How can the tissue area stay almost the same with more than a double number of cells in the tissue?

To answer this question we analyze the blade tracked region, described in Section 3.1 and shown in green in Fig. 3.1. We decompose the relative change rate of the blade tracked region area into its cellular contributions as in Eq. (2.13). The relative change rate of tissue area in the blade region is a sum of the relative change rate of the cell area $(1/a)(da/dt)$, cell division rate k_d and the negative cell extrusion rate k_e. Division and extrusion rates are defined in Eqs. (2.9)-(2.10).

We plot cellular contributions to the blade cumulative isotropic flow in Fig. 5.1 for a number of different experiments. Besides the unperturbed wild type wings, *dumpy* mutant wing and mechanically perturbed wild type wings that we studied in Chapter 3, here we study homozygous *cdc2* mutant wings in which the cell divisions have been inhibited when the temperature is increased to 30 degrees Celsius. As the increase in temperature and the *cdc2* mutation are two different perturbations, we also study wild type wings imaged at the increased temperature as well as heterozygous *cdc2* mutant wings at the increased temperature.

We find that the overall area does not change significantly (blue lines in Fig. 5.1). In all wings in which cell divisions are present, the decrease in the cell area (green lines in Fig. 5.1) occurs simultaneously with the cell divisions and it is of similar magnitude as cell division rate (orange lines in Fig. 5.1). Furthermore, the cell area does not change in the homozygous *cdc2* mutant wings where the divisions are inhibited. These two observations could be accounted for by a direct mechanical constraint that prevents the wing blade tissue from changing its area. If that was the case, the increase in cell number would drive the increase in pressure. However, during the pupal wing morphogenesis the wing blade shape changes significantly. It is hard to imagine an external mechanical area preserving constraint when the wing blade dimensions change
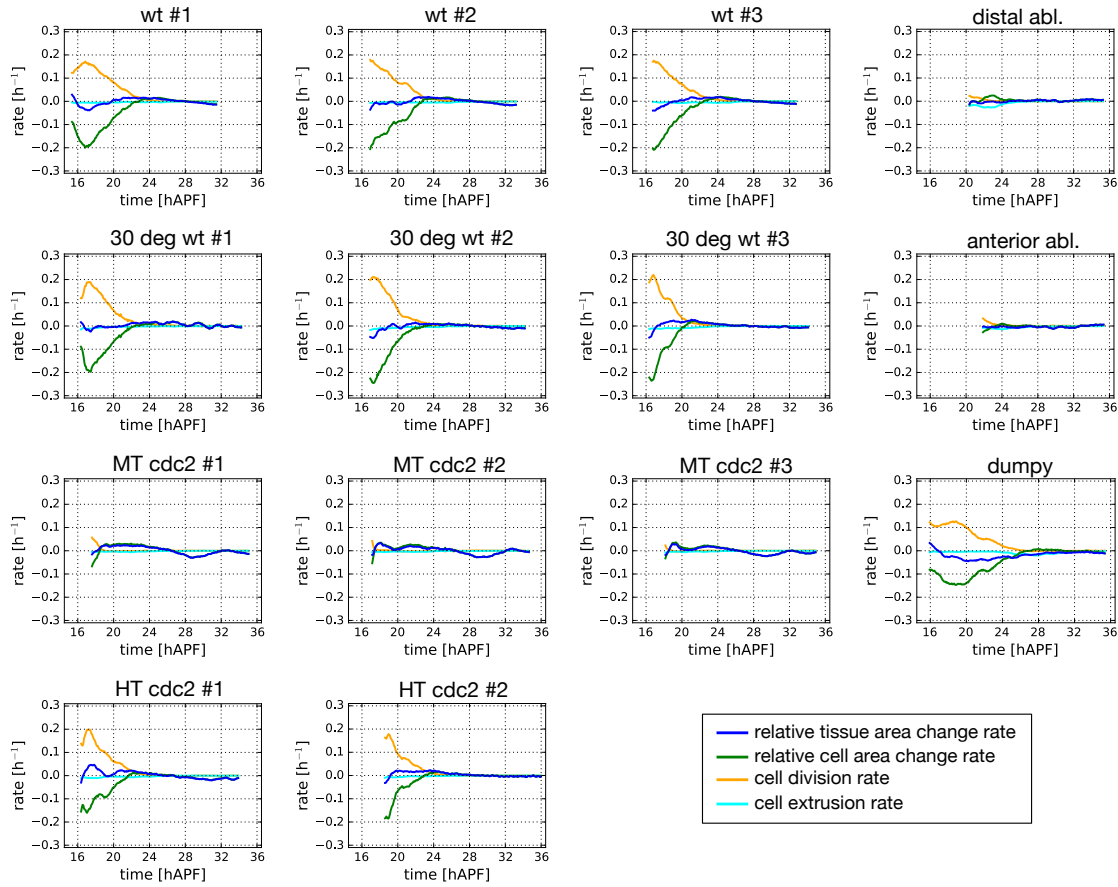
Figure 5.1: Relative area change rate of the blade tracked region (blue) in different experiments and its cellular contributions: relative area change rate (green), cell division rate (orange) and cell extrusion rate (cyan). We use 3 wild type wings (wt), 3 wild type wings imaged at 30 degrees Celsius (30 deg wt), 3 homozygous cdc2 mutant wings imaged at 30 degrees Celsius (MT cdc2), 2 heterozygous cdc2 mutant wings imaged at 30 degrees Celsius (HT cdc2), 1 distally ablated wing, 1 anteriorly ablated wing and 1 *dumpy* mutant wing. For more details about different experiments see Appendix B. For plotting, the data is smoothed by a moving time interval of about 50 minutes. Some of the data shown here was published in ref. [54].

along both long and short wing axis.

A simpler explanation is that, under the same pressure, the daughter cells are smaller in area than their mothers. In other words, the preferred cell area is reduced by cell division. Therefore, we expect that in the model for the preferred cell area Eq. (2.23), the parameter ϵ controlling the influence of cell divisions on the preferred cell area

change is much smaller than 1. This could indicate that during pupal morphogenesis the wing blade tissue does not have a reservoir of cellular material it could use to grow.

Here we do not attempt to model the cell division rate but we rather measure it directly from the experiment and use it as an input when modeling cell extrusions in the following section. However, we will find a value of ϵ by investigating the cell extrusions mechanosensitivity.

5.2 Model of mechanosensitive cell extrusions

Cell extrusion is a process of removing a single cell from the epithelium. Epithelia use cell extrusion to remove dying or *apoptotic* cells from the epithelium since dead cells in the epithelium could compromise its function [77]. Another type of cell extrusion is a process of removing a live cell from the epithelium to maintain homeostasis in the epithelium [78].

During the pupal wing morphogenesis, we identify extruding cells by observing the cellular network in time. This allows us to measure the cell extrusion rate. In wild type wings, the extrusions are present during the first 8-9 hours of pupal morphogenesis and their rate significantly decreases (blue curves in Fig. 5.2 A top row). In the experiments where the boundary conditions were compromised by laser ablation (blue curves in Fig. 5.2 A right) we observed a higher rate of cell extrusions, indicating that unlike division, extrusions could be sensitive to changes of mechanical forces in the tissue. To quantitatively describe the response of cell extrusions to the tissue stresses we construct a simple mechanosensitive model for the cell extrusion rate.

5.2.1 Constitutive equation for cell extrusions

The cell extrusion rate is a scalar quantity and we expect it to be a function of pressure

$$k_e = F(P) \quad . \tag{5.1}$$

The number of cell extrusions is always a positive number and therefore a simple linear function $F(P) \sim P$ cannot be a realistic model close to the value of pressure at

which the cell extrusion rate vanishes. Our model should be capable of describing both the regime of frequent cell extrusions as well as the regime in which cell extrusions do not appear. Therefore, we have to include a nonlinearity in our model that will ensure positive definiteness of the cell extrusion rate. We also expect that the rate of cell extrusion should increase monotonically with the pressure. A simple model that fulfills these requirements is an exponential response of cell extrusion rate to the tissue pressure

$$k_e = \mu e^{\frac{P}{\kappa_e}} \quad , \tag{5.2}$$

where κ_e has a unit of elastic constant and sets the scale on which the pressure fluctuations significantly change the extrusion rate and μ is the rate of cell extrusions in a pressure free tissue.

Motivated by the memory kernel in the constitutive equation for the shear rate due to topological rearrangements in Eq. (3.2), we include an exponential memory kernel in the cell extrusion model

$$\phi_e(t) = \frac{1}{\tau_e} e^{-\frac{t}{\tau_e}} \quad . \tag{5.3}$$

Here, τ_e is the memory time scale over which the information about the pressure in the tissue is retained. Therefore, we obtain

$$k_e(t) = \int_{-\infty}^{t} \phi_e(t - t')\mu \exp\left(\frac{P(t')}{\kappa_e}\right) dt' \quad . \tag{5.4}$$

This equation can be written as a differential equation

$$\left(1 + \tau_e \partial_t\right) k_e = \mu e^{\frac{P}{\kappa_e}} \quad . \tag{5.5}$$

Our collaborators cannot directly measure the pressure in the wing blade. Therefore, in order to experimentally validate Eq. (5.5), we need to propose a constitutive equation for pressure. To this end, we use the constitutive relation Eq. (2.21) without

memory

$$P = -\overline{K} \ln \left(\frac{a}{a_0} \right) \quad . \tag{5.6}$$

This choice is made in analogy with the shear stress constitutive equation Eq. (3.6). It can be understood as an assumption that cells adjust their size on a time-scale short compared to the time-scale over which the tissue can relax stress fluctuations.

In the dynamical equation for the preferred cell area Eq. (2.23) we omit the growth term by setting $\beta(a_0) = 0$. This is justified by the observation from the previous section where we found that the cell area typically does not change significantly in the absence of cell divisions. The observed slight variations can arise from changes in pressure. Therefore, we use the equation for the dynamics of cell preferred area

$$\partial_t a_0 = - \left(1 - \epsilon \right) k_d a_0 \quad . \tag{5.7}$$

Now, we eliminate the preferred cell area a_0 from Eq. (5.6) by subtracting the initial value of the pressure

$$P(t) - P(t_0) = -\overline{K} \left[\ln \left(\frac{a(t)}{a(t_0)} \right) - \ln \left(\frac{a_0(t)}{a_0(t_0)} \right) \right] \tag{5.8}$$

$$= -\overline{K} \left[(1 - \epsilon) \int_{t_0}^{t} k_d(t')dt' + \ln \left(\frac{a(t)}{a(t_0)} \right) \right] \quad . \tag{5.9}$$

We can now write the dynamical equation for the cell extrusion rate

$$\left(1 + \tau_e \partial_t \right) k_e(t, t_0) = \mu e^{\frac{P(t_0)}{\kappa_e}} \exp \left(-\frac{\overline{K}}{\kappa_e} \left[(1 - \epsilon) \int_{t_0}^{t} k_d(t')dt' + \ln \left(\frac{a(t)}{a(t_0)} \right) \right] \right) \quad , \tag{5.10}$$

where we can measure both the cell division rate k_d and the cell area a. Our lack of knowledge about pressure and preferred cell area a_0 is represented by the initial value of the pressure $P(t_0)$.

5.2.2 Comparison with the experimental data

Now we determine parameters τ_e, ϵ and $\kappa_e/\overline{K}$ by jointly fitting the Eq. (5.10) to the experimental data. We find that a single set of parameters

$$\tau_e = 2.9 \text{ hours} \quad , \tag{5.11}$$

$$\epsilon = 0.22 \quad , \tag{5.12}$$

$$\frac{\kappa_e}{\overline{K}} = 1.7 \cdot 10^{-2} \tag{5.13}$$

can account for the observed cumulative extrusion rates in all experiments except for the *dumpy* mutant wing (see Fig. 5.2 A). The product $\mu \exp\left(P(t_0)/\kappa_e\right)$ was allowed to vary in different experiments because the initial value of the pressure can vary in experiments. Also, the initial value of extrusion rate k_e was treated as a fitting parameter for each experiment. In the *dumpy* mutant wing blade, the mechanosensitive model in Eq. (5.10) fails to account for the measured extrusion rate for any values of parameters τ_e, ϵ and $\kappa_e/\overline{K}$ (see Fig. 5.2 B).

The value of the memory time-scale τ_e is comparable to the value of the memory time-scale found in the analysis of the response of topological rearrangements to cell elongation in Section 3.1. The small value of the parameter ϵ is consistent with the observation that cell divisions reduce the preferred cell area of the daughter cells. The positive value $\epsilon = 0.22$ indicates that the preferred cell area of daughter cells is slightly larger than the one-half of their mother preferred cell area. Finally, the dimensionless ratio $\kappa_e/\overline{K}$ sets the range over which changes in natural cell strain $u = \ln\left(a/a_0\right)$ significantly change the cell extrusion rate. The value $\kappa_e/\overline{K} = 1.7 \cdot 10^{-2}$ indicates that the cell area strain of only several percent is sufficient to significantly change the cell extrusion rate.

Interestingly, extrusions in the *dumpy* mutant wing cannot be accounted for by this model. As this model accounts only for the mechanically induced cell extrusions it is possible that in this mutant, the additional cell extrusions arise due to chemical signaling.
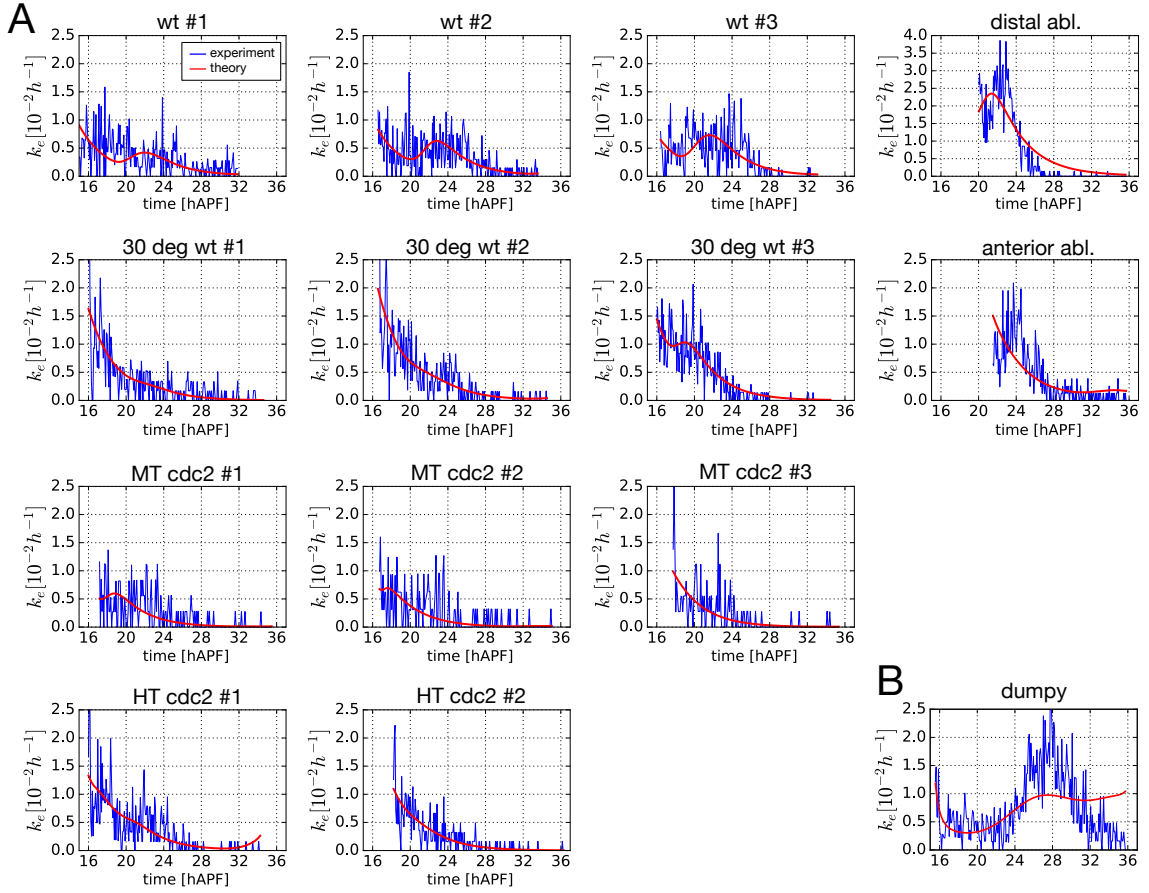
Figure 5.2: A) Cell extrusion rate k_e in different experiments (blue) and mechanosensitive model for the cell extrusion rate fitted to the experimental data (red) with a single set of parameters τ_e, ϵ and $\kappa_e/\overline{K}$. Initial conditions are treated as fitting parameters and the product $\mu \exp\left(P(t_0)/\kappa_e\right)$ was allowed to vary in different experiments. B) This mechanosensitive model can not account for the extrusions in the dumpy mutant wing for any values of model parameters.

5.3 Summary

In this chapter, we analyzed area changes of the fly wing blade and we discussed how cell divisions affect mechanical properties of the cells in the wing. Although the number of cells increases significantly, we found that the overall wing blade area does not increase. This indicated that cell divisions reduce the cell size.

We then proposed a mechanosensitive model to describe the cell extrusions in the wing blade in which the extrusion rate grows exponentially with the pressure in the

tissue. Additionally, we introduced a memory kernel in the response of cell extrusion to pressure. To experimentally validate this model we analyzed a number of different wing perturbations, including mechanical perturbations, temperature changes and inhibition of cell divisions. We found that the experimentally measured cell extrusion rates can be reasonably described by the proposed model with a single set of parameters. The small value of the cell division parameter $\epsilon = 0.22$ is consistent with the observation that cell divisions reduce the cell size.

Chapter 6

Boundary conditions shape the wing during pupal morphogenesis

In this chapter, we investigate the role of boundary conditions in shaping the fly wing during the pupal morphogenesis. Our aim is to build a simple model of the wing that combines the tissue material properties with external forces acting at the tissue boundary. This model will allow us to describe both tissue and cell shape changes under different boundary conditions and compare them to the corresponding experimental results.

We first describe the rectangle model of the wing in which the wing is composed of two rectangular homogeneous pieces of tissue representing the hinge and blade regions. We then introduce the external forces acting on the wing tissue. They include the elastic linkers connecting the wing margin to the surrounding hard cuticle and friction between the tissue and the surroundings. We use this model to describe one unperturbed wild type wing and two wild type wings in which the boundary conditions have been altered by laser ablation to determine the unknown parameters describing the tissue material properties, boundary conditions and the friction. Finally, we find that the *dumpy* mutant wing pupal morphogenesis can be described as the morphogenesis of the wild type wing tissue with perturbed boundary conditions.

Results of this chapter have been published in ref. [54].

6.1 Rectangle model for the developing wing epithelium

Here, we construct a simple model of the wing where the wing blade and hinge regions are represented by two homogeneous rectangular pieces of tissue in contact (see Fig. 6.1). They are connected to the surrounding hard cuticle via elastic linkers that provide elastic resistance to the shape changes of the hinge and blade regions. Since the distal end of the wing does not move significantly in the unperturbed wild type wings, we will assume that distal lateral linkers are sufficiently stiff so that we can treat the distal end of the blade rectangle as immobile in the wild type and anteriorly ablated wings (see Fig. 6.2). We will treat the proximal end of the hinge rectangle in the same way. Therefore, in the wild type and anteriorly ablated wings we assume that the overall wing length does not change. This is a good approximation, as the total wing length in the data varies up to 2%.

6.1.1 Rectangle shape and tissue flow

Dimensions of a rectangle shaped, homogeneously flowing tissue, are related to the velocity gradient in the tissue as

$$\frac{1}{L^{\text{region}}}\frac{dL^{\text{region}}}{dt} = \frac{1}{2}v_{kk}^{\text{region}} + \tilde{v}_{xx}^{\text{region}} \quad , \tag{6.1}$$

$$\frac{1}{h^{\text{region}}}\frac{dh^{\text{region}}}{dt} = \frac{1}{2}v_{kk}^{\text{region}} - \tilde{v}_{xx}^{\text{region}} \quad . \tag{6.2}$$

Here, L^{region} and h^{region} are the length and height of the particular rectangle region and v_{kk} and $\tilde{v}_{xx}$ are the corresponding isotropic flow rate and shear flow rate along the x axis, aligned with the long axis of the wing. The superscript 'region' represents either hinge or blade. We will denote variables related to the blade without superscript, for example, L denotes the length of the blade region. Variables related to the hinge will have a superscript H, for example, L^H denotes the length of the hinge region.

In this chapter our aim is to study the shape of the hinge and blade tissue. Therefore, we do not consider the tracked regions defined in Section 3.1. Instead, we consider the whole visible hinge and blade regions of the wing (colored wing regions in Fig. 6.4).
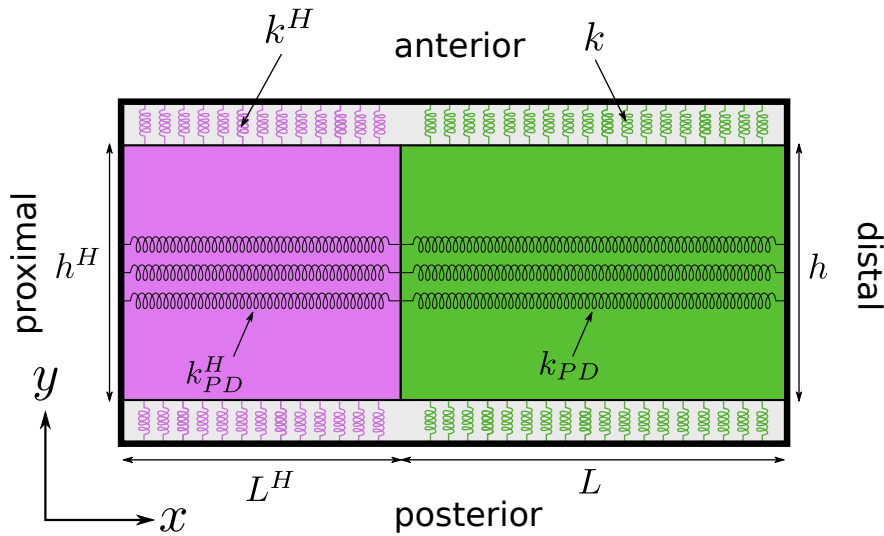
Figure 6.1: Schematic of the hinge (magenta) and blade (green) in the rectangle model. Height and length of blade and hinge regions are denoted by h, L, h^H and L^H. Elastic constants of lateral linkers are denoted by k^H and k_{PD}^H in the hinge and k and k_{PD} in the blade.

Blade and hinge regions in the experimental data are not rectangular. There are different ways to characterize height and length of an arbitrary region. In Appendix F we define the dimensions of the hinge and blade regions that make Eqs. (6.1)-(6.2) exactly satisfied and account for inflow and outflow of tissue in the field of view during the experiment.

6.2 Boundary conditions, friction and force balance

Lateral connections of the tissue to the surrounding cuticle are important for the proper development of the wing. This is shown in experiments performed by our collaborators where the material surrounding the wing was ablated by laser, in one case distally and in the other case anteriorly. In both cases, the wing shape is defective by the end of the pupal morphogenesis. Experiments are described in more detail in Appendix B. We include the lateral connections of the tissue to the surrounding hard cuticle as elastic linkers that oppose the change of blade and hinge heights and lengths

(see Fig. 6.1).

Elastic properties of the material represented by the lateral linkers do not have to be isotropic and the effective elasticity in different directions can come from different sources. Therefore, we allow them to act in the x and y direction in different ways. Also, since the linkers are likely to be distributed non-uniformly around the wing tissue we allow the hinge and blade linkers to have different elastic constants.

The tissue stress component σ_{yy} at the anterior and posterior tissue boundaries is determined by the antero-posterior (AP) elastic linkers

$$\sigma_{yy}^{\text{region}} = -k^{\text{region}} \left(h^{\text{region}} - h_0^{\text{region}} \right) \quad , \tag{6.3}$$

where h_0^{region} is the height of a region at which the elastic boundary linkers are in their resting configuration. We take h and h^H to be equal to the initial values of the region height. Elastic constants of the AP elastic linkers are k and k^H.

Since we assume that the tissue is flowing homogeneously, the boundary condition sets the value of the stress in the whole tissue. In notation we will not distinguish boundary and bulk values of stress.

To account for the dissipative processes in the wing we introduce an effective friction. Introducing a bulk friction force would lead to a contradiction with the assumption of homogeneous stress in the tissue. Therefore, we impose a frictional force $\gamma dL^H/dt$ acting on the interface of the hinge and blade rectangle regions. In the distally ablated and *dumpy* mutant wings the distal end of the blade region is mobile so we also include the frictional force $\gamma d(L + L^H)/dt$ acting at that edge.

Balance of forces at the hinge-blade interface states that the difference in forces from the tissue stresses is balanced by friction and elastic forces of proximal-distal (PD) linkers

$$h\sigma_{xx} - h^{\text{H}}\sigma_{xx}^{\text{H}} = \gamma \frac{dL^H}{dt} - k_{PD} \left(L - L_0 \right) \\ + k_{PD}^{\text{H}} \left(L^{\text{H}} - L_0^{\text{H}} \right) \quad . \tag{6.4}$$

Here, γ is the friction coefficient. As in the case of the region height, L_0^{region} are the resting values of the region length and we take them to correspond to the initial

values of the region lengths. PD elastic linkers have elastic constants k_{PD} and k_{PD}^H. We assumed that PD elastic linkers produce the same force in response to the change of region length, irrespective of the region height. Therefore, k_{PD} and k_{PD}^H do not have the same units as k and k^H.

6.2.1 Boundary conditions in the mechanically perturbed wings

To investigate how modifications of the boundary conditions influence the pupal morphogenesis of the wing, our collaborators performed experiments in which the lateral linkers connecting the wing tissue to the surrounding cuticle were ablated by a laser. In these experiments, the tissue was not directly damaged and therefore we can assume that the tissue mechanical properties were not altered by the ablation procedure. This would not be the case if the tissue was directly damaged as the damage could initiate a wound healing response in the tissue [79–83].

In the two laser ablation experiments the lateral linkers were ablated either on the distal or on the anterior side of the wing (see Fig. 6.2). To describe these perturbations in the rectangle model we remove the corresponding lateral elastic linkers. Therefore, for the anterior ablation instead of Eq. (6.3) we write

$$\sigma_{yy} = 0 \quad . \tag{6.5}$$

In the experiment where the distal boundary linkers were ablated the distal end of the tissue can move and we write force balance as

$$-h\sigma_{xx} = \gamma \frac{d\left(L + L^{\mathrm{H}}\right)}{dt} - k_{PD}\left(L - L_0\right) \quad . \tag{6.6}$$

Here we used the same friction coefficient as in Eq. (6.4).

6.3 Model for the tissue area change

We were not able to reliably extract information from the isotropic retraction flow in the circular ablation experiments described in Section 3.2. Here we conside the following form for the constitutive equation for the two-dimensional pressure in the

wild type

distal ablation

anterior ablation

dumpy
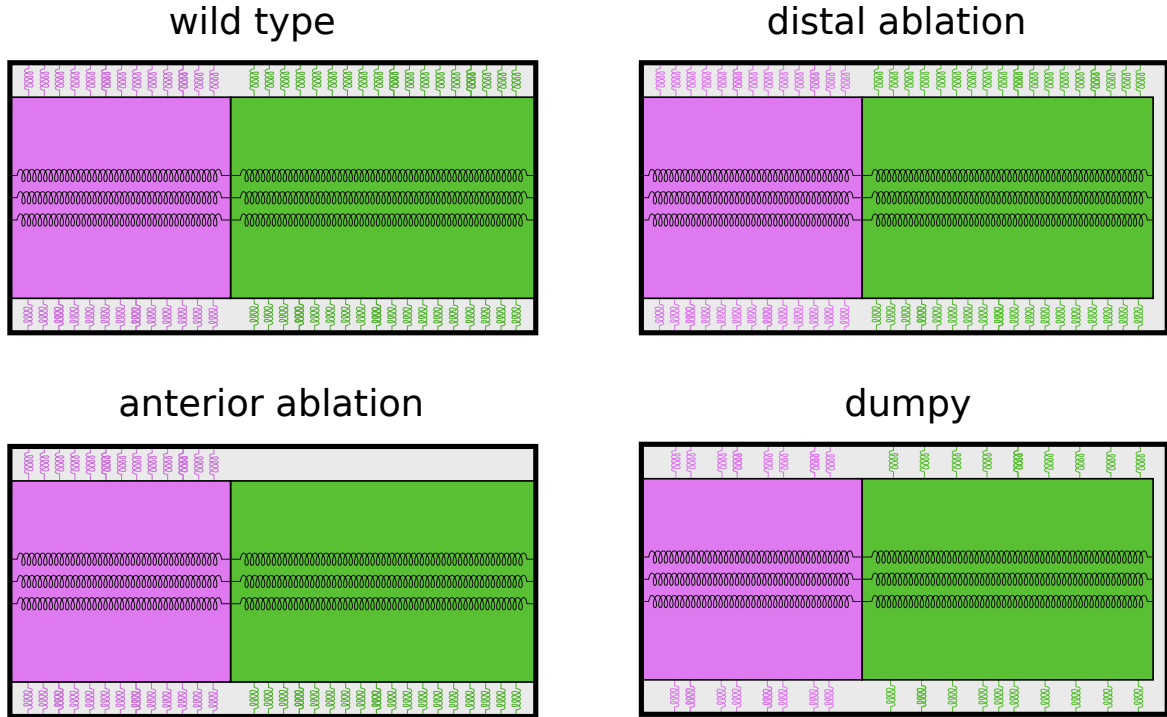
Figure 6.2: Schematic of boundary conditions in different experiments. In wild type and anteriorly ablated wing distal linkers are very strong and are modeled as a fixed wall. In the distally ablated wing distal linkers are removed. In the anteriorly ablated wing anterior linkers are removed. In the dumpy mutant wing distal linkers are removed and all other linker strengts are allowed to vary from wild type values.

tissue

$$P = -\overline{K}u - \overline{\eta}\frac{du}{dt} \quad , \tag{6.7}$$

where

$$u = \ln\frac{a}{a_0} \tag{6.8}$$

is the natural strain of the average cell area. We introduced the bulk viscosity $\overline{\eta}$ because it significantly improved the agreement of the model with the experimental data.

To describe the dynamics of the preferred cell area we assume that divisions are

exactly halving the preferred cell area of the mother cells so that

$$\frac{da_0}{dt} = -k_d a_0 \quad , \tag{6.9}$$

with the initial condition

$$a_0(t_0) = a(t_0)e^{-\overline{\zeta}/K} \quad . \tag{6.10}$$

Here we introduced cell area contractility $\overline{\zeta}$. This model is applied to the blade region only. The contraction of the hinge region driving the pupal morphogenesis cannot be captured with a constant $\overline{\zeta}$. Instead, we impose the hinge area as measured in the experiments and use the pressure P^H in the hinge to maintain the measured dynamics of the hinge area $A^H(t)$.

Finally, the extrusions in the *dumpy* mutant wing do not follow the mechanosensitive model described in Chapter 5 and therefore we treat the cell extrusion rate as a direct input from the experiments.

6.4 Comparison with the experimental data

In this section, we fit the rectangle model to the experimental data to ask whether we can describe the wild type and mechanically perturbed wings with the same model and to find out how is the *dumpy* mutant wing different from the wild type one.

In Section 3.1 we determined time scales τ and τ_d relevant for dynamics of shear due to topological rearrangements in the Eq. (3.3) in the tracked blade region of the wing. At the same time, we determined the magnitudes of active shear flow λ for each of the wings considered. In order to use the Eq. (3.3) in the rectangle model, we repeated the fitting procedure using the shear due to topological rearrangements R_{xx} corresponding to the tissue shear rate determined by the particle image velocimetry (PIV) measurements of tissue velocity in the whole visible hinge and blade regions

$$R_{xx}^{\text{region}} = \tilde{v}_{PIV,xx}^{\text{region}} - \frac{dQ_{xx}^{\text{region}}}{dt} \quad . \tag{6.11}$$

Although the cell elongation can in principle be measured in the whole wing, due to

a lower quality of the experimental data at the wing margin and parts of the hinge region, we measure the cell elongation in the tracked regions, as defined in Section 3.1.1 (also see Fig. 3.1). The PIV measurements were performed by our collaborators and are described in ref. [54].

Besides the time scales τ and τ_d, and the active shear flow λ in the hinge and blade regions these fits also provide initial conditions for R_{xx} that we will use in the rectangle model. The values of parameters are reported in Table 6.4.

		wt 1	wt 2	wt 3	ant. abl.	dist. abl.	dumpy
Blade	$\tau[h]$	1.7 ± 0.1					
	$\tau_d[h]$	4.2 ± 0.3					
	$\lambda[h^{-1}]$	-0.11 ± 0.01	-0.11 ± 0.01	-0.10 ± 0.01	-0.10 ± 0.01	-0.068 ± 0.007	-0.094 ± 0.008
Hinge	$\tau[h]$	5 ± 2					
	$\tau_d[h]$	2 ± 1					
	$\lambda[h^{-1}]$	-0.05 ± 0.01	-0.05 ± 0.01	-0.04 ± 0.01	-0.03 ± 0.01	-0.01 ± 0.01	-0.04 ± 0.01

Table 6.1: Parameter values obtained by fitting Eq. (3.3) to the experimental data in whole visible blade and hinge regions of the wing, using the shear due to topological rearrangements R_{xx} quantified using Eq. (6.11). Uncertainties reported here are standard deviations of parameters obtained on 1000 realizations obtained by bootstraping the original datasets. Source: adapted from ref. [54].

In Section 3.2 we used the circular laser ablation experiments to determine the ratio of active shear stress and shear elastic constant $\zeta/K = 0.3 \pm 0.2$ in wild type and *dumpy* mutant wings. Here, in rectangle model we use the constitutive equation for shear stress Eq. (3.6) and the measured value of ζ/K in the wing blade.

Now we determine the remaining 11 wild type parameters. They can be divided into parameters describing mechanical properties of the epithelial tissue (Table 6.4 top) and parameters describing the interaction of the wing tissue the external material (Table 6.4 bottom).

Since we never measure the absolute value of any stress, we normalize all other quantities with the blade shear elastic constant K. This leaves us with 10 unknown parameters. We determine these 10 parameters by numerically solving the rectangle model and fitting the solutions to the experimental data.

The rectangle model presented in this chapter provides the following dynamical

system

$$\frac{dQ_{xx}}{dt} = \frac{1}{2}\left(v_{xx} - v_{yy}\right) - R_{xx} \quad , \tag{6.12}$$

$$\frac{dQ_{xx}^{\mathrm{H}}}{dt} = \frac{1}{2}\left(v_{xx}^{\mathrm{H}} - v_{yy}^{\mathrm{H}}\right) - R_{xx}^{\mathrm{H}} \quad , \tag{6.13}$$

$$\frac{dR_{xx}}{dt} = -\frac{1}{\tau_d}R_{xx} + \frac{1}{\tau\tau_d}Q_{xx} + \frac{1}{\tau_d}\lambda \quad , \tag{6.14}$$

$$\frac{dR_{xx}^{\mathrm{H}}}{dt} = -\frac{1}{\tau_d}R_{xx}^{\mathrm{H}} + \frac{1}{\tau\tau_d}Q_{xx}^{\mathrm{H}} + \frac{1}{\tau_d}\lambda^{\mathrm{H}} \quad , \tag{6.15}$$

$$\gamma\frac{dL^{\mathrm{H}}}{dt} = -h^{\mathrm{H}}\sigma_{xx}^{\mathrm{H}} + h\sigma_{xx}$$
$$- k_{PD}^{\mathrm{H}}\left(L^{\mathrm{H}} - L_0^{\mathrm{H}}\right) + k_{PD}\left(L - L_0\right) \quad , \tag{6.16}$$

$$\frac{dh}{dt} = hv_{yy} \quad , \tag{6.17}$$

together with Eq. (6.6) used in experiments with perturbed distal linkers.

The tissue velocity gradient, tissue dimensions and tissue stress can be calculated using

$$v_{xx}^{\mathrm{H}} = \frac{1}{L^{\mathrm{H}}}\frac{dL^{\mathrm{H}}}{dt} \quad , \tag{6.18}$$

$$v_{xx} = \frac{1}{L}\frac{dL}{dt} \quad , \tag{6.19}$$

$$v_{xx}^{\mathrm{H}} + v_{yy}^{\mathrm{H}} = \frac{1}{A^{\mathrm{H}}}\frac{dA^{\mathrm{H}}}{dt} \quad , \tag{6.20}$$

$$\sigma_{xx} = 2KQ_{xx} + \zeta + \overline{\zeta} + \overline{K}\left(\ln\frac{A}{A(t_0)} + \int_{t_0}^{t}k_e dt\right)$$
$$+ \overline{\eta}\left(v_{xx} + v_{yy} + k_e\right) \quad , \tag{6.21}$$

$$\sigma_{yy} = -2KQ_{xx} - \zeta + \overline{\zeta} + \overline{K}\left(\ln\frac{A}{A(t_0)} + \int_{t_0}^{t}k_e dt\right) \quad ,$$
$$+ \overline{\eta}\left(v_{xx} + v_{yy} + k_e\right) \quad , \tag{6.22}$$

$$\sigma_{yy} = -k\left(h - h_0\right) \quad , \tag{6.23}$$

$$\sigma_{xx}^{\mathrm{H}} = 2K^{\mathrm{H}}Q_{xx}^{\mathrm{H}} + \zeta^{\mathrm{H}} - P^{\mathrm{H}} \quad , \tag{6.24}$$

$$\sigma_{yy}^{\mathrm{H}} = -2K^{\mathrm{H}}Q_{xx}^{\mathrm{H}} - \zeta^{\mathrm{H}} - P^{\mathrm{H}} \quad , \tag{6.25}$$

$$\sigma_{yy}^{\mathrm{H}} = -k^{\mathrm{H}} \left(h^{\mathrm{H}} - h_0^{\mathrm{H}} \right) \quad . \tag{6.26}$$

As in Section 3.1.2 we have set $q_{xx} = 1$. This set of equations can be numerically solved to determine the dynamics of the hinge and blade region shape and size for a given set of parameters and boundary conditions.

Now we need to jointly fit this model to the experimentally measured changes of dimensions of the hinge and blade regions for wild type and the two mechanically perturbed wild type wings to determine the remaining unknown parameters.

In order to jointly fit the data of the wild type wing and the two mechanically perturbed wild type wings, we assume that the mechanically perturbed wings behave as wild type wings before the ablation. Relative starting time points of experiments with the mechanically perturbed wings with respect to the wild type wing were determined by our collaborators, based on biological landmarks. This allows us to use the tissue area change decomposition Eq. (2.13) and Eq. (6.8) to express the difference of the accumulated cell extrusion rate in the wild type and ablated wings as

$$\int_{t_{0,WT}}^{t_{0,\mathrm{abl.}}} \left(k_e^{\mathrm{abl.}}(t') - k_e^{WT}(t') \right) dt' = u^{\mathrm{abl.}}(t_{0,\mathrm{abl.}}) - u^{WT}(t_{0,\mathrm{abl.}}) - \ln \frac{A^{\mathrm{abl.}}(t_{0,\mathrm{abl.}})}{A^{WT}(t_{0,\mathrm{abl.}})} \quad . \tag{6.27}$$

Here, the *abl.* stands for either of the two ablated wings and $t_{0,\mathrm{abl.}}$ is the starting time point of the corresponding experiment. Starting time point of the wild type wing is denoted by $t_{0,WT}$. The estimate in Eq. (6.27) can be incorporated in the rectangle model by simply redefining the parameter $\overline{\zeta}$ as follows

$$\overline{\zeta}^{\mathrm{abl.}} = \overline{\zeta} + \overline{K} \left[\int_{t_{0,WT}}^{t_{0,\,\mathrm{abl.}}} k_e^{WT}(t') dt' + \ln \frac{A^{\mathrm{abl.}}(t_{0,\,\mathrm{abl.}})}{A^{WT}(t_{0,WT})} \right] \quad . \tag{6.28}$$

Without this relation, we would be forced to use an independent $\overline{\zeta}$ in each of the wings.

We now perform a joint fit of the rectangle model to the accumulated cell elongation change $Q_{xx}(t) - Q_{xx}(t_0)$, accumulated shear $\int_{t_0}^{t} \tilde{v}_{xx} dt$ and accumulated relative area change $\ln(A(t)/A(t_0))$ in the hinge and blade regions in the wild type and two
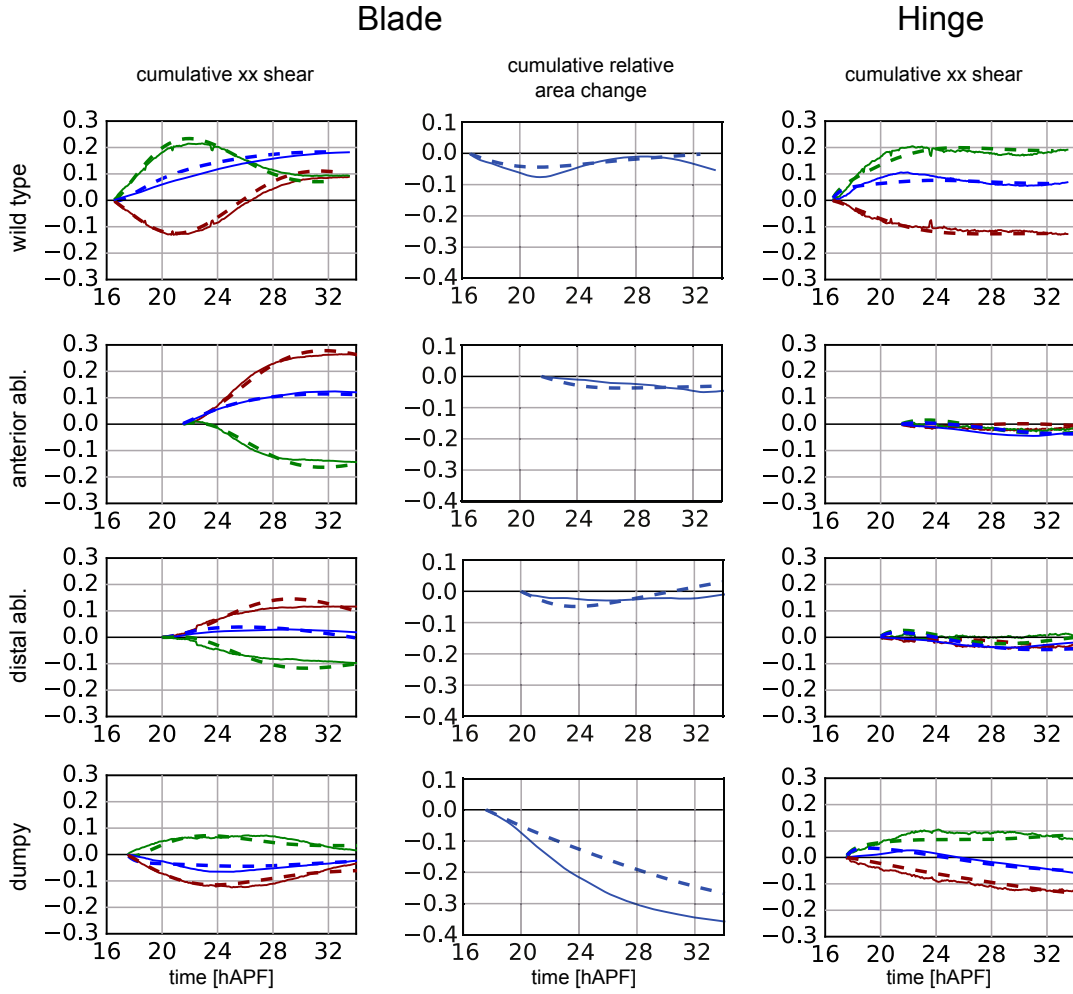
Figure 6.3: Comparison of data (dotted lines) and theoretical curves (full lines) obtained by fitting the accumulated cell elongation change (green lines), accumulated shear (blue lines) and accumulated relative area change (blue lines). Dark red lines show the accumulated shear due to topological rearrangements. Source: partially adapted from ref. [54].

mechanically perturbed wild type movies. We find that the two parameters characterizing the anisotropic stress in the hinge region K^H and ζ^H are small and have little influence on the fit quality. Thus we set the two parameters to 0. This corresponds to effectively neglecting anisotropic stress in the hinge and reduces the number of fitting parameters to 8. Repeating the fitting procedure with the reduced number of parameters we find that a single set of parameters can reasonably describe wild type,

distally and anteriorly ablated wings (see Fig. 6.3 and Fig. 6.4). Therefore, we can use the rectangle model with the same parameters to describe both the wild type and mechanically perturbed wings.

We report the obtained values of parameters in Table 6.4. The friction coefficient and the blade isotropic viscosity normalized by the blade shear elastic constant K have units of time and both are larger than the duration of experiments. Therefore, the dissipation processes have an important role in the tissue dynamics during pupal morphogenesis.

				wt	dist. abl.	ant. abl.	dumpy
Tissue paramteres	Blade	shear elastic constant	K/K		1		
		cell area contractiliy	$\overline{\zeta}/K$		0.05 ± 0.03		
		isotropic elastic constant	$\overline{K}/K$		2.07 ± 0.09		
		isotropic viscosity	$\overline{\eta}/K[h]$		49 ± 2		
	Hinge	active shear stress	ζ^{H}/K		0		
		shear elastic constant	K^{H}/K		0		
External linkers	Blade	AP linkers elasticitiy	kL_0/K		0.5 ± 0.1	0	0.005 ± 0.007
		PD linkers elasticity	k_{PD}/K		4.91 ± 0.04		5.3 ± 0.2
		friction coefficient	$\gamma/K[h]$		21.3 ± 0.8		22.1 ± 0.6
		distal linkers	-	Yes	No	Yes	No
	Hinge	AP linkers elasticity	$k^{\mathrm{H}}L_0/K$		67.8 ± 0.4		78 ± 2
		PD linkers elasticity	k^{H}_{PD}/K		9.50 ± 0.07		16.8 ± 0.6
		friction coefficient	$\gamma/K[h]$		21.3 ± 0.8		22.1 ± 0.6

Table 6.2: Parameters obtained by fitting the rectangle model to the data. Shear elastic constant K in the blade is used as a unit of stress. Active shear stress ζ^H and shear elastic constant K^H in the hinge are negligible so we set their values to 0. The uncertainties reported here are calculated from the diagonal values of the inverse Hessian matrix at the minimum of the function used in the fitting procedure and they do not represent other sources of uncertainty. The friction coefficient γ is listed twice, both as blade and hinge parameter. Source: partially adapted from ref. [54].

6.5 Dumpy mutant wing develops as the wild type tissue with compromised boundary linkers

We now turn to the *dumpy* mutant wing. To qualitatively describe the *dumpy* mutant wing morphogenesis we use the rectangle model described in the previous subsection. As we expect that the main role of the Dumpy protein is in constructing

the connections between the tissue and the surrounding cuticle [84], we want to account for the experimental measurement of tissue and cell shape as well as the flow due to cellular rearrangements using the same tissue parameters we found for the wild type wings (see Table 6.4). At the same time, we allow the parameters describing the external links and the friction to change. We remove the distal connections as in the experiment with distally ablated lateral connections and thus we use the force balance Eq. (6.6) in the *dumpy* mutant model.
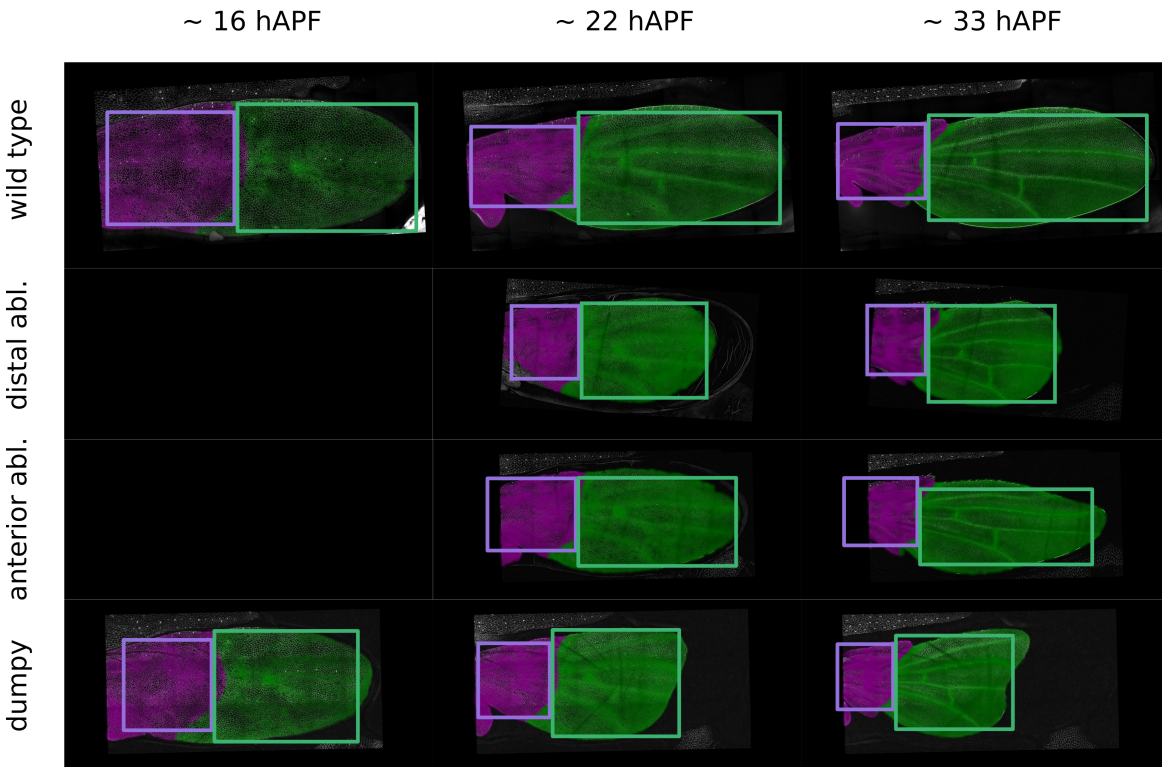
Figure 6.4: Wing hinge (magenta) and blade (green) regions overlayed with corresponding rectangles in the rectangle model. Apparent mismatch in region size in some images is due to inflow and/or outflow of tissue from the field of view, see Appendix F for details.

We find that the rectangle model with wild type tissue parameters can reasonably describe the morphogenesis of the *dumpy* mutant wing (see Fig. 6.3 and Fig. 6.4). Interestingly, we find that the friction coefficient and the PD elastic constant in the blade are not significantly affected (see Table 6.4). This indicates that the source of the friction and the elastic response of lateral linkers along the long axis of the wing

are not significantly affected in this *dumpy* mutant wing. However, the AP elastic constant is reduced by two orders of magnitude, indicating that the lateral linkers on anterior and/or posterior sides of the wing have been severely compromised.

6.6 Summary

In this chapter, we investigated fruit fly wing shape and size changes during pupal morphogenesis and found that the boundary conditions play an important role in the proper shaping of the fly wing.

We developed a rectangle model of the fruit fly wing. In this model blade and hinge regions of the wing are represented by homogeneous rectangle shaped tissues. We then introduced a model for boundary conditions where we described the linkers connecting tissue with the surrounding cuticle as elastic springs. We also introduced friction and area viscosity to account for dissipation processes in the wing tissue and between the wing and the surrounding extracellular matrix.

We then used this model together with the results from the Chapter 3 to determine the model parameters by fitting the theoretical result to experimental data of wild type and mechanically perturbed wild type wings. Finally, we found that we can understand mechanics of the dumpy mutant wing as a wild type wing with perturbed distal and antero-posterior boundary linkers.

Chapter 7

Active T1 transitions in a radially symmetric epithelium

In Chapter 3 we described active T1 transitions during which cells exchange neighbors due to some internal anisotropy not related to the cell shape. Similar active T1 transitions are known to drive germ band extension [85, 86] and elongation of embryo along the body axis [87, 88]. In a chick embryo they drive two-dimensional flows of ectoderm cells that precedes the formation of the primitive streak of the embryo [89].

In the first part of this chapter, we analyze the tissue flow and patterns of cell shape and size in the pouch region of an explanted fruit fly wing disc. We find evidence of active T1 transitions oriented radially around a center of the wing pouch. How do such active T1 transitions affect stresses in a planar epithelium?

We use the hydrodynamic theory described in Chapter 2 to investigate the influence of radially oriented active T1 transitions on a radially symmetric, rotationally invariant epithelium. We determine how such active T1 transitions can account for the observed distribution of cell elongation and we calculate their influence on the distribution of stresses in the epithelium. We find that the distribution of pressure predicted by the theory is consistent with the observed cell size and shape distributions.

Finally, we investigate how the radial T1 transitions can influence tissue growth. Mechanosensitive tissue growth has been studied in cell aggregates [42, 75] and in tissues in which cells proliferate at different proliferation rates [16, 74]. Also, the influence of mechanical compression on growth regulatory network has been investigated [38]. We find that for small variations of pressure in the epithelium the radially oriented active T1 transitions do not influence the tissue growth. However, as soon as

the spatial variations of pressure created by the radially oriented active T1 transitions are sufficiently large they can determine the tissue size. This provides a possible role for the active T1 transitions in the developing wing imaginal disc.

7.1 Radial patterns in the wing disc pouch epithelium
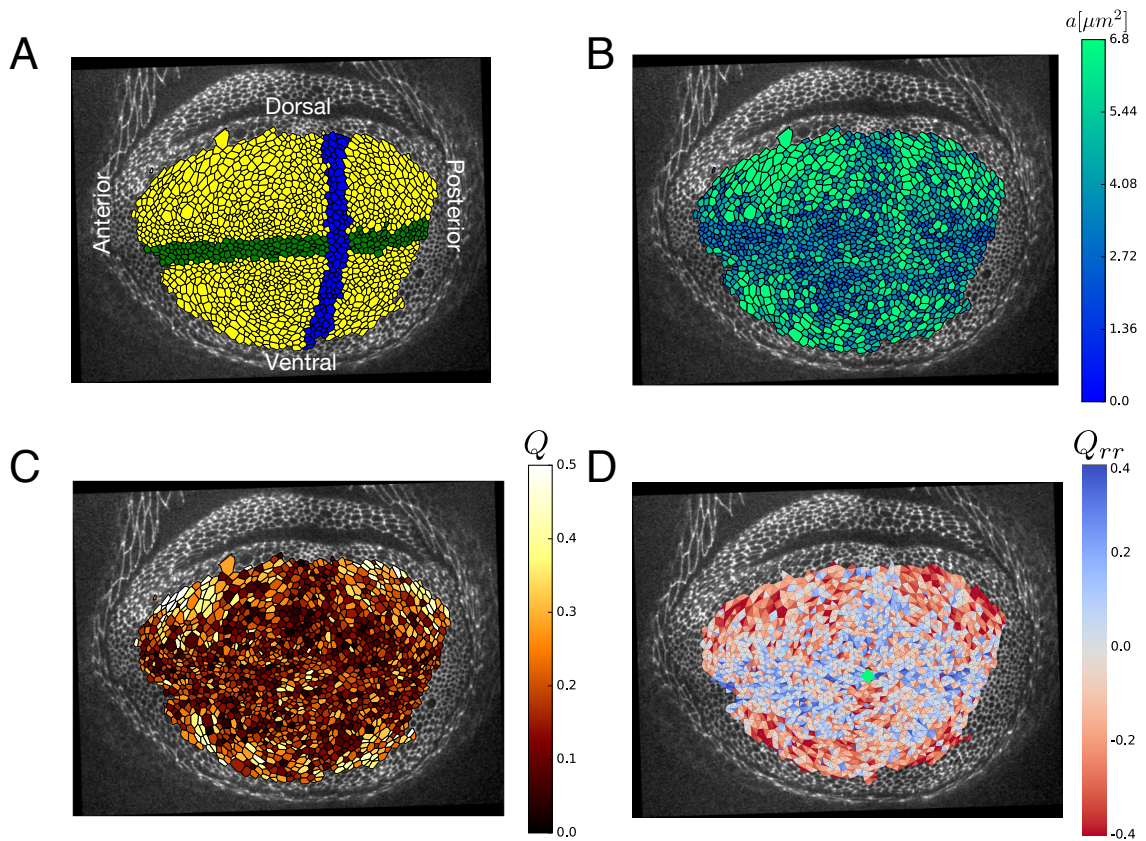
Figure 7.1: A) Wing disc pouch region. Dorso-ventral (DV) compartments boundary is colored in green and anterio-posterior (AP) compartments boundary is colored in blue. B) Cell area in the wing disc pouch. C) The magnitude of cell elongation in the wing disc pouch. D) The radial component of the cell elongation in the wing disc pouch. The center of the pouch is indicated by the green diamond.

We investigate the behavior of the pouch region of the wing imaginal disc (Fig. 7.1 A). The wing disc pouch is divided into dorsal and ventral compartments by the dorso-ventral (DV) compartment boundary (green cells in the Fig. 7.1 A) and anterior and

posterior compartments by the antero-posterior (AP) compartment boundary (blue cells in the Fig. 7.1 A). The cell area of individual cells at the end of the experiment is shown in Fig. 7.1 B. Cells in the in the middle of the pouch region are smaller than the cells the periphery of the pouch. A similar pattern is present in the distribution of the magnitude of cell elongation (Fig. 7.1 C). This radial symmetry of the cell elongation and cell area motivated us to precisely define the center point of the wing pouch (see Appendix G.1). We use this center point (green diamond in Fig. 7.1 D) to quantify the radial component of cell elongation. We find a tangential distribution of cell elongation in the peripheral regions of the wing pouch (Fig. 7.1 D). We quantify the radial distribution of average cell area in Fig. 7.2 A and the radial distribution of the radial component of the cell elongation in Fig. 7.2 B. These results are consistent with *in vivo* observations [90–93].

The culture conditions, developed by our collaborators allow imaging of the developing wing epithelium with a high temporal resolution over around 13 hours. We quantify the radial components of the shear rate $\tilde{v}_{rr}$ and $\tilde{v}_{r\varphi}$ in the wing disc pouch (Fig. 7.2 C). We then calculate average radial shear rate in the tissue. For any nematic tensor t_{ij} we denote componetns of radial averages by capital indices RR and $R\Phi$

$$T_{RR} = \langle t_{rr} \rangle \tag{7.1}$$

$$T_{R\Phi} = \langle t_{r\varphi} \rangle \quad . \tag{7.2}$$

Here $\langle \cdot \rangle$ denotes the area-weighted average over the tissue, r is the radial position and φ is the polar angle (see Fig. 7.2 C).

We then use a modified version of the triangle method [55] to decompose the average radial shear rate components into their cellular contributions. The decomposition is formally the same as in [55] with an additional correlation term S_{IJ} and with all averages replaced by the radial averages as defined in Eq. (7.1) and Eq. (7.2)

$$\tilde{v}_{IJ} = \frac{DQ_{IJ}}{Dt} + T_{IJ} + C_{IJ} + E_{IJ} + D_{IJ} + S_{IJ} \quad . \tag{7.3}$$

We denote individual cellular contributions with the same variable names as in Eq. (2.14). The additional term S_{IJ} arises from a correlation between triangle elongation and ro-
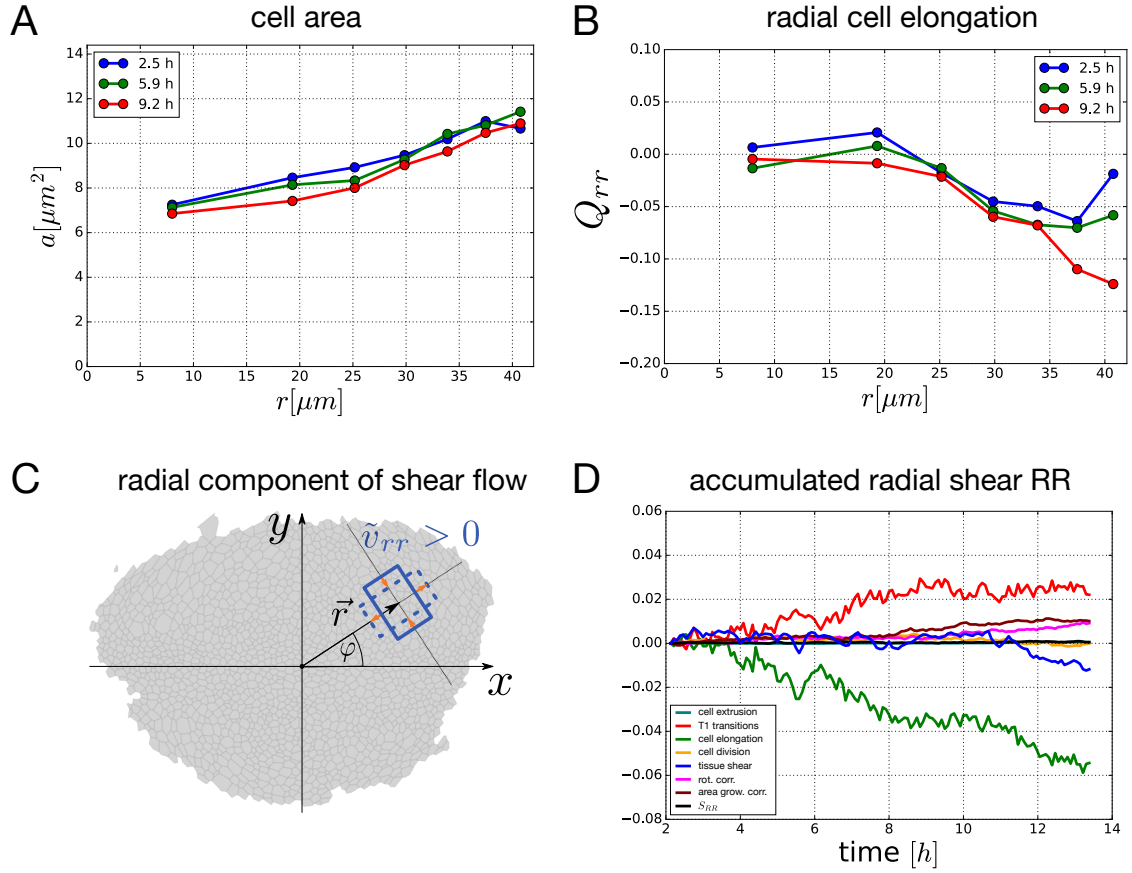
Figure 7.2: A) Average cell area evaluated in concentric rings of equal area at early (blue), middle (green) and late (red) time of the experiment. Cells are smaller in the center of the wing disc pouch and bigger at the periphery. B) Average radial cell elongation Q_{rr} evaluated in concentric rings of equal area at early (blue), middle (green) and late (red) time of the experiment. Radial cell elongation is close to 0 in the center of the wing disc pouch and becomes tangential further away from the center. C) The radial component of the local tissue shear rate $\tilde{v}_{rr}$ is averaged throughout the wing disc pouch to obtain the average radial shear rate $\tilde{v}_{RR}$. D) Accumulated average radial shear $\int_{t_0}^{t} \tilde{v}_{RR} dt$ in the wing disc pouch fluctuates around 0 (blue). However, cell elongation increases tangentially (green) mostly due to shear by the radial T1 transitions (red). Correlation effects also contribute to the tangential elongation of cells (magenta represents correlation between local tissue rotation and cell elongation and brown represents correlation between local area growth and cell elongation, see [55] for details). Contributions from cell divisions (orange), cell extrusions (cyan) and the correlation between cell elongation and rotation around the tissue center S_{RR} (black) are negligible.

tation of cells with respect to the tissue center. In Appendix G.2 we show how to quantify S_{IJ} and we give an expression for DQ_{IJ}/Dt. The correlation term S_{RR} does not contribute significantly to the average radial tissue shear $\tilde{v}_{RR}$ in the experiment we analyze here (black line in Fig. 7.2 D shows cumulative S_{RR}).

We find that although there is very little accumulated radial shear RR component $\int_0^t \tilde{v}_{RR}dt$ in the wing pouch (blue line in Fig. 7.2 D), cells elongate tangentially (green line in Fig. 7.2 D) while at the same time the T1 transitions drive the opposing radial shear $\int_0^t T_{RR}dt$ (red line in Fig. 7.2 D). Since the magnitude of cell elongation is increased by the T1 transitions we can conclude that these are the active T1 transitions. How do these active T1 transitions influence the mechanical stresses in a radially symmetric tissue? In the following, we theoretically investigate the influence of radially oriented active T1 transitions on the tissue mechanics.

7.2 Hydrodynamic theory for a radially symmetric tissue

In this section, we rewrite our hydrodynamic theory in the polar coordinate system and then we solve the theory for the case of rotationally invariant and non-chiral tissue. We determine how the radial active T1 transitions contribute to the radial component of cell elongation Q_{rr}, pressure P and radial velocity of the tissue v_r.

In a polar coordinate system, components of the velocity gradient tensor are

$$v_{rr} = \partial_r v_r \tag{7.4}$$

$$v_{\varphi r} = \partial_r v_\varphi \tag{7.5}$$

$$v_{r\varphi} = \frac{1}{r}\partial_\varphi v_r - \frac{1}{r}v_\varphi \tag{7.6}$$

$$v_{\varphi\varphi} = \frac{1}{r}\partial_\varphi v_\varphi + \frac{1}{r}v_r \quad . \tag{7.7}$$

The isotropic flow decomposition Eq. (2.12) can therefore be written as

$$v_{kk} = \partial_r v_r + \frac{1}{r}\partial_\varphi v_\varphi + \frac{1}{r}v_r = \frac{1}{a}\frac{da}{dt} + k_d - k_e \quad , \tag{7.8}$$

and the shear rate decomposition Eq. (2.16) is

$$\tilde{v}_{rr} = \frac{1}{2}\left(\partial_r v_r - \frac{1}{r}\partial_\varphi v_\varphi - \frac{1}{r}v_r\right) = \frac{dQ_{rr}}{dt} + R_{rr} \tag{7.9}$$

$$\tilde{v}_{r\varphi} = \frac{1}{2}\left(\partial_r v_\varphi + \frac{1}{r}\partial_\varphi v_r - \frac{1}{r}v_\varphi\right) = \frac{dQ_{r\varphi}}{dt} + R_{r\varphi} \quad . \tag{7.10}$$

Force balance Eq. (2.19) in polar coordinates states

$$\partial_r \sigma_{rr} + \frac{1}{r}\sigma_{rr} + \frac{1}{r}\partial_\varphi \sigma_{r\varphi} - \frac{1}{r}\sigma_{\varphi\varphi} = 0 \tag{7.11}$$

$$\frac{1}{r}\partial_\varphi \sigma_{\varphi\varphi} + \partial_r \sigma_{r\varphi} + \frac{2}{r}\sigma_{r\varphi} = 0 \quad . \tag{7.12}$$

Here, we neglected frictional forces.

7.2.1 The general solution for a rotationally invariant tissue

We now solve the hydrodynamic theory for a rotationally invariant, non-chiral tissue. In such system all tensors expressed in polar coordinates are diagonal and all derivatives with respect to the polar angle φ vanish. We neglect the non-linear terms arising from the convected and corotational derivatives.

We use following constitutive equations. For the shear due to topological rearrangements we use Eq. (3.3) without memory effects

$$R_{rr} = \frac{1}{\tau}Q_{rr} + \lambda q_{rr} \quad . \tag{7.13}$$

The influence of the radially oriented active T1 transitions on the tissue mechanics is described by the active shear flow λ.

As in Chapters 3 and 5 shear stress and pressure are described by

$$\tilde{\sigma}_{rr} = \frac{1}{2}\left(\sigma_{rr} - \sigma_{\varphi\varphi}\right) = 2KQ_{rr} + \zeta q_{rr} \tag{7.14}$$

$$P = -\frac{1}{2}\left(\sigma_{rr} + \sigma_{\varphi\varphi}\right) = -\overline{K}\ln\left(\frac{a}{a_0}\right) \quad . \tag{7.15}$$

For the constitutive equation for the preferred cell area a_0 we use

$$\frac{1}{a_0}\frac{da_0}{dt} = \beta - (1 - \epsilon)\,k_d \quad , \tag{7.16}$$

as introduced in Section 2.23. However, we will assume that β is constant.

Combining these constitutive equations together with Eqs. (7.4) - (7.11) we find the following system of equations for v_r, σ_{rr} and $\sigma_{\varphi\varphi}$

$$\partial_r v_r + \frac{1}{r}v_r = \frac{1}{2\overline{K}}\partial_t\left(\sigma_{rr} + \sigma_{\varphi\varphi}\right) + \epsilon k_d + \beta - k_e \quad , \tag{7.17}$$

$$\partial_r v_r - \frac{1}{r}v_r = \frac{1}{2K}\left(\partial_t + \frac{1}{\tau}\right)\left(\sigma_{rr} - \sigma_{\varphi\varphi}\right) + 2\left(\lambda - \frac{\zeta}{2K\tau}\right)q_{rr} \quad , \tag{7.18}$$

$$\sigma_{\varphi\varphi} = r\partial_r\sigma_{rr} + \sigma_{rr} \quad . \tag{7.19}$$

For simplicity, we assumed that $\partial_t\zeta = 0$. Interestingly, this system can be further reduced to a single equation

$$\left[\frac{1}{2}\left(\frac{1}{\overline{K}} + \frac{1}{K}\right)\partial_t + \frac{1}{2K\tau}\right]\left(r^2\partial_r^2\sigma_{rr} + 3r\partial_r\sigma_{rr}\right) = 4\gamma + 2r\partial_r\gamma - r\partial_r g \quad , \tag{7.20}$$

where we have introduced the active shear coefficient γ and growth coefficient g

$$\gamma = \left(\lambda - \frac{\zeta}{2K\tau}\right)q_{rr} \quad , \tag{7.21}$$

$$g = \epsilon k_d + \beta - k_e \quad . \tag{7.22}$$

The active shear coefficient γ contains contributions from both λ and ζ. Here we are interested in the radially oriented active T1 transitions and therefore we assume that the contribution from ζ is not important. However, we will formally keep it in our equations.

In the Eq. (7.20) spatial and temporal differential operators are factorized and thus we can proceed to first integrate the object $r^2\partial_r^2\sigma_{rr} + 3r\sigma_{rr}$ in time, assuming constant

γ and g

$$r^2 \partial_r^2 \sigma_{rr} + 3r\partial_r\sigma_{rr} = C_0 e^{-\frac{\overline{K}}{K+\overline{K}}\frac{t}{\tau}}$$
$$+ 2K\tau \left(4\gamma + 2r\partial_r\gamma - r\partial_r g\right)\left(1 - e^{-\frac{\overline{K}}{K+\overline{K}}\frac{t}{\tau}}\right) \quad , \tag{7.23}$$

where C_0 is an integration constant. In the following, we will consider a stationary state corresponding to $t \gg \tau(1 + K/\overline{K})$

$$r^2\partial_r^2\sigma_{rr} + 3r\partial_r\sigma_{rr} = 2K\tau\left(4\gamma + 2r\partial_r\gamma - r\partial_r g\right) \quad . \tag{7.24}$$

Note that in this stationary state tissue can still flow. We integrate Eq. (7.24) to find the radial component of radial stress gradient

$$\partial_r\sigma_{rr} = \frac{4K\tau\gamma}{r} - \frac{2K\tau}{r^3}\int_0^r r'^2\partial_{r'}g(r')dr' \quad . \tag{7.25}$$

Integration constant was set to 0 because the homogeneous part of solution diverges at $r = 0$. Now we can determine the radial component of cell elongation Q_{rr}, pressure in the tissue and cell area.

Cell elongation

The radial component of cell elongation tensor is

$$Q_{rr} = \frac{1}{4K}\left(\sigma_{rr} - \sigma_{\varphi\varphi}\right) - \frac{1}{2K}\zeta q_{rr} \tag{7.26}$$
$$= -\frac{1}{4K}r\partial_r\sigma_{rr} - \frac{1}{2K}\zeta q_{rr} \tag{7.27}$$
$$= -\tau\left(\lambda q_{rr} - \frac{1}{2r^2}\int_0^r r'^2\partial_{r'}g(r')dr'\right) \quad . \tag{7.28}$$

The tangential distribution of cell elongation observed in the experiment is consistent with positive radial gradient of λ.

Pressure

In order to find the tissue pressure we first integrate the Eq. (7.25) over the radial coordinate we find

$$\sigma_{rr} = \sigma_{rr}|_R - 4K\tau \int_r^R \frac{\gamma(r')}{r'}dr' + 2K\tau \int_r^R \frac{1}{r'^3} \int_0^{r'} r''^2 \partial_{r''} g(r'')dr''dr' \quad , \qquad (7.29)$$

where $\sigma_{rr}|_R$ is the normal stress imposed at $r = R$. Using Eq. (7.29) we find the expression for the radial pressure distribution in the tissue

$$\begin{aligned}
P =& -\frac{1}{2}r\partial_r\sigma_{rr} - \sigma_{rr} \\
=& -\sigma_{rr}|_R - 2K\tau \left[\gamma - 2\int_r^R \frac{\gamma(r')}{r'}dr'\right] \\
& + K\tau \left[\frac{1}{r^2}\int_0^r r'^2\partial_{r'}g(r')dr' - 2\int_r^R \frac{1}{r'^3}\int_0^{r'} r''^2\partial_{r''}g(r'')dr''dr'\right] .
\end{aligned} \qquad (7.30)$$

The last expression on the right hand side can be simplified so that

$$P = -\sigma_{rr}|_R - 2K\tau \left[\gamma - 2\int_r^R \frac{\gamma(r')}{r'}dr'\right] + K\tau \left[g - \frac{2}{R^2}\int_0^R r'g(r')dr'\right] \quad . \qquad (7.31)$$

See Appendix H.1 for the derivation.

A positive radial gradient of γ, corresponding to the positive radial gradient of λ if ζ is negligible, produces higher pressure in the center of the tissue and smaller pressure in the periphery. This is consistent with the observation of smaller cells in the center of the wing disc tissue. However, the same effect can be produced by divisions and extrusions contributing to g. More experimental data will be needed to give a conclusive explanation of the observed cell shape and size patterns.

Radial velocity

The radial tissue velocity is given by

$$v_r = \frac{r}{2\overline{K}}\partial_t\sigma_{rr} + \frac{1}{r}\int_0^r r'g(r')dr' \quad . \tag{7.32}$$

The time dependence of σ_{rr} in the stationary state is due to a possible time dependence of the boundary condition $\sigma_{rr}|_R$. The radial velocity v_r is determined by the growth coefficient g and boundary stress dynamics $\partial_t\,\sigma_{rr}|_R$ and it does not depend directly on the active T1 transitions in the tissue. Therefore, in order to affect the tissue flow patterns the active T1 transitions have to perturb cell division or cell extrusion rate.

7.3 Mechanosensitive tissue growth

In this section, we investigate how the pressure induced by the radially oriented active T1 transitions can affect the growth of the epithelial tissue. To this end, we introduce a mechanosensitive model for the tissue growth coefficient $g = \epsilon k_d + \beta - k_e$, introduced in Eq. (7.22). We discuss the influence of the radially distributed active T1 transitions on the tissue pressure and how they can influence the tissue growth. Mechanosensitivity of the tissue growth coefficient g can be expressed by writing

$$g = G(P) \quad , \tag{7.33}$$

where $G(P)$ is some function of pressure.

7.3.1 Small variations of pressure

Let us expand Eq. (7.33) around a pressure P_0 to linear order

$$g = g_0 + \frac{1}{\overline{\eta}}\left(P_0 - P\right) \quad , \tag{7.34}$$

where $g_0 = g(P_0)$. The proportionality constant $\overline{\eta}$ is positive and has units of viscosity. The choice of sign indicates that we are in a regime where higher values of pressure

suppress growth and lower ones to induce it. Combining this linear mechanosensitive model with Eq. (7.31) we find

$$g = \frac{K\tau}{\bar{\eta} + K\tau}\langle g \rangle + \frac{P_0 + \sigma_{rr}|_R + \bar{\eta}g_0}{\bar{\eta} + K\tau} + \frac{2K\tau}{\bar{\eta} + K\tau}\left(\gamma - 2\int\limits_r^R \frac{\gamma(r')}{r'}dr'\right) \quad , \qquad (7.35)$$

where $\langle g \rangle$ is the average growth coefficient in the tissue

$$\langle g \rangle = \frac{2}{R^2}\int\limits_0^R rg(r)dr \quad . \qquad (7.36)$$

We now average Eq. (7.35) over the tissue to find

$$\langle g \rangle = g_0 + \frac{P_0 + \sigma_{rr}|_R}{\bar{\eta}} + \frac{2K\tau}{\bar{\eta}}\frac{2}{R^2}\int\limits_0^R r\left(\gamma - 2\int\limits_r^R \frac{\gamma(r')}{r'}dr'\right)dr \quad . \qquad (7.37)$$

Interestingly, the second term on the right-hand side of this expression vanishes for any continuous function $\gamma(r)$, see Section H.2 for proof. Therefore

$$\langle g \rangle = \frac{P_0 + \sigma_{rr}|_R}{\bar{\eta}} + g_0 \quad , \qquad (7.38)$$

and we find the expression for the tissue growth coefficient

$$g = \frac{P_0 + \sigma_{rr}|_R}{\bar{\eta}} + g_0 + \frac{2K\tau}{\bar{\eta} + K\tau}\left(\gamma - 2\int\limits_r^R \frac{\gamma(r')}{r'}dr'\right) \quad . \qquad (7.39)$$

Now we can discuss the growth of the tissue. We consider a tissue with free boundaries

$$\sigma_{rr}|_R = 0 \quad . \qquad (7.40)$$

To determine how the tissue boundary moves, we need to evaluate the radial velocity

v_r at $r = R$

$$\frac{dR}{dt} = v_r(R) = \frac{R}{2}\langle g\rangle \quad .\tag{7.41}$$

We have already determined $\langle g\rangle$ in Eq. (7.38) and therefore

$$\frac{dR}{dt} = \frac{R}{2}\left(\frac{P_0}{\overline{\eta}} + g_0\right) \quad .\tag{7.42}$$

Therefore, the tissue growth is independent of radially oriented active T1 transitions. It is completely determined by the parameters $P_0/\overline{\eta}$ and g_0 and the size of the tissue either exponentially grows or exponentially shrinks in time. Only in the fine tuned case $P_0 = -\overline{\eta}g_0$, the size of the tissue does not change.

This result has strong implications on the possible role of active T1 transitions. As long as the variations of pressure in the tissue remain in the regime in which the linear approximation Eq. (7.34) is valid, the active T1 transitions do not influence the tissue size.

It is important to note that we neglected non-linear terms arising from the convected and corotational derivatives. We also neglected frictional forces. Both of these effects could change the conclusion of this section and it will be interesting to investigate them in future. However, in the following section, we will keep both approximations and consider a particular non-linear mechanosensitive constitutive equation Eq. (7.33).

7.3.2 Large variations of pressure

Since in the linear regime of Eq. (7.33) the active radial T1 transitions cannot affect the overall tissue growth, in this subsection we investigate a particular non-linear mechanosensitive model as an example of a tissue whose growth is controlled by the active T1 transitions.

We consider a tissue in which the rate of cell divisions is not affected by the pressure. Extrusions are not present at low pressures and they are induced when pressure is higher than P_0. This two properties can be described by the following constitutive

equation for the growth coefficient

$$g = g_0 - \frac{1}{\eta} \left(P - P_0 \right) \theta \left(P - P_0 \right) \quad . \tag{7.43}$$

Here, g_0 is the contribution of divisions to the growth coefficient and it does not depend on pressure. η is a positive constant with units of viscosity and θ is Heaviside theta function. We assume that in a stress free tissue $g = g_0$ which corresponds to $P_0 \geq 0$.

For simplicity, we assume a linear radial profile of the active shear coefficient

$$\gamma = \Gamma r \quad , \tag{7.44}$$

where Γ is a positive constant. Now, using Eq. (7.31), Eq. (7.43) and Eq. (7.44) we find the equation for pressure

$$P = -2K\tau\Gamma \left(3r - 2R \right) + K\tau \left[g_0 - \frac{1}{\eta} \left(P - P_0 \right) \theta \left(P - P_0 \right) - \langle g \rangle \right] \quad . \tag{7.45}$$

Starting from $r = R$, the pressure linearly increases towards the center of the tissue until a point $r = r_0$ is reached where $P = P_0$. At that position in the tissue the extrusions are induced. For $r < r_0$ the pressure still increases linearly towards the tissue center but with a different slope. The position r_0 at which the pressure reaches the value P_0 is

$$r_0 = \frac{2}{3}R - \frac{1}{6K\tau\Gamma} \left[P_0 - K\tau \left(g_0 - \langle g \rangle \right) \right] \quad . \tag{7.46}$$

This equation still contains $\langle g \rangle$ and we need to find another equation to determine r_0 and $\langle g \rangle$. To this end, we can use the following property

$$\langle P \rangle = 0 \quad , \tag{7.47}$$

that follows from averaging the Eq. (7.31) over the tissue and using the result of Appendix H.2. By explicitly evaluating the average pressure in the system we are

considering, we find that Eq. (7.47) is equivalent to

$$r_0^2 \frac{K\tau}{\eta + K\tau} \left[4\Gamma \left(R - r_0 \right) + g_0 - \langle g \rangle \right] = \frac{P_0 r_0^2}{\eta + K\tau} + \left(g_0 - \langle g \rangle \right) R^2 \qquad (7.48)$$

The system of Eqs. (7.46) and (7.48) can be solved numerically for r_0 and $\langle g \rangle$ and we can calculate the radial component of velocity at radius R

$$v_r(R) = \frac{R}{2} \langle g \rangle \quad . \qquad (7.49)$$

Note that when $r_0 < 0$ pressure is greater than P_0 everywhere in the tissue and $\langle g \rangle = g_0$. The value of radius $R = R_M$ for which the velocity $v_r(R)$ vanishes, corresponds to the equilibrium size of the tissue. In Fig. 7.3 A we show R_M as a function of Γ. We use an arbitrary length unit L since the other model parameters do not contain a length scale.

We can conclude that radially oriented active T1 transitions can indeed determine the equilibrium tissue size. A higher active shear flow λ due to radially oriented active T1 transitions corresponds to a higher Γ and therefore to a smaller equilibrium tissue size.

Finally, we quantify the dynamics of tissue growth. If the tissue growth is slow enough so that we can assume, to a good approximation, that the tissue is always in the stationary state, we can determine how much time it takes for the tissue to increase its radius from an initial value R_0 to R by numerically evaluating

$$t = \int\limits_{R_0}^{R} \frac{1}{v_r(R')} dR' \quad . \qquad (7.50)$$

Figure 7.3 B shows the tissue radius as a function of time. At early times the pressure in the center of the tissue is below P_0 and the exponential growth rate is independent of the value of Γ. When the pressure in the middle of the tissue increases sufficiently to induce cell extrusions, tissue growth is slowed and it saturates at the equilibrium value $R_M(\Gamma)$.
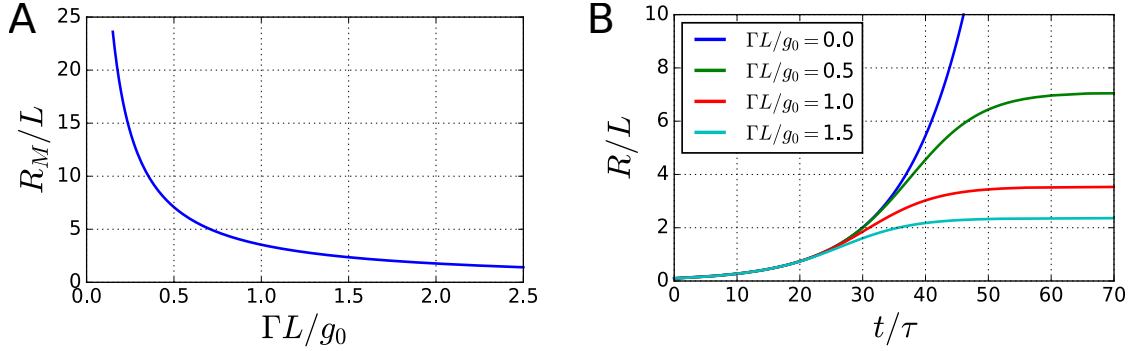
Figure 7.3: A) Equilibrium tissue radius R_M as a function of the gradient of active shear coefficient Γ. Stronger radially oriented T1 transitions correspond to a higher Γ and thus to a smaller equilibrium tissue size. L is an arbitrary length scale. B) Dynamics of tissue radius $R(t)$ for different values of Γ. At early times, when the pressure is everywhere below P_0, the tissue grows exponentially independent of the value of Γ. When the pressure in the center of the tissue increases sufficiently to induce extrusions, the tissue growth is slowed until it saturates at the equilibrium value $R_M(\Gamma)$. We use the initial tissue radius value $R_0 = 0.1L$. Other parameters used are: $\eta/(K\tau) = 0.5$, $g_0\tau = 0.2$ and $P_0/K = 0.5$.

7.4 Summary

In this chapter, we investigated the influence of active T1 transitions in a radially symmetric geometry. We first analyzed experimental data that shows a radial pattern of cell properties in a wing disc pouch region. We decomposed the radial shear rate into cellular components following the triangle method [55] and we found that the contribution to the radial shear rate from T1 transition contributes to the increase of tangential cell elongation.

We then solved the hydrodynamic theory of tissues for a radially symmetric, rotationally invariant circular tissue and we found general analytic expressions for cell elongation, tissue stresses and radial tissue velocity in a stationary state, in presence of active T1 transitions, cell divisions and extrusions.

Finally, we included a mechanosensitive model of cell divisions and cell extrusions to investigate a possible role of radially oriented active T1 transitions in the regulation of tissue size. We found that as long as the variations of pressure in the tissue are sufficiently small so that the mechanosensitive model is in a linear regime, the active T1 transitions have no effect on the tissue growth. However, once the active T1

transitions are sufficiently strong to create variations of pressure inside the tissue that take the mechanosensitive model outside of its linear regime, the equilibrium tissue size can be determined by the radially oriented T1 transitions.

Chapter 8

Summary and outlook

In this thesis, we used a hydrodynamic theory of epithelial tissues to investigate mechanics and rheology of a developing fruit fly wing epithelium. Analysis of experiments performed by our collaborators allowed us to develop a relevant theoretical description and focus on interesting new phenomena we encountered in the experimental data. The hydrodynamic theory we developed allowed us to further theoretically investigate properties of epithelial tissues.

In Chapter 2 we constructed a general hydrodynamic theory of developing epithelial tissues. Many ingredients we used were already present in the literature [41, 42, 46, 94]. Our theory treats cell elongation, cell area and internal cell polarity as observable quantities and preserves the information about cell state properties on a coarse-grained tissue scale. We established a relationship between large-scale tissue flows and cellular processes by separating contributions of individual cellular processes to the tissue shear flow and tissue area change. Such shear decomposition can be realized exactly using a recently developed triangle method [54, 55]. Finally, we propose general linear constitutive equations to describe stresses in the tissue as well as to describe how cell rearrangements contribute to the overall tissue flow. The theory presented here assumes that epithelia are flat, two-dimensional tissues. Generalization to three dimensions is straightforward. For a description of curved tissues, a covariant version of the theory will be required.

In Chapter 3 we investigated shear flows of a developing fruit fly wing epithelium. The flow of the wing during pupal morphogenesis can be described by our hydrodynamic theory. We found that both active processes introduced in Chapter 2 are present in the developing wing. Moreover, we found that the topological rearrangements in

the tissue respond to cell shape with a memory that lasts about 4 hours. We then investigated rheology of tissue shear flow. We found that in the absence of memory effects the tissue behaves as a Maxwell viscoelastic material. The long time viscosity stems from the tissue fluidization by the topological rearrangements. However, when the memory time-scale τ_d is sufficiently long we find that the shear stress in the tissue exhibits transient oscillations. This corresponds to the situation in the developing wing. We show that the response function describing the wing shear flow can be represented by a simple mechanical network that contains a spring connected in series with parallel connection of a dashpot and an inerter. We estimated the value of inertance to be on the order of $2 \cdot 10^4 kg$ and thus the memory effects we observed cannot arise from the inertia of the wing. Interestingly, we found that the same constitutive equation that describes shear flow of the fruit fly wing epithelium also describes shear flows in a viscoelastic nematic gel close to equilibrium. We further discussed similarities and differences between the two theories. Finally, we discussed the two active processes that drive tissue shear flows and the influence of the boundary conditions on the tissue shear flows. Results of this chapter hold for homogeneous tissue flows. A future challenge will be to investigate a more detailed spatial tissue flow profiles.

In Chapter 4 we investigated spontaneous rotations in a system of two coupled nematics. We defined soft and hard nematics based on their interaction with an external field. The magnitude of a soft nematic is proportional to that of the external field while the magnitude of a hard nematic does not change. In a passive system, the two nematics are either aligned or opposed in the steady state. Interestingly, we found that in the regime of coupling parameters that is not accessible to a passive system, steady states exist where the two nematics rotate together with a constant angular velocity. Analysis of the stability showed that the rotating steady states are stable whenever they exist. It would be interesting to find a biological system that features a soft and hard nematic in the rotating steady state.

In Chapter 5 we analyzed how cellular processes contribute to the area changes in the fruit fly wing blade during pupal morphogenesis. Cells in the blade undergo 1 to 2 rounds of division. However, at the same time, the wing blade area does not change significantly. This is achieved by reducing the average cell area by divisions. Cell divisions do not seem to be significantly altered mechanical perturbations and

it is not clear that we should expect a significant influence of mechanics on the cell division rate in the wing. We then proposed a mechanosensitive model to describe cell extrusions and we determined parameters of the model by fitting it to the experimental data. We found that a single set of tissue parameters τ_e, ϵ and $\kappa_e/\overline{K}$ can describe wild type wings, mechanically perturbed wings, wings imaged at increased temperature and $cdc2$ mutant wings where the divisions are genetically inhibited when the temperature is increased. Interestingly, the $dumpy$ mutant wing cannot be described by this model indicating that another type of extrusions regulation is present in that mutant wing. In future, we expect that improved data quality will allow for a more detailed investigation of extrusions in the developing fruit fly wing.

In Chapter 6 we studied the influence of boundary conditions on the dynamics of the fruit fly wing shape during the pupal morphogenesis. We devised a rectangle model of the wing tissue where blade and hinge region of the wing are represented by rectangular homogeneous pieces of tissue in contact. They are connected to the surrounding hard cuticle by lateral connections. We included these boundary conditions in the model as elastic springs that respond to change of blade and hinge height and length. Friction between the wing tissue and the surrounding material was included by an effective friction that acts on the proximal and distal edges of the rectangles. We used experimental measurements of the flow in the wings that were mechanically perturbed by laser ablation and a wild type wing to determine the parameters of the model. We then showed that the flow of the $dumpy$ mutant wing can be understood as the wild type wing tissue with a perturbed stiffness of boundary linkers. The rectangle model is useful to describe the average behavior of the wing blade and hinge regions. However, it does not allow us to investigate spatial profiles of cell properties and the tissue flow. To discuss these properties a more detailed implementation of the hydrodynamic theory of tissues will be required.

In Chapter 7 we investigated the influence of active T1 transitions on the mechanics of a radially symmetric tissue. We first analyzed tissue flows in an explanted wing disc tissue, cultured by our collaborators for about 13 hours. We found clear radial patterns of radial cell elongation component and cell area, consistent with the measurements $in\ vivo$ [90–93]. High temporal resolution imaging allowed us to quantify the cellular contributions to the radial tissue shear rate. This decomposition indicated that active

radially oriented T1 transitions are present in this tissue. We then solved our hydrodynamic theory of tissues for a radially symmetric, rotationally invariant epithelium where radially oriented active T1 transitions are present. We obtained analytical expressions that describe radial cell elongation, pressure and radial flow patterns. We found that when cell divisions or cell extrusions in the tissue are mechanosensitive the radially oriented T1 transitions can determine the tissue size by perturbing the pressure distribution in the tissue. However, we found that this is only possible when the proposed mechanosensitive model is nonlinear. We expect that more extensive experiments will allow us to determine whether the active T1 contribute to the determination of the wing disc epithelium size.

The hydrodynamic theory of epithelia that we constructed in this thesis proved to be a valuable tool in study of tissue mechanics. It allowed us to combine conservation laws and force balance with tissue specific constitutive equations. Important ingredients of our hydrodynamic theory are memory effects in constitutive equations and identification of two distinct active cellular processes. We have used the hydrodynamic theory to describe a novel tissue rheology due to memory effects and actively driven tissue flow, construct and experimentaly valide a mechanosensitive constitutive equation and to investigate the role of active T1 transitions in the development of epithelia. Moreover, we used our hydrodynamic theory to compare mechanical properties of mutated and wild type tissues. Although in most of this work we studied average properties of cells in a tissue and assumed that the tissues are homogeneous, in the last chapter we demonstrated how our theory can be used to describe inhomogeneous tissue flows.

An important challenge in future will be to extend our theory to curved epithelia. This would allow us to investigate a wide range of developing epithelia that posses spherical, oval or cyllindrical geometry. Also, in the hydrodynamic theory presented here all constitutive equations are local. Introducing a coupling between orientational order parameters in our theory would open door to a completely new phenomena that we have not considered here.

Appendices

Appendix A

Definitions and conventions

A.1 Convected and corotational derivatives

In a material flowing with a velocity v_i we define convected derivative of a scalar field S as

$$\frac{\mathrm{d}S}{\mathrm{d}t} = \frac{\partial S}{\partial t} + v_k \partial_k S \quad . \tag{A.1}$$

The convected corotational derivative of a nematic tensor field Q_{ij} is defined as [55]

$$\frac{\mathrm{D}Q_{ij}}{\mathrm{D}t} = \frac{\partial Q_{ij}}{\partial t} + v_k \partial_k Q_{ij} - 2 \left(c\omega + (1-c)\frac{d\phi}{dt} \right) \epsilon_{ik} Q_{kj} \quad , \tag{A.2}$$

where $c = \tanh(2|Q_{ij}|)/(2|Q_{ij}|)$, $-\omega\epsilon_{ij} = (\partial_i v_j - \partial_j v_i)/2$ and ϕ is the orientation angle of the nematic tensor field Q_{ij} . For $|Q_{ij}| \ll 1$ this becomes convected corotational Jaumann derivative [95]

$$\frac{\mathrm{D}Q_{ij}}{\mathrm{D}t} = \frac{\partial Q_{ij}}{\partial t} + v_k \partial_k Q_{ij} + \omega_{ik} Q_{kj} + \omega_{jk} Q_{ik} \quad , \tag{A.3}$$

where $\omega_{ij} = (\partial_i v_j - \partial_j v_i)/2$.

A.2 Fourier transform

The following convention for Fourier transform is used

$$f(\omega) = \int\limits_{-\infty}^{\infty} f(t)e^{-i\omega t}dt \tag{A.4}$$

$$f(t) = \frac{1}{2\pi} \int\limits_{-\infty}^{\infty} f(\omega)e^{i\omega t}d\omega \quad . \tag{A.5}$$

Here $f(\omega)$ is the Fourier transform of the function $f(t)$.

A.3 Totally antisymmetric matrix in 2D

The totally antisymmetric two-dimensional matrix ϵ_{ij} in this work is defined as

$$\epsilon_{ij} = \begin{pmatrix} 0 & -1 \\ 1 & 0 \end{pmatrix} \quad . \tag{A.6}$$

Appendix B

Experimental data used in this work

Many results reported in this thesis are motivated and are driven by the experimental data. All experiments and a large part of data processing were performed by our collaborator from the group of Suzanne Eaton at the Max Planck Institute of Molecular Cell Biology and Genetics. In particular, experiments with pupal wings were performed by Raphael Etournay and experiments with the wing disc were performed by Natalie Dye.

In this section, we briefly present the experiments that were studied and analyzed in this work. We discuss the results of experiments in corresponding chapters. Technical details are not described and can be found in publications [54, 68]. In all experiments the image of the wing tissue we analyze is a two-dimensional projection of the wing surface on a plane perpendicular to the optical axis of the microscope.

B.1 Wild type pupal wings

We study three wild type pupal wings. We observe that during wing pupal morphogenesis the wing epithelium undergoes large-scale flows that reshape the wing over around 17 hours. In Fig. B.1 A blue stripes are tracked throughout the experiment and show the pattern of the wing tissue flow. The shape of a wild type wing at three different timepoints is shown in the top row of Fig. B.1 B top.

B.2 Dumpy mutant wing

A *dumpy* mutant wing shows a very strong phenotype. It shorter and concave at the distal end. In Fig. B.1 B we compare a wild type and a *dumpy* mutant wing and we show that the characteristic dumpy phenotype arises during the pupal morphogenesis. In 1940 C. H. Waddington argued that the misshaping of the dumpy wing is due to perturbation of forces in the wing [96]. Dumpy protein is present in the extracellular matrix that connects tissue to the surrounding cuticle and it forms large filaments, about 1 μm long [84]. In the pupal wing it is mostly located around the wing margin [54] and therefore we expect that the shape of the dumpy mutant wing can be accounted for by compromised boundary conditions. We investigate this in Chapter 6.

B.3 Mechanically perturbed pupal wings

Our collaborators performed laser ablations along the margin of the wild type wings, between the wing tissue and the surrounding cuticle. The ablations were performed about 7 hours after the start of the pupal morphogenesis. Due to technical difficulties, earlier ablations were not possible.

Fig. B.1 C shows shapes of the two mechanically perturbed wings at the end of the pupal morphogenesis. Ablations are performed on the anterior side of the wing (left) and on the distal side (right). Distal ablation produces a wing shape similar to the dumpy mutant wing. We use the mechanically perturbed wings to investigate the role of boundary conditions in the wing morphogenesis.

B.4 Temperature perturbation and cdc2 mutant wings

In Chapter 5 we use experimental data obtained from wild type wings that were placed at $30°C$ during the pupal morphogenesis. The shape of these wings does not show a strong phenotype but the cellular contributions to the overall tissue deformation do differ from wild type wings.

Together with the wings at increased temperature, we use the experimental data
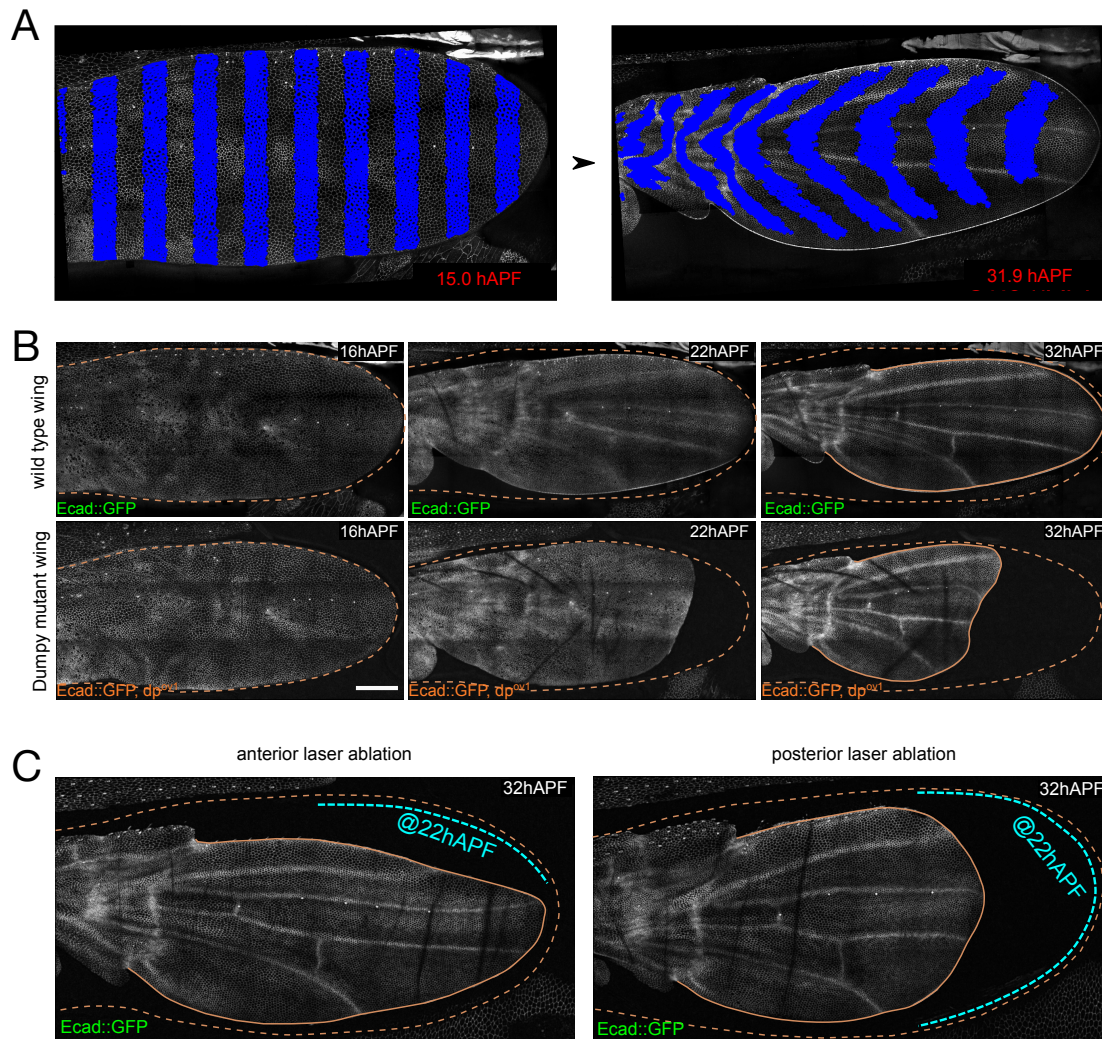
Figure B.1: A) Blue regions are tracked over the course of pupal morphogenesis. Comparison of left and right image visualizes the large scale tissue flows that reshape the fly wing. B) Comparison of pupal development of a wild type wing (top) and a dumpy mutant wing (bottom) reveals that the shape defect characteristic for the dumpy mutant phenotype arises during the pupal morphogenesis. C) Perturbation of extracellular matrix by laser ablations produces misshaped wings. Left: extracellular matrix has been ablated on the anterior side of the wing. Right extracellular matrix has been ablated on the distal side of the wing. Ablations are indicated by the teal line. Source: adapted from ref. [54].

obtained from *cdc2* mutant wings. In the homozygous *cdc2* mutants in which both alleles of the gene have been mutated cells stop dividing when the temperature is

$30°C$. In the heterozygous mutant, in which only one allele has been mutated, cells divide but the development is somewhat different from the wild type at the same temperature.

B.5 Synchronization of the pupal wing data

It is difficult to precisely know, in terms of the developmental time, at how many hours after the pupa formation (hAPF) an experiment starts. In this thesis the precise relative timing of experiments is important only in Chapter 6. In order to synchronize the timing of different movies we use two methods. In wild type wing experiments we align the time axis of different movies so that the maximum of the cell elongation curves coincide. In experiments with perturbed wigs the time axis is synchronized by our collaborators at a time point when the histoblast nests fuse [54]. These synchronizations allow us to position different experiments in time relative to each other. Finally, as a reference, we choose the starting point of the first wild type wing experiment to be 15 hAPF.

B.6 Cultured wing disc epithelium

Our collaborators developed a new culturing method that allows us to observe development of explanted wing disc epithelium at high temporal resolution (not published at the moment). The wing disc data we analyze in Chapter 7 comes from a cultured wing disc that was explanted at about 90 hours after the beginning of the larval stage of development. This corresponds to about three-quarters of the larval developmental time. At that time the wing disc pouch, from which the wing blade will form, is patterned in dosro-ventral and anterio-posterior compartments (see Fig. 7.1 A).

Appendix C

Mechanical networks

This appendix was published in our recent publication [66]. Due to its importance for discussion in Chapter 3 we reproduce it here with minor modifications.

C.1 Real and imaginary parts of a mechanical network response function

We discuss here some properties of the response function of serial and parallel connections of two mechanical elements with response functions $\chi_1(\omega)$ and $\chi_2(\omega)$. The mechanical response function of a parallel connection of these elements is

$$\chi_{\text{parallel}} = \chi_1 + \chi_2 \tag{C.1}$$

so that

$$\text{Re}\,\chi_{\text{parallel}} = \text{Re}\,\chi_1 + \text{Re}\,\chi_2 \tag{C.2}$$

$$\text{Im}\,\chi_{\text{parallel}} = \text{Im}\,\chi_1 + \text{Im}\,\chi_2 \quad . \tag{C.3}$$

The response function of a serial connection is

$$\chi_{\text{serial}} = \frac{\chi_1 \chi_2}{\chi_1 + \chi_2} \quad , \tag{C.4}$$

which can be written in terms of real and imaginary parts

$$\text{Re}\,\chi_{\text{serial}} = \frac{\text{Re}\,\chi_1\,\text{Re}\,\chi_2\,(\text{Re}\,\chi_1 + \text{Re}\,\chi_2) + \text{Re}\,\chi_1\,[\text{Im}\,\chi_2]^2 + \text{Re}\,\chi_2\,[\text{Im}\,\chi_1]^2}{(\text{Re}\,\chi_1 + \text{Re}\,\chi_2)^2 + (\text{Im}\,\chi_1 + \text{Im}\,\chi_2)^2} \qquad (\text{C.5})$$

$$\text{Im}\,\chi_{\text{serial}} = \frac{\text{Im}\,\chi_1\,\text{Im}\,\chi_2\,(\text{Im}\,\chi_1 + \text{Im}\,\chi_2) + \text{Im}\,\chi_1\,[\text{Re}\,\chi_2]^2 + \text{Im}\,\chi_2\,[\text{Re}\,\chi_1]^2}{(\text{Re}\,\chi_1 + \text{Re}\,\chi_2)^2 + (\text{Im}\,\chi_1 + \text{Im}\,\chi_2)^2} \qquad (\text{C.6})$$

By inspecting Eqs. (C.2) and (C.5) we conclude that if the real parts of the response functions of two elements in a serial or parallel connection have the same sign, this sign is preserved in the real part of the response function of the connection. The same is true for the imaginary parts in Eqs. (C.3) and (C.6).

C.2 Response function of a mechanical network with a spring in series with a parallel connection of an inerter and a dashpot

We calculate here the response function of the mechanical network shown in Fig. 3.6E. Using Eq. (C.1) we find that the response function of a parallel connection of an inerter with inertance m and dashpot with viscosity $\bar{\eta}$ reads

$$\chi_{m,\bar{\eta}} = i\omega m + \bar{\eta} \quad . \qquad (\text{C.7})$$

The full response function is found using Eq. (C.4) for a serial connection of a spring with elastic constant k and parallel connection of an inerter and dashpot

$$\begin{aligned}\chi &= \frac{\frac{k}{i\omega}\left(i\omega m + \bar{\eta}\right)}{i\omega m + \bar{\eta} + \frac{k}{i\omega}} \\ &= \bar{\eta}\,\frac{1 + i\omega\frac{m}{\bar{\eta}}}{i\omega\frac{\bar{\eta}}{k}\left(1 + i\omega\frac{m}{\bar{\eta}}\right) + 1} \quad . \end{aligned} \qquad (\text{C.8})$$

Comparing with the Eq. (3.8) we can identify $\bar{\eta} = 2K\tau$, $k = 2K$ and $m = 2K\tau\tau_d$.

Appendix D

Active and passive viscoelastic nematic gels

This appendix was published in our recent publication [66]. Due to its importance for discussion in Chapter 3, we reproduce it here with minor modifications.

D.1 Onsager theory of viscoelastic nematic gel

Here we derive hydrodynamic equations for a viscoelastic nematic gel close to equilibrium and we discuss parameter regimes which reproduce Eq. (3.3). Our derivation is similar to the one given in the ref. [53], but for a one-component, nematic gel.

We start by writing conservation equations for density and momentum

$$\partial_t \rho + \partial_i \left(\rho v_i \right) = 0 \tag{D.1}$$

$$\partial_t g_i - \partial_j \sigma_{ij}^{\mathrm{tot}} = 0 \quad , \tag{D.2}$$

where $g_i = \rho v_i$ and $\sigma_{ij}^{\mathrm{tot}}$ is the total two-dimensional stress. We treat the local elastic shear strain Q_{ij} as a thermodynamic state variable. We also include in our description a nematic order parameter q_{ij} describing other internal anisotropies, motivated by the cell polarity in tissues. Here we will discuss the case when q_{ij} is not spontaneously generated in equilibrium. Assuming that the dynamics of elastic shear strain Q_{ij} and nematic order parameter q_{ij} are sufficiently slow, we introduce the free energy density of the gel as $f(\rho, Q_{ij}, q_{ij})$.

We define the elastic shear stress as being the thermodynamic conjugate quantity

to the elastic shear strain Q_{ij}

$$\sigma_{ij}^{\mathrm{el}} = \frac{\delta f}{\delta Q_{ij}} \quad . \tag{D.3}$$

We also allow for ATP-driven active processes described by the chemical reaction rate r and the chemical potential difference between ATP molecule and hydrolysis products $\Delta\mu$.

Using the free energy density $f(\rho, Q_{ij}, q_{ij})$, we find the expression for the density of entropy production rate $\dot{\sigma}$

$$T\dot{\sigma} = \sigma_{ij}v_{ij} - \sigma_{ij}^{\mathrm{el}}\frac{\mathrm{D}Q_{ij}}{\mathrm{D}t} + H_{ij}\frac{\mathrm{D}q_{ij}}{\mathrm{D}t} + r\Delta\mu \quad . \tag{D.4}$$

Here $\sigma_{ij} = \sigma_{ij}^{\mathrm{tot}} + \rho v_i v_j + P\delta_{ij}$, $v_{ij} = 1/2(\partial_i v_j + \partial_j v_i)$ is the symmetric part of velocity gradient tensor and H_{ij} is the nematic molecular field conjugate to q_{ij} defined as

$$H_{ij} = -\frac{\delta f}{\delta q_{ij}} \quad . \tag{D.5}$$

For simplicity, we ignored here terms associated to the gradients of chemical potential and elastic shear strain, and we discuss traceless symmetric components. Identifying the thermodynamic fluxes $\tilde{\sigma}_{ij}$, $\mathrm{D}Q_{ij}/\mathrm{D}t$, $\mathrm{D}q_{ij}/\mathrm{D}t$ and r, and the corresponding forces $\tilde{v}_{ij}$, $-\sigma_{ij}^{\mathrm{el}}$, H_{ij} and $\Delta\mu$, we write the phenomenological equations

$$\tilde{\sigma}_{ij} = 2\eta\tilde{v}_{ij} + \sigma_{ij}^{\mathrm{el}} - \beta_1 H_{ij} + \left(\Theta q_{ij} + \overline{\Theta}Q_{ij}\right)\Delta\mu \tag{D.6}$$

$$\frac{\mathrm{D}Q_{ij}}{\mathrm{D}t} = \tilde{v}_{ij} - \Gamma\sigma_{ij}^{\mathrm{el}} + \frac{1}{\beta_2}H_{ij} + \left(\psi q_{ij} + \overline{\psi}Q_{ij}\right)\Delta\mu \tag{D.7}$$

$$\frac{\mathrm{D}q_{ij}}{\mathrm{D}t} = \beta_1\tilde{v}_{ij} - \frac{1}{\beta_2}\sigma_{ij}^{\mathrm{el}} + \gamma H_{ij} + \left(\theta q_{ij} + \overline{\theta}Q_{ij}\right)\Delta\mu \tag{D.8}$$

$$\begin{aligned} r = &- \left(\Theta q_{ij} + \overline{\Theta}Q_{ij}\right)\tilde{v}_{ij} - \left(\psi q_{ij} + \overline{\psi}Q_{ij}\right)\sigma_{ij}^{\mathrm{el}} \\ &+ \left(\theta q_{ij} + \overline{\theta}Q_{ij}\right)H_{ij} + \Lambda\Delta\mu \quad . \end{aligned} \tag{D.9}$$

Here, the Onsager symmetry relations have been taken into account. We have included ATP consumption terms coupling to fluxes of different tensorial order through Onsager coefficients proportional to the elastic shear strain Q_{ij} and nematic order parameter q_{ij}. Note that since elastic shear strain is conjugate to the elastic shear stress, the

Onsager coefficient relating $\tilde{v}_{ij}$ to the change of shear strain Q_{ij} can be set to 1 without loss of generality, see [53].

One can already note that Eq. (D.7) is in the form of Eq. (2.16) if we identify $R_{ij} = \Gamma \sigma_{ij}^{\text{el}} - H_{ij}/\beta_2 - \psi \Delta\mu q_{ij} - \overline{\psi} \Delta\mu Q_{ij}$. We now show that this general description can result in the delayed response of R_{ij} discussed in the main text, produced by the relaxation dynamics of q_{ij}.

In the remaining part of this appendix, we consider the following simple choice for the elastic stress and molecular field

$$\sigma_{ij}^{\text{el}} = 2K Q_{ij} \tag{D.10}$$

$$H_{ij} = -\kappa q_{ij} \quad . \tag{D.11}$$

D.1.1 Passive gel

Let us first consider the case of a passive gel which would not consume ATP. Using Eqs. (D.7) and (D.8), the tensor R_{ij} can be expressed as a function of the shear strain Q_{ij}

$$\left[1 + \frac{1}{\gamma\kappa \left(1 - \frac{\beta_1}{\gamma\beta_2}\right)} \frac{\text{D}}{\text{D}t} \right] R_{ij} = 2K \frac{\Gamma - \frac{1}{\beta_2^2 \gamma}}{1 - \frac{\beta_1}{\gamma\beta_2}} Q_{ij} + \frac{2K\Gamma + \kappa\frac{\beta_1}{\beta_2}}{\gamma\kappa \left(1 - \frac{\beta_1}{\gamma\beta_2}\right)} \frac{\text{D}}{\text{D}t} Q_{ij} \quad . \tag{D.12}$$

We find that the choice $\tau_d = 1/[\gamma\kappa(1 - \beta_1/(\gamma\beta_2))]$ and $\tau = [1 - \beta_1/(\gamma\beta_2)]/[2K(\Gamma - 1/(\beta_2^2\gamma))]$ allows to identify Eq. (D.12) with Eq. (3.3). The last term on the right-hand side of Eq. (D.12), involving the derivative of Q_{ij}, is not present in Eq. (3.3). The dimensionless prefactor in front of this term, $\alpha = [2K\Gamma + \kappa\beta_1/\beta_2]/[\gamma\kappa(1 - \beta_1/(\gamma\beta_2))]$, can be set to 0 if $\beta_1 = -2K\Gamma\beta_2/\kappa$. This choice implies the following inequality

$$\frac{\tau}{\tau_d} = \frac{[2K\Gamma + \gamma\kappa]^2}{2K\left(\Gamma - \frac{1}{\gamma\beta_2^2}\right)\gamma\kappa} \geq \frac{\left[2K\left(\Gamma - \frac{1}{\gamma\beta_2^2}\right) + \gamma\kappa\right]^2}{2K\left(\Gamma - \frac{1}{\gamma\beta_2^2}\right)\gamma\kappa} \geq 4 \quad , \tag{D.13}$$

where we have used $\gamma, \kappa, K, \Gamma \geq 0$ and $\Gamma - 1/(\gamma\beta_2^2) \geq 0$. Therefore, if the parameter β_1 is chosen such that α is negligible, the gel can never be in the oscillatory regime $\tau_d > \tau/4$ described in Section 3.3.

A finite value of β_1 implies a dependence of the shear stress on the molecular field H_{ij}. If we assume that the main contribution to the shear stress comes from the viscous and elastic stresses and other contributions are negligible, one would set $\beta_1 = 0$. In this case, it is no longer possible for α to be arbitrarily small. Indeed, due to the positive semi-definiteness of Onsager coefficient matrix $\Gamma - 1/(\gamma\beta_2) \geq 0$, the coefficient Γ cannot be arbitrarily small. For $\Gamma < 1/(\gamma\beta_2^2)$ the time-scale τ would become negative and the thermodynamic equilibrium state would become unstable. Moreover, a lower limit to the prefactor α is given by

$$\alpha > \frac{\tau_d}{\tau} \quad . \tag{D.14}$$

Other possible choices of parameters which would allow neglecting the term involving the shear strain are $K \to 0$ and $\gamma\kappa \to \infty$. However, both choices inevitably remove a term in Eq. (D.12), in such a way that the form of Eq. (3.3) can not be reproduced. Therefore, a passive gel with only viscous and elastic stresses can reproduce Eq. (3.3) only with an additional term involving time derivative of the tensor Q_{ij}.

D.1.2 Active gel

If the system is provided with a reservoir of ATP molecules to keep it out of equilibrium, such that the difference of chemical potential $\Delta\mu$ is not 0, the equation for R_{ij} in the case $\beta_1 = 0$ reads

$$\left(1 + \frac{1}{\gamma\kappa - \theta\Delta\mu}\frac{\mathrm{D}}{\mathrm{D}t}\right)R_{ij} = \left(2K\Gamma - \overline{\psi}\Delta\mu - \left(\frac{2K}{\beta_2} - \overline{\theta}\Delta\mu\right)\frac{\kappa/\beta_2 - \psi\Delta\mu}{\gamma\kappa - \theta\Delta\mu}\right)Q_{ij}$$
$$+ \frac{2K\Gamma - \overline{\psi}\Delta\mu}{\gamma\kappa - \theta\Delta\mu}\frac{\mathrm{D}}{\mathrm{D}t}Q_{ij} \tag{D.15}$$

and we identify

$$\tau_d = \frac{1}{\gamma\kappa - \theta\Delta\mu} \tag{D.16}$$

$$\tau = \frac{1}{\left(2K\Gamma - \overline{\psi}\Delta\mu - \left(\frac{2K}{\beta_2} - \overline{\theta}\Delta\mu\right)\frac{\kappa/\beta_2 - \psi\Delta\mu}{\gamma\kappa - \theta\Delta\mu}\right)} \quad . \tag{D.17}$$

In this case, the term involving the derivative of shear strain Q_{ij} becomes small when $\left|(2K\Gamma - \overline{\psi}\Delta\mu)/(\gamma\kappa - \theta\Delta\mu)\right| \ll 1$. The stability in this limit can still be maintained if the factor $(2K/\beta_2 - \overline{\theta}\Delta\mu)(\kappa/\beta_2 - \psi\Delta\mu)$ is negative. This is possible because the signs of the active terms $\psi\Delta\mu$ and $\overline{\theta}\Delta\mu$ are not constrained. Thus, an active nematic gel close to equilibrium can be described by Eq. (3.3), even without a specific coupling of the molecular field to the shear stress.

Appendix E

Autonomous convergent extension

This appendix was published in our recent publication [66]. It contains derivation of the results presented in Chapter 3 and we reproduce it here with minor modifications.

Here we derive the result discussed in the Section 3.5. We consider a rectangular homogeneous tissue with length l and width h. The cell polarity nematic q_{ij} is constant and oriented along x-axis such that $q_{xx} = 1, q_{xy} = 0$. We assume that for $t < 0$, the tissue is at rest, not subjected to active processes, that cells are isotropic and that there is no stress in the elastic boundary springs. At $t = 0$, active processes described by ζ and λ are turned on and remain constant for $t > 0$. The tissue is constrained in space by the boundary springs that provide resistance to the changes in tissue length and width. We describe the external elastic response to the tissue deformations by a Hooke's law

$$
\begin{aligned}
\sigma_{xx} &= -k_x L \\
\sigma_{yy} &= -k_y H \quad ,
\end{aligned}
\tag{E.1}
$$

where $L = \ln\left(l/l_0\right)$ and $H = \ln\left(h/h_0\right)$ are natural strain variables of the tissue and l_0, h_0 are tissue length and width at zero stress. For negative times, the tissue is stress free and thus $L(t < 0) = H(t < 0) = 0$. Since tissue is homogeneously flowing, boundary conditions Eq. (E.1) determine the stress in the whole tissue.

Since the shape of the tissue is a rectangle, the velocity gradient tensor has only diagonal components

$$
\begin{aligned}
v_{xx} &= \partial_t L \\
v_{yy} &= \partial_t H \quad .
\end{aligned}
\tag{E.2}
$$

We assume that the tissue pressure can be described by Eq. (2.21) without memory

$$P = -\overline{K} \ln \frac{a}{a_0} \quad , \tag{E.3}$$

where a and a_0 are the average cell area and the preferred cell area, as defined in Chapter 2.

Combining Eq. (E.1) and Eq. (E.2) with Eq. (E.3) and tissue area change rate decomposition Eq. (2.13), we obtain a relation between L and H from the isotropic flow component

$$\left(1 + \frac{k_x}{2\overline{K}}\right) \partial_t L + \left(1 + \frac{k_y}{2\overline{K}}\right) \partial_t H = 0 \quad , \tag{E.4}$$

where we have used the fact that in the absence of cell division and extrusion, $(da/dt)/a = (dA/dt)/A$ with A being the area of the tissue. Using the constitutive relation for the shear stress Eq. (3.6), the constitutive equation for the shear due to topological rearrangements Eq. (3.3), and the shear flow decomposition Eq. (2.16), we obtain a second relation between L and H

$$\left(1 + \frac{k_x}{2K}\right)\left(1 + \tau_d \partial_t\right)\partial_t L + \frac{k_x}{2K\tau}L - \left(1 + \frac{k_y}{2K}\right)\left(1 + \tau_d \partial_t\right)\partial_t H - \frac{k_y}{2K\tau}H = 2\gamma \tag{E.5}$$

where $\gamma = -\zeta/(2K\tau) + \lambda$. Integrating Eq. (E.4) from an arbitrary lower bound $t < 0$ yields

$$\left(1 + \frac{k_x}{2\overline{K}}\right) L + \left(1 + \frac{k_y}{2\overline{K}}\right) H = 0 \quad . \tag{E.6}$$

We now express H in terms of L in Eq. (E.5) and we obtain the second order equation

$$\tau_d \partial_t^2 L + \partial_t L + \frac{\nu}{\tau\mu}L = \frac{2\gamma}{\mu} \quad , \tag{E.7}$$

where

$$\mu = 1 + \frac{k_x}{2K} + \left(1 + \frac{k_y}{2K}\right)\frac{1 + \frac{k_x}{2\overline{K}}}{1 + \frac{k_y}{2\overline{K}}} \tag{E.8}$$

$$\nu = \frac{k_x}{2K} + \frac{k_y}{2K}\frac{1+\frac{k_x}{2K}}{1+\frac{k_y}{2K}} \quad . \tag{E.9}$$

This can be solved for

$$
\begin{aligned}
L(t) &= \frac{2\tau}{\nu}\gamma\left[1 - \left(1 - \frac{\nu L(0)}{2\tau\gamma}\right)e^{-t/(2\tau_d)}\left(\frac{1}{s}\sin\frac{s}{2\tau_d}t + \cos\frac{s}{2\tau_d}t\right)\right] \\
&\quad + \partial_t L(0)e^{-t/(2\tau_d)}\frac{\sin\frac{s}{2\tau_d}t}{s/(2\tau_d)} \quad ,
\end{aligned}
\tag{E.10}
$$

where $L(0)$ and $\partial_t L(0)$ are initial conditions, and

$$s^2 = \frac{4\tau_d\nu}{\tau\mu} - 1. \tag{E.11}$$

The parameter s^2 is positive only for high enough values of the memory time-scale τ_d. When s^2 becomes negative, the solution is equivalent in form to Eq. (E.10), with trigonometric functions replaced by their hyperbolic counterparts and s^2 replaced with $-s^2$.

We now determine the initial conditions for an experimental setting in which the tissue is initially at rest, cells in the tissue are not elongated, external elastic connections are not under tension, and there is no tissue polarity. At $t = 0$ the polarity is activated on a time-scale much shorter than τ and τ_d, so that we can treat the activation as instantaneous. First, considering Eq. (3.3) we can conclude that $R_{xx}(0^+) = 0$. Then, using Eqs. (E.1), (E.2), (E.4), (2.16) and (3.6) we can show that for $t \to 0^+$

$$
\begin{aligned}
\frac{1}{2}\left(1 + \frac{1+\frac{k_x}{2K}}{1+\frac{k_y}{2K}}\right)\partial_t L(t) &= \partial_t Q_{xx}(t) \\
&= -\frac{1}{2}\left[\frac{k_x}{2K} + \frac{k_y}{2K}\frac{1+\frac{k_x}{2K}}{1+\frac{k_y}{2K}}\right]\partial_t L(t) - \frac{\zeta}{2K}\partial_t q_{xx}(t) \quad .
\end{aligned}
\tag{E.12}
$$

Then, using $\partial_t q_{xx} = \delta(t)$ and integrating over a small finite time interval around $t = 0$,

we obtain the initial conditions

$$L(0^+) = -\frac{\zeta}{\mu K}$$

$$\partial_t L(0^+) = 0 \quad . \tag{E.13}$$

When the elastic connections around the tissue are isotropic ($k_x = k_y$), one obtains from Eqs. (E.6), (E.8) and (E.9)

$$H(t) = -L(t) \tag{E.14}$$

$$\mu = 2\left(1 + \frac{k}{2K}\right) \tag{E.15}$$

$$\nu = \frac{k}{K} \quad . \tag{E.16}$$

Since $L(t) + H(t) = 0$, the tissue area is constant. Therefore, area changes arise only when the surrounding material is anisotropic. In Chapter 3 we are interested in the tissue shear flows and thus we only discuss the case $k_x = k_y = k$. Using these relations, the initial conditions discussed above and Eq. (E.10), we obtain Eq. (3.24) in the Chapter 3.

Finally, we note that in the limit $\tau_d \to 0$, Eq. (E.10) describes a simple exponential relaxation of the tissue length:

$$L(t) = \frac{2\tau\gamma}{\nu}\left[1 - \left(1 - \frac{\nu L(0)}{2\tau\gamma}\right)e^{-\frac{\nu}{\mu\tau}t}\right] \quad . \tag{E.17}$$

with a characteristic relaxation time-scale equal to $\tau(1 + 2K/k)$ for isotropic external springs. It differs from the Maxwell time-scale of the tissue τ by a factor describing the competition of internal and external elasticities.

Appendix F

Rectangle dimensions

Here we describe how the effective height and length of the wing blade and hinge regions is determined from the experimental data. A reasonable definition of region dimensions should preserve the region area A^{region}

$$L^{\text{region}} h^{\text{region}} = A^{\text{region}} \quad . \tag{F.1}$$

A second condition we impose on the effective region dimensions is that their ratio should reflect the region anisotropy along the long axis of the wing. To this end, we consider the moment of inertia tensor of the region

$$M_{ij} = \sum_{k \in \text{cells}} a_k \left(r_i^{(k)} - r_i^{CM} \right) \left(r_j^{(k)} - r_j^{CM} \right) \quad , \tag{F.2}$$

where a_k and r_i are the area and the position vector of cell k, respectively and r_i^{CM} is the position of the region center of area

$$r_i^{CM} = \frac{1}{A^{\text{region}}} \sum_{k \in \text{cells}} a_k r_i^{(k)} \quad . \tag{F.3}$$

Now, the elongation of the region can be represented by a tensor Q_{ij}^r defined to satisfy

$$M_{ij} = e^{Q_{ij}^r} \quad . \tag{F.4}$$

The region elongation along the x axis is then Q_{xx}^r and we impose on the region dimensions the condition

$$\frac{L^{\text{region}}}{h^{\text{region}}} = e^{Q_{xx}^r} \quad .$$

(F.5)

Using Eq. (F.1) and Eq. (F.5) one could determine the effective dimension of the tissue regions at any given timepoint. However, region dimensions defined in this way would only satisfy Eq. (6.1) and Eq. (6.2) if the tissue sheared homogeneously in space along a constant axis. Although this approximation holds reasonably well for the blade tracked region we cannot use it for the whole visible hinge and blade regions. Also, parts of the wing tissue flow in and out of the field of view. To avoid these problems we instead define height and length as integrals of average velocity gradients calculated from particle image velocimetry (PIV) measurements performed by our collaborators [54]

$$L^{\text{region}} = \beta_L^{\text{region}} \exp\left(\int_{t_0}^{t} v_{xx} dt\right)$$

(F.6)

$$h^{\text{region}} = \beta_h^{\text{region}} \exp\left(\int_{t_0}^{t} v_{yy} dt\right) \quad .$$

(F.7)

so that they exactly fulfill Eqs. (6.1)-(6.2). The integration constants β_L^{region} and β_h^{region} are determined by comparison of the two definitions in a time interval in which no inflow of tissue is visible.

Appendix G

Center of the wing disc pouch and the additional correlation term

G.1 Definition of the wing disc pouch center

We define the center of the wing disc pouch to be the crossing point of the DV compartment boundary (green cells in the Fig. 7.1 A) and the stripe of small cells oriented in the dorso-ventral direction (see Fig. 7.1 B). The cell area as a function of position along the DV boundary in the wing disc pouch is shown in Fig. G.1 at four different time points. The well-defined minimum of the cell area does not change its position in time. This is the position at the DV boundary that we use as the center point of the wing pouch.

G.2 Correlation between cell elongation and cell movement contributes to the average radial shear flow

Here we show how the new correlation terms S_{ij} arises in the triangle method. We consider a tissue that translates over time interval Δt but does not change otherwise. The tissue is triangulated by connecting the neighboring cell centers (see [55] for details of the triangle method). Initially, the angle of a triangle k with with respect to a center point is φ^k (blue triangle in Fig. G.1 B). During the translation by $\Delta \boldsymbol{r} = \boldsymbol{r}(t+\Delta t) - \boldsymbol{r}(t)$ the radial angle of the triangles changes by a small angle $\Delta \varphi^k$. Therefore, the radial
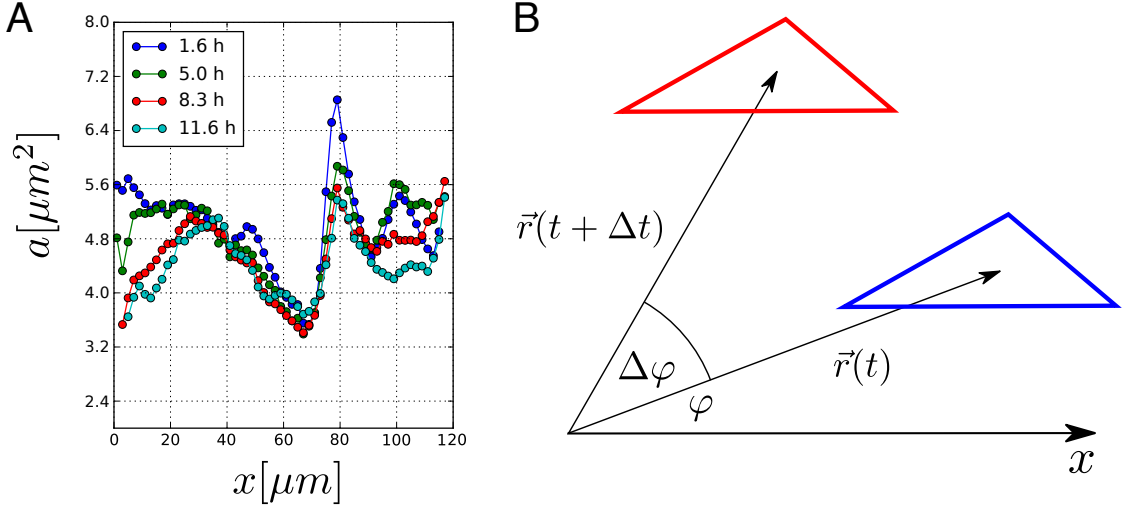
A

B

Figure G.1: A) Cell area as a function of position along the DV compartment boundary in the wing disc pouch at 4 different time points. B) Triangle is translated by $\Delta \boldsymbol{r} = \boldsymbol{r}(t+\Delta t) - \boldsymbol{r}(t)$. Although the cell elongation did not change during the translation the radial component of cell elongation is changed due to the change of radial direction by $\Delta \varphi$.

component of triangle elongation tensor q_{ij}^k changes by

$$\Delta q_{ij}^k = -2\epsilon_{ik} q_{kj}^k \Delta \varphi^k \quad . \tag{G.1}$$

However, since all triangles are only translating, there is no shear flow anywhere in the tissue. Therefore, the average radial shear flow also vanishes and an additional term is necessary to account for the change in the average radial cell elongation in a translating tissue

$$\tilde{v}_{IJ} = 0 = \frac{\Delta Q_{IJ}}{\Delta t} + S_{IJ} \quad . \tag{G.2}$$

Therefore, the new correlation term is given by

$$S_{IJ} = \frac{1}{\Delta t} \left\langle 2\epsilon_{ik} q_{kj} \Delta \varphi \right\rangle \quad . \tag{G.3}$$

G.2 Correlation between cell elongation and cell movement contributes to the average
radial shear flow
121

We now give the expression for DQ_{IJ}/Dt used in Eq. (7.3)

$$\frac{DQ_{RR}}{Dt} = \frac{\Delta Q_{RR}}{\Delta t} - 2\left(C\langle\omega\rangle + (1-C)\frac{\Delta\Phi}{\Delta t}\right)Q_{R\Phi} \tag{G.4}$$

$$\frac{DQ_{R\Phi}}{Dt} = \frac{\Delta Q_{R\Phi}}{\Delta t} + 2\left(C\langle\omega\rangle + (1-C)\frac{\Delta\Phi}{\Delta t}\right)Q_{RR} \quad . \tag{G.5}$$

Here, Q_{RR} and $Q_{R\Phi}$ are radial averages as defined in Eq. (7.1) and Eq. (7.2) and

$$C = \frac{\tanh\left(2\sqrt{Q_{RR}^2 + Q_{RT}^2}\right)}{2\sqrt{Q_{RR}^2 + Q_{RT}^2}}, \tag{G.6}$$

$$-\omega\epsilon_{ij} = \frac{1}{2}\left(\partial_i v_j - \partial_j v_i\right), \tag{G.7}$$

$$\tan\left(2\Phi\right) = \frac{Q_{R\Phi}}{Q_{RR}} \quad . \tag{G.8}$$

This is expression is equivalent to the expression for the coarse-grained corotational derivative of cell elongation tensor in [55] with the difference that cell elongation averages are defined by Eq. (7.1) and Eq. (7.2).

Other cellular contributions in Eq. (7.3) are simply the radial averages, defined by Eq. (7.1) and Eq. (7.2).

Appendix H

Mathematical identities used in Chapter 7

H.1 Simplification of the expression for pressure in the circular tissue

Here we simplify the last term on the right-hand side of Eq. (7.30). To this end, we define it to be equal to some function $f(r)$

$$f(r) = \frac{1}{r^2} \int\limits_0^r r'^2 \partial_{r'} g(r') dr' - 2 \int\limits_r^R \frac{1}{r'^3} \int\limits_0^{r'} r''^2 \partial_{r''} g(r'') dr'' dr' \quad . \tag{H.1}$$

We then perform partial integrations to find

$$f(r) = g(r) - \frac{2}{r^2} \left[\int\limits_0^r r' g(r') dr' + r^2 \int\limits_r^R \frac{1}{r'} \left[g(r') - \frac{2}{r'^2} \int\limits_0^{r'} r'' g(r'') dr'' \right] dr' \right] \quad . \tag{H.2}$$

Now we define a function

$$\Phi(r) = \int\limits_0^r r' g(r') dr' + r^2 \int\limits_r^R \frac{1}{r'} \left[g(r') - \frac{2}{r'^2} \int\limits_0^{r'} r'' g(r'') dr'' \right] dr' \quad , \tag{H.3}$$

so that

$$f(r) = g(r) - \frac{2}{r^2}\Phi(r) \quad . \tag{H.4}$$

Taking a derivative of $\Phi(r)$ over r we find

$$\Phi'(r) = \frac{2}{r}\Phi(r) \quad . \tag{H.5}$$

The solution of this differential equation is

$$\Phi(r) = \Phi(R)\frac{r^2}{R^2} \quad , \tag{H.6}$$

and the value of the integration constant can be found from Eq. (H.3) to be

$$\Phi(R) = \int_0^R rg(r)dr \quad . \tag{H.7}$$

Therefore,

$$f(r) = g(r) - \frac{2}{R^2}\int_0^R rg(r)dr \quad . \tag{H.8}$$

We can recognize the second term on the right-hand side to be the average $\langle g(r)\rangle$ of $g(r)$ in the circular tissue. Therefore $f(r)$ is a measure of fluctuation of $g(r)$ around its mean value. We use Eq. (H.8) to simplify Eq. (7.30).

H.2 The active shear coefficient does not contribute to the average pressure in a circular tissue

Here, we prove that for an arbitrary continuous function $f(r)$

$$\int_0^R r\left(f(r) - 2\int_r^R \frac{f(r')}{r'}dr'\right)dr = 0 \quad . \tag{H.9}$$

We use this identity in Eq. (7.37) to show that the influence of the active shear coefficient on the pressure vanishes on average, for an arbitrary continuous active shear coefficient $\gamma(r)$.

We first expand the function $f(r)$ in a Fourier sine series on $0 < r < R$

$$f(r) = \sum_n c_n \sin\left(\frac{n\pi r}{R}\right) \quad , \tag{H.10}$$

where c_n are defined to be

$$c_n = \frac{2}{R} \int_0^R f(r) \sin\left(\frac{n\pi r}{R}\right) \quad . \tag{H.11}$$

Now we prove the Eq. (H.9) by directly evaluating the expression on left-hand side

$$\int_0^R r \left(f(r) - 2 \int_r^R \frac{f(r')}{r'} dr' \right) dr =$$

$$\sum_n c_n \int_0^R r \sin\left(\frac{n\pi r}{R}\right) dr - 2 \sum_n c_n \int_0^R r \int_r^R \frac{\sin\left(\frac{n\pi r'}{R}\right)}{r'} dr' dr =$$

$$\sum_n c_n \sum_k \frac{\left(\frac{n\pi}{R}\right)^{2k+1}}{(2k+1)!} \int_0^R r^{2k+2} dr - 2 \sum_n c_n \sum_k \frac{\left(\frac{n\pi}{R}\right)^{2k+1}}{(2k+1)!} \int_0^R r \int_r^R r'^{2k} dr' dr =$$

$$\sum_n c_n \sum_k \frac{\left(\frac{n\pi}{R}\right)^{2k+1}}{(2k+1)!} \frac{R^{2k+3}}{2k+3} - 2 \sum_n c_n \sum_k \frac{\left(\frac{n\pi}{R}\right)^{2k+1}}{(2k+1)!} \int_0^R r \frac{1}{2k+1} \left(R^{2k+1} - r^{2k+1} \right) dr =$$

$$\sum_n c_n \sum_k \frac{\left(\frac{n\pi}{R}\right)^{2k+1}}{(2k+1)!} \frac{R^{2k+3}}{2k+3} - 2 \sum_n c_n \sum_k \frac{\left(\frac{n\pi}{R}\right)^{2k+1}}{(2k+1)!} \frac{R^{2k+3}}{2(2k+3)} = 0 \quad . \tag{H.12}$$

Here, we have used Taylor series of the sine function.

Bibliography

[1] *OpenStax, Anatomy & Physiology*. OpenStax CNX, Dec 15, 2016. eprint: `http: //cnx.org/contents/14fb4ad7-39a1-4eee-ab6e-3ef2482e3e22@8.47.` (cited on page 2).

[2] C. G. Vasquez and A. C. Martin. "Force transmission in epithelial tissues". *Developmental Dynamics* 245.3 (2016), 361–371 (cited on page 2).

[3] L. Larue, M. Ohsugi, J. Hirchenhain, and R. Kemler. "E-cadherin null mutant embryos fail to form a trophectoderm epithelium". *Proceedings of the National Academy of Sciences* 91.17 (1994), 8263–8267. eprint: `http://www.pnas.org/ content/91/17/8263.full.pdf` (cited on page 2).

[4] U. Tepass, E. Gruszynski-DeFeo, T. A. Haag, L. Omatyar, T. Török, and V. Hartenstein. "shotgun encodes Drosophila E-cadherin and is preferentially required during cell rearrangement in the neurectoderm and other morphogenetically active epithelia." *Genes & Development* 10.6 (1996), 672–685. eprint: `http: //genesdev.cshlp.org/content/10/6/672.full.pdf+html` (cited on page 2).

[5] G. Salbreux, G. Charras, and E. Paluch. "Actin cortex mechanics and cellular morphogenesis". *Trends in cell biology* 22.10 (2012), 536–545 (cited on page 4).

[6] K. Kruse, J.-F. Joanny, F. Jülicher, J. Prost, and K. Sekimoto. "Generic theory of active polar gels: a paradigm for cytoskeletal dynamics". *The European Physical Journal E* 16.1 (2005), 5–16 (cited on pages 4, 7, 21).

[7] J. Joanny and J. Prost. "Active gels as a description of the actin-myosin cytoskeleton". *HFSP Journal* 3.2 (2009), 94–104. eprint: `http://www.tandfonline. com/doi/pdf/10.2976/1.3054712` (cited on page 4).

[8] A. G. Clark, O. Wartlick, G. Salbreux, and E. K. Paluch. "Stresses at the Cell Surface during Animal Cell Morphogenesis". *Current Biology* 24.10 (2014), R484–R494 (cited on page 4).

[9] T. Hiraiwa and G. Salbreux. "Role of Turnover in Active Stress Generation in a Filament Network". *Physical Review Letters* 116 (18 2016), 188101 (cited on page 4).

[10] R. Farhadifar, J.-C. Röper, B. Aigouy, S. Eaton, and F. Jülicher. "The influence of cell mechanics, cell-cell interactions, and proliferation on epithelial packing". *Current Biology* 17.24 (2007), 2095–2104 (cited on page 4).

[11] H. Honda, R. Kodama, T. Takeuchi, H. Yamanaka, K. Watanabe, and G. Eguchi. "Cell behaviour in a polygonal cell sheet". *Development* 83.Supplement (1984), 313–327 (cited on page 4).

[12] F. Graner and J. A. Glazier. "Simulation of biological cell sorting using a two-dimensional extended Potts model". *Physical review letters* 69.13 (1992), 2013 (cited on page 4).

[13] D. Drasdo, R. Kree, and J. S. McCaskill. "Monte Carlo approach to tissue-cell populations". *Physical Review E* 52.6 (1995), 6635 (cited on page 4).

[14] T. Nagai and H. Honda. "A dynamic cell model for the formation of epithelial tissues". *Philosophical Magazine Part B* 81.7 (2001), 699–719. eprint: `http://dx.doi.org/10.1080/13642810108205772` (cited on page 4).

[15] J. Moreira and A. Deutsch. "Cellular automaton models of tumor development: a critical review". *Advances in Complex Systems* 05.02n03 (2002), 247–267. eprint: `http://www.worldscientific.com/doi/pdf/10.1142/S0219525902000572` (cited on page 4).

[16] L. Hufnagel, A. A. Teleman, H. Rouault, S. M. Cohen, and B. I. Shraiman. "On the mechanism of wing size determination in fly development". *Proceedings of the National Academy of Sciences* 104.10 (2007), 3835–3840. eprint: `http://www.pnas.org/content/104/10/3835.full.pdf` (cited on pages 4, 53, 77).

[17]   T. Bittig, O. Wartlick, A. Kicheva, M. González-Gaitán, and F. Jülicher. "Dynamics of anisotropic tissue growth". *New Journal of Physics* 10.6 (2008), 063001 (cited on pages 4–5, 7).

[18]   H. Byrne and D. Drasdo. "Individual-based and continuum models of growing cell populations: a comparison". *Journal of Mathematical Biology* 58.4 (2008), 657 (cited on page 4).

[19]   P. Pathmanathan, J. Cooper, A. Fletcher, G. Mirams, P. Murray, J. Osborne, J. Pitt-Francis, A. Walter, and S. J. Chapman. "A computational study of discrete mechanical tissue models". *Physical Biology* 6.3 (2009), 036001 (cited on page 4).

[20]   K. P. Landsberg, R. Farhadifar, J. Ranft, D. Umetsu, T. J. Widmann, T. Bittig, A. Said, F. Jülicher, and C. Dahmann. "Increased Cell Bond Tension Governs Cell Sorting at the Drosophila Anteroposterior Compartment Boundary". *Current Biology* 19.22 (2009), 1950–1955 (cited on page 4).

[21]   M. Basan, J. Prost, J.-F. Joanny, and J. Elgeti. "Dissipative particle dynamics simulations for biological tissues: rheology and competition". *Physical Biology* 8.2 (2011), 026014 (cited on page 4).

[22]   O. Wartlick, P. Mumcu, A. Kicheva, T. Bittig, C. Seum, F. Jülicher, and M. González-Gaitán. "Dynamics of Dpp Signaling and Proliferation Control". *Science* 331.6021 (2011), 1154–1159. eprint: `http://science.sciencemag.org/content/331/6021/1154.full.pdf` (cited on page 4).

[23]   G. Salbreux, L. K. Barthel, P. A. Raymond, and D. K. Lubensky. "Coupling mechanical deformations and planar cell polarity to create regular patterns in the zebrafish retina". *PLoS Computational Biology* 8.8 (2012), e1002618 (cited on page 4).

[24]   D. Bi, X. Yang, M. C. Marchetti, and M. L. Manning. "Motility-Driven Glass and Jamming Transitions in Biological Tissues". *Physical Review X* 6 (2 2016), 021011 (cited on page 4).

[25]   M. Osterfield, X. Du, T. Schüpbach, E. Wieschaus, and S. Y. Shvartsman. "Three-dimensional epithelial morphogenesis in the developing Drosophila egg". *Developmental cell* 24.4 (2013), 400–410 (cited on page 4).

[26]   N. Murisic, V. Hakim, I. G. Kevrekidis, S. Y. Shvartsman, and B. Audoly. "From discrete to continuum models of three-dimensional deformations in epithelial sheets". *Biophysical journal* 109.1 (2015), 154–163 (cited on page 4).

[27]   B. Monier, M. Gettings, G. Gay, T. Mangeat, S. Schott, A. Guarner, and M. Suzanne. "Apico-basal forces exerted by apoptotic cells drive epithelium folding". *Nature* 518.7538 (2015), 245–248 (cited on page 4).

[28]   C. Bielmeier, S. Alt, V. Weichselberger, M. La Fortezza, H. Harz, F. Jülicher, G. Salbreux, and A.-K. Classen. "Interface contractility between differently fated cells drives cell elimination and cyst formation". *Current Biology* 26.5 (2016), 563–574 (cited on page 4).

[29]   G. M. Odell, G. Oster, P. Alberch, and B. Burnside. "The mechanical basis of morphogenesis: I. Epithelial folding and invagination". *Developmental biology* 85.2 (1981), 446–462 (cited on page 4).

[30]   A. Hočevar Brezavšček, M. Rauzi, M. Leptin, and P. Ziherl. "A model of epithelial invagination driven by collective mechanics of identical cells". *Biophysical Journal* 103.5 (2012), 1069–1077 (cited on page 4).

[31]   M. Rauzi, U. Krzic, T. E. Saunders, M. Krajnc, P. Ziherl, L. Hufnagel, and M. Leptin. "Embryo-scale tissue mechanics during Drosophila gastrulation movements". *Nature communications* 6 (2015) (cited on page 4).

[32]   N. Štorgel, M. Krajnc, P. Mrak, J. Štrus, and P. Ziherl. "Quantitative Morphology of Epithelial Folds". *Biophysical Journal* 110.1 (2016), 269–277 (cited on page 4).

[33]   R. A. Alexander, M. A. J. Chaplain, and K. A. Rejniak. *Single-Cell-Based Models in Biology and Medicine.* Birkhäuser Basel, 2007 (cited on page 4).

[34]   R. Smallwood. "Computational modeling of epithelial tissues". *Wiley Interdisciplinary Reviews: Systems Biology and Medicine* 1.2 (2009), 191–201 (cited on page 4).

[35]   A. G. Fletcher, M. Osterfield, R. E. Baker, and S. Y. Shvartsman. "Vertex models of epithelial morphogenesis". *Biophysical Journal* 106.11 (2014), 2291–2304 (cited on page 4).

[36]   M. Aliee, J.-C. Röper, K. P. Landsberg, C. Pentzold, T. J. Widmann, F. Jülicher, and C. Dahmann. "Physical Mechanisms Shaping the Drosophila Dorsoventral Compartment Boundary". *Current Biology* 22.11 (2012), 967–976 (cited on page 4).

[37]   B. Aigouy, R. Farhadifar, D. B. Staple, A. Sagner, J.-C. Röper, F. Jülicher, and S. Eaton. "Cell flow reorients the axis of planar polarity in the wing epithelium of Drosophila". *Cell* 142.5 (2010), 773–786 (cited on pages 4, 7, 17).

[38]   T. Aegerter-Wilmsen, M. B. Heimlicher, A. C. Smith, P. B. de Reuille, R. S. Smith, C. M. Aegerter, and K. Basler. "Integrating force-sensing and signaling pathways in a model for the regulation of wing imaginal disc size". *Development* 139.17 (2012), 3221–3231. eprint: `http://dev.biologists.org/content/139/17/3221.full.pdf` (cited on pages 4, 77).

[39]   D. B. Staple, R. Farhadifar, B. Röper J. -C.and Aigouy, S. Eaton, and F. Jülicher. "Mechanics and remodelling of cell packings in epithelia". *The European Physical Journal E* 33.2 (2010), 117–127 (cited on page 4).

[40]   L. Wolpert, R. Beddington, T. Jessell, P. Lawrence, E. Meyerowitz, and J. Smith. *Principles of development.* Oxford University Press, 2002 (cited on pages 5, 9–11).

[41]   P. Marmottant, A. Mgharbel, J. Käfer, B. Audren, J.-P. Rieu, J.-C. Vial, B. Van Der Sanden, A. F. M. Marée, F. Graner, and H. Delanoë-Ayari. "The role of fluctuations and stress on the effective viscosity of cell aggregates". *Proceedings of the National Academy of Sciences* 106.41 (2009), 17271–17275 (cited on pages 5, 93).

[42]   J. Ranft, M. Basan, J. Elgeti, J.-F. Joanny, J. Prost, and F. Jülicher. "Fluidization of tissues by cell division and apoptosis". *Proceedings of the National Academy of Sciences* 107.49 (2010), 20863–20868 (cited on pages 5, 53, 77, 93).

[43]   X. Serra-Picamal, V. Conte, R. Vincent, E. Anon, D. T. Tambe, E. Bazellieres, J. P. Butler, J. J. Fredberg, and X. Trepat. "Mechanical waves during tissue expansion". *Nature Physics* 8.8 (2012), 628–634 (cited on page 5).

[44]   M. H. Köpf and L. M. Pismen. "A continuum model of epithelial spreading". *Soft Matter* 9.14 (2013), 3727–3734 (cited on pages 5, 7).

[45]   C. Blanch-Mercader, J. Casademunt, and J. F. Joanny. "Morphology and growth of polarized tissues". *The European Physical Journal E* 37.5 (2014), 1–11 (cited on page 5).

[46]   S. Tlili, C. Gay, F. Graner, P. Marcq, F. Molino, and P. Saramito. "Colloquium: Mechanical formalisms for tissue dynamics". *The European Physical Journal E* 38.5 (2015), 1–31 (cited on pages 5, 7, 93).

[47]   S. Banerjee, K. J. C. Utuje, and M. C. Marchetti. "Propagating Stress Waves During Epithelial Expansion". *Physical Review Letters* 114 (22 2015), 228101 (cited on pages 5, 7).

[48]   P. Recho, J. Ranft, and P. Marcq. "One-dimensional collective migration of a proliferating cell monolayer". *Soft matter* 12.8 (2016), 2381–2391 (cited on page 5).

[49]   W.-T. Yeh and H.-Y. Chen. "Hydrodynamics of stratified epithelium: steady state and linearized dynamics". *Physical Review E* 93.5 (2016), 052421 (cited on page 5).

[50]   J. Notbohm, S. Banerjee, K. J. C. Utuje, B. Gweon, H. Jang, Y. Park, J. Shin, J. P. Butler, J. J. Fredberg, and M. C. Marchetti. "Cellular contraction and polarization drive collective cellular motion". *Biophysical Journal* 110.12 (2016), 2729–2738 (cited on pages 5–7).

[51]   L. Onsager. "Reciprocal Relations in Irreversible Processes. I." *Physical Review* 37 (4 1931), 405–426 (cited on page 6).

[52]   M. Merkel, A. Sagner, F. S. Gruber, R. Etournay, C. Blasse, E. Myers, S. Eaton, and F. Jülicher. "The balance of prickle/spiny-legs isoforms controls the amount of coupling between core and fat PCP systems". *Current Biology* 24.18 (2014), 2111–2123 (cited on page 7).

[53]   A. C. Callan-Jones and F. Jülicher. "Hydrodynamics of active permeating gels". *New Journal of Physics* 13.9 (2011), 093027 (cited on pages 7, 38, 107, 109).

[54] R. Etournay et al. "Interplay of cell dynamics and epithelial tension during morphogenesis of the Drosophila pupal wing". *eLife* 4 (2015), e07090 (cited on pages 8, 12, 20, 25, 28, 30, 32–33, 53–55, 63, 70, 73–74, 93, 101–104, 118).

[55] M. Merkel, R. Etournay, M. Popović, G. Salbreux, S. Eaton, and F. Jülicher. "Triangles bridge the scales: Quantifying cellular contributions to tissue deformation". *Physical Review E* 95 (3 2017), 032401 (cited on pages 8, 13, 16, 18, 25, 27, 79–80, 91, 93, 99, 119, 121).

[56] B. Guirao, S. Rigaud, F. Bosveld, A. Bailles, J. Lopez-Gay, S. Ishihara, K. Sugimura, F. Graner, and Y. Bellaïche. "Unified quantitative characterization of epithelial tissue development". *eLife* 5 (2015), e08519 (cited on pages 8–9).

[57] G. B. Blanchard, A. J. Kabla, N. L. Schultz, L. C. Butler, B. Sanson, N. Gorfinkiel, L. Mahadevan, and R. J. Adams. "Tissue tectonics: morphogenetic strain rates, cell shape change and intercalation". *Nature methods* 6.6 (2009), 458–464 (cited on page 7).

[58] M. Asipauskas, M. Aubouy, J. A. Glazier, F. Graner, and Y. Jiang. "A texture tensor to quantify deformations: the example of two-dimensional flowing foams". *Granular Matter* 5.2 (2003), 71–74 (cited on page 9).

[59] T. H. Morgan. "Sex limited inheritance in Drosophila". *Science* 32.812 (1910), 120–122. eprint: `http://science.sciencemag.org/content/32/812/120.full.pdf` (cited on page 9).

[60] M. D. Adams, S. E. Celniker, R. A. Holt, C. A. Evans, J. D. Gocayne, P. G. Amanatides, S. E. Scherer, P. W. Li, R. A. Hoskins, R. F. Galle, et al. "The genome sequence of Drosophila melanogaster". *Science* 287.5461 (2000), 2185–2195 (cited on page 9).

[61] E. Bier. "Drosophila, the golden bug, emerges as a tool for human genetics". *Nature Reviews Genetics* 6.1 (2005), 9–23 (cited on page 9).

[62] J. V. Beira and R. Paro. "The legacy of Drosophila imaginal discs". *Chromosoma* 125.4 (2016), 573–592 (cited on page 10).

[63] G. Morata. "How Drosophila appendages develop". *Nature Reviews Molecular Cell Biology* 2.2 (2001), 89–97 (cited on page 11).

[64] C. Kiecker and A. Lumsden. "Compartments and their boundaries in vertebrate brain development". *Nature Reviews Neuroscience* 6.7 (2005), 553–564 (cited on page 11).

[65] M. D. de la Loza and B. Thompson. "Forces shaping the Drosophila wing". *Mechanisms of Development* (2016) (cited on pages 11–12).

[66] M. Popović, A. Nandi, M. Merkel, R. Etournay, S. Eaton, F. Jülicher, and G. Salbreux. "Active dynamics of tissue shear flow". *New Journal of Physics* 19.3 (2017), 033006 (cited on pages 13, 15, 25, 35, 41, 105, 107, 113).

[67] A. Sagner, M. Merkel, B. Aigouy, J. Gaebel, M. Brankatschk, F. Jülicher, and S. Eaton. "Establishment of global patterns of planar polarity during growth of the Drosophila wing epithelium". *Current Biology* 22.14 (2012), 1296–1301 (cited on pages 16–17).

[68] R. Etournay, M. Merkel, M. Popović, H. Brandl, N. A. Dye, B. Aigouy, G. Salbreux, S. Eaton, and F. Jülicher. "TissueMiner: a multiscale analysis toolkit to quantify how cellular processes create tissue dynamics". *eLife* 5 (2016), e14334 (cited on pages 28, 101).

[69] M. Mayer, M. Depken, J. S. Bois, F. Jülicher, and S. W. Grill. "Anisotropies in cortical tension reveal the physical basis of polarizing cortical flows". *Nature* 467.7315 (2010), 617–621 (cited on page 32).

[70] M. C. Smith. "Synthesis of mechanical networks: the inerter". *Automatic Control, IEEE Transactions on* 47.10 (2002), 1648–1662 (cited on page 37).

[71] L. Giomi, L. Mahadevan, B. Chakraborty, and M. F. Hagan. "Excitable Patterns in Active Nematics". *Physical Review Letters* 106 (21 2011), 218101 (cited on pages 45, 48).

[72] R. FitzHugh. "Impulses and physiological states in theoretical models of nerve membrane". *Biophysical journal* 1.6 (1961), 445–466 (cited on page 48).

[73] A. L. Hodgkin and A. F. Huxley. "A quantitative description of membrane current and its application to conduction and excitation in nerve". *The Journal of Physiology* 117.4 (1952), 500 (cited on page 48).

[74] B. I. Shraiman. "Mechanical feedback as a possible regulator of tissue growth". *Proceedings of the National Academy of Sciences of the United States of America* 102.9 (2005), 3318–3323. eprint: `http://www.pnas.org/content/102/9/3318.full.pdf` (cited on pages 53, 77).

[75] M. Delarue, J.-F. Joanny, F. Jülicher, and J. Prost. "Stress distributions and cell flows in a growing cell aggregate". *Interface Focus* 4.6 (2014), 20140033 (cited on pages 53, 77).

[76] F. D. Fischer, G. A. Zickler, J. W. C. Dunlop, and P. Fratzl. "Tissue growth controlled by geometric boundary conditions: a simple model recapitulating aspects of callus formation and bone healing". *Journal of The Royal Society Interface* 12.107 (2015). eprint: `http://rsif.royalsocietypublishing.org/content/12/107/20150108.full.pdf` (cited on page 53).

[77] Y. Gu and J. Rosenblatt. "New emerging roles for epithelial cell extrusion". *Current Opinion in Cell Biology* 24.6 (2012), 865–870 (cited on page 56).

[78] E. Marinari, A. Mehonic, S. Curran, J. Gale, T. Duke, and B. Baum. "Live-cell delamination counterbalances epithelial growth to limit tissue overcrowding". *Nature* 484.7395 (2012), 542–545 (cited on page 56).

[79] J. A. Sherratt. "Actin aggregation and embryonic epidermal wound healing". *Journal of Mathematical Biology* 31.7 (1993), 703–716 (cited on page 67).

[80] X. Ma, H. E. Lynch, P. C. Scully, and M. S. Hutson. "Probing embryonic tissue mechanics with laser hole drilling". *Physical Biology* 6.3 (2009), 036004 (cited on page 67).

[81] Y. Belacortu and N. Paricio. "Drosophila as a model of wound healing and tissue regeneration in vertebrates". *Developmental Dynamics* 240.11 (2011), 2379–2404 (cited on page 67).

[82] M. T. Abreu-Blanco, J. M. Verboon, R. Liu, J. J. Watts, and S. M. Parkhurst. "Drosophila embryos close epithelial wounds using a combination of cellular protrusions and an actomyosin purse string". *Journal of Cell Science* 125.24 (2013), 5984–5997. eprint: `http://jcs.biologists.org/content/125/24/5984.full.pdf` (cited on page 67).

[83] A. Brugués, E. Anon, V. Conte, J. H. Veldhuis, M. Gupta, J. Colombelli, J. J. Muñoz, G. W. Brodland, B. Ladoux, and X. Trepat. "Forces driving epithelial wound healing". *Nature Physics* 10.9 (2014), 683–690 (cited on page 67).

[84] M. Wilkin, M. Becker, D. Mulvey, I. Phan, A. Chao, K. Cooper, H.-J. Chung, I. Campbell, M. Baron, and R. MacIntyre. "Drosophila Dumpy is a gigantic extracellular protein required to maintain tension at epidermal–cuticle attachment sites". *Current Biology* 10.10 (2000), 559–567 (cited on pages 75, 102).

[85] C. Bertet, L. Sulak, and T. Lecuit. "Myosin-dependent junction remodelling controls planar cell intercalation and axis elongation". *Nature* 429.6992 (2004), 667–671 (cited on page 77).

[86] C. Collinet, M. Rauzi, P.-F. Lenne, and T. Lecuit. "Local and tissue-scale forces drive oriented junction growth during tissue extension". *Nature Cell Biology* (2015) (cited on page 77).

[87] R. Keller, L. Davidson, A. Edlund, T. Elul, M. Ezin, D. Shook, and P. Skoglund. "Mechanisms of convergence and extension by cell intercalation". *Philosophical Transactions of the Royal Society of London B: Biological Sciences* 355.1399 (2000), 897–922 (cited on page 77).

[88] M. Tada and C.-P. Heisenberg. "Convergent extension: using collective cell migration and cell intercalation to shape embryos". *Development* 139.21 (2012), 3897–3904 (cited on page 77).

[89] O. Voiculescu, F. Bertocchini, L. Wolpert, R. E. Keller, and C. D. Stern. "The amniote primitive streak is defined by epithelial cell intercalation before gastrulation". *Nature* 449.7165 (2007), 1049–1052 (cited on page 77).

[90] M. González-Gaitán, M. P. Capdevila, and A. García-Bellido. "Cell proliferation patterns in the wing imaginal disc of Drosophila". *Mechanisms of Development* 46.3 (1994), 183–200 (cited on pages 79, 95).

[91] L. A. Baena-López, A. Baonza, and A. García-Bellido. "The orientation of cell divisions determines the shape of Drosophila organs". *Current Biology* 15.18 (2005), 1640–1644 (cited on pages 79, 95).

[92] Y. Mao, A. L. Tournier, A. Hoppe, L. Kester, B. J. Thompson, and N. Tapon. "Differential proliferation rates generate patterns of mechanical tension that orient tissue growth". *The EMBO journal* 32.21 (2013), 2790–2803 (cited on pages 79, 95).

[93] I. Heemskerk, T. Lecuit, and L. LeGoff. "Dynamic clonal analysis based on chronic in vivo imaging allows multiscale quantification of growth in the Drosophila wing disc". *Development* 141.11 (2014), 2339–2348 (cited on pages 79, 95).

[94] P. Marmottant and F. Graner. "An elastic, plastic, viscous model for slow shear of a liquid foam". *The European Physical Journal E* 23.4 (2007), 337–347 (cited on page 93).

[95] G. Marrucci, R. B. Bird, C. F. Curtiss, R. C. Armstrong, and O. Hassager. "Dynamics of polymeric liquids. Volume 2: Kinetic Theory By R. Ryron Bird, Charles F. Curtis, Robert C. Armstrong, and Ole Hassager, John Wiley & Sons, Inc., New York, 2nd Ed., 1987, 437 + xxi pp." *AIChE Journal* 35.8 (1989), 1399–1402 (cited on page 99).

[96] C. H. Waddington. "The genetic control of wing development in Drosophila". *Journal of Genetics* 41.1 (1940), 75–113 (cited on page 102).

Versicherung

Hiermit versichere ich, dass ich die vorliegende Arbeit ohne unzulässige Hilfe Dritter und ohne Benutzung anderer als der angegebenen Hilfsmittel angefertigt habe; die aus fremden Quellen direkt oder indirekt übernommenen Gedanken sind als solche kenntlich gemacht. Die Arbeit wurde bisher weder im Inland noch im Ausland in gleicher oder ähnlicher Form einer anderen Prüfungsbehörde vorgelegt.

Diese Arbeit wurde unter der wissenschaftlichen Betreuung durch Prof. Dr. Frank Jülicher und Dr. Guillaume Salbreux am Max-Planck-Institut für Physik komplexer Systeme in Dresden angefertigt.

Ich erkläre hiermit, dass keine früheren erfolglosen Promotionsverfahren stattgefunden haben. Ich erkenne die Promotionsordnung der Fakultät für Mathematik und Naturwissenschaften der Technische Universität Dresden an.

_____

Dresden, _____, Marko Popović